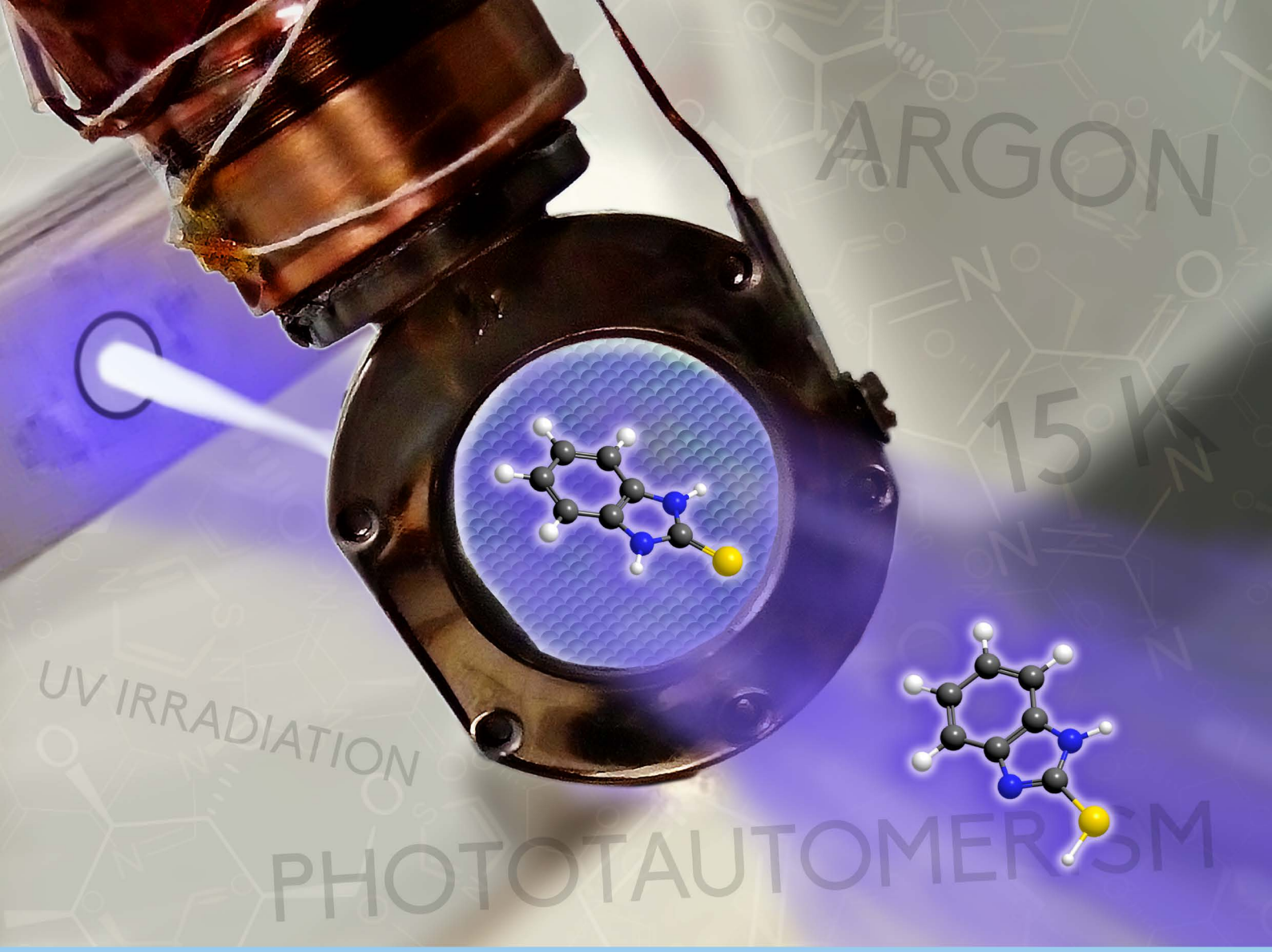

Elisa Marçalo Brás

On The Tautomerism of 2-Mercaptoimidazoles and 2-Mercaptobenzimidazoles: A Low Temperature Matrix Isolation and Solid State Study

Mestrado em Química

Departamento de Química

FCTUC

Setembro 2017

· U C ·

Universidade de Coimbra

Elisa Marçalo Brás

On the Tautomerism of 2-Mercaptoimidazoles and 2-Mercaptobenzimidazoles: A Low Temperature Matrix Isolation and Solid State Study

Dissertação apresentada para provas de Mestrado em Química

Área de especialização em Química Avançada e Industrial

Orientador: Professor Doutor Rui Fausto M. R. S. Lourenço

Setembro de 2017

Universidade de Coimbra

‘‘*Science is not only a disciple of reason but, also, one of romance and passion*.”

Stephen Hawking

“On the walls of the cave, only the shadows are the truth.”

Plato, The Allegory of the Cave

Acknowledgements

At the end of this journey, I would like to thank to all of those who contributed to the accomplishment of this work.

I would like to express my deepest gratitude to Professor Rui Fausto Lourenço, my supervisor, for giving me the opportunity to develop my work at the Laboratory of Molecular Cryospectroscopy and Biospectroscopy (LMCB) in a research field that I admire. I am also very thankful for the guidance, concern and support in key moments. He was always there to help and discuss research ideas and results.

To Professor José António Paixão and Marta Henriques, from the Department of Physics, a very special acknowledgement for the collaboration in this work and for the help provided. I would like also to thank Marta for her friendship.

To Professor Ermelinda Eusébio and Professor João Canotilho, I would like to thank for allowing me to do some studies at the Molecular Thermodynamics and Solid State Chemistry Laboratory and for the help provided in the discussion of the results obtained therein.

To Professor Maria de Lurdes Cristiano from the University of Algarve, I would like to thank for the opportunity to participate in some fruitful investigations, apart from the thesis work.

To all LMCB members, I would like to thank for the daily company and for the help provided in many different ways.

To my closest friends, especially to Diana Santos, Eduardo Gomes, Patricia Prazeres, António Góis and Rute Coelho, a very special thank for always being there for me. I am very lucky to have you by my side.

To the most important, my parents and my sister, I am eternally grateful for the unconditional love, for all the sacrifices made and endless support. It would not have been possible without you.

Thank you very much.

Table of Contents

Abbreviations

1-M-2-MBI: 1-Methyl-2-Mercaptobenzimidazole

1-M-2-MI: 1-Methyl-2-Mercaptoimidazole

2-MBI: 2-Mercaptobenzimidazole

2-MI: 2-Mercaptoimidazole

ATR: Attenuated Total Reflectance

B3LYP: Becke's Three-Parameters Lee, Yang and Parr Exchange Functional

CI: Configuration Interaction

DFT: Density Functional Theory

DNA: Deoxyribonucleic Acid

DSC: Differential Scanning Calorimetry

DTGS: Deuterated Triglycine Sulfate Detector

ESIPT: Excited State Intramolecular Proton Transfer

FIR: Far-infrared

FTIR: Fourier Transform Infrared

GGA: Generalized Gradient Approximation

H-Bond: Hydrogen Bond

HF: Hartree-Fock Theory

HOMA: Harmonic Oscillator Model of Aromaticity

IDI: (2-[(1*H*-Imidazol-2-yl)disulfanyl]-1*H*-imidazole)

IR: Infrared

IUPAC: International Union of Pure and Applied Chemistry

LDA: Local Density Approximation

LSDA: Local Spin Density Approximation

MP: Møller-Plesset

NIR: Near-Infrared

PED: Potential Energy Distribution

PLTM: Polarized Light Thermal Microscopy

THF: Tetrahydrofuran

T_{fus}: Melting point

UV: Ultraviolet

XRD: X-ray Diffraction

$\Delta_{fus}H$: Enthalpy of Fusion

Abstract

The thione-thiol tautomerism has been only scarcely investigated in spite of its well-known relevance in chemical processes. In this thesis, investigations on the tautomerism of 2-mercaptoimidazole, 2-mercaptobenzimidazole and their 1-methyl substituted derivatives (1-methyl-2-mercaptoimidazole and 1-methyl-2-mercaptobenzimidazole) are reported.

The photoinduced thione-thiol tautomerism in these molecules was investigated by low-temperature matrix isolation spectroscopy and quantum chemical calculations. The initial population of the studied molecules trapped in the matrices, in all the performed experiments, comprised only the thione tautomer, the thermodynamically most stable tautomer predicted by DFT(B3LYP)/6-11++G(d,p) calculations. Upon *in situ* narrowband UV irradiation, the as-deposited thione forms were partially converted into the corresponding thiol forms. The photoreversibility of this type of process was proved for the benzosubstituted 2-mercaptoimidazoles, by undertaken selective irradiation of the thiol forms (at λ = 246 nm). The thiol → thione conversion was shown to have a greater efficiency than the thione → thiol conversion.

An interesting result extracted from the performed quantum chemical calculations is that the studied molecules do not exhibit any intramolecular H-bond, a result that has been also confirmed by the crystal data. This points to a mechanism of phototautomerization involving a hydrogen atom transfer from the nitrogen of the imidazole ring to the sulphur atom (or vice versa), which shall take place via bond-breaking and re-attachment, instead of the well-known ESIPT process.

The investigation on the tautomerism of 2-mercaptoimidazole in the solid state was also undertaken by Raman microspectroscopy, X-ray diffraction, polarized light thermal microscopy and differential scanning calorimetry. The results showed also only the presence of the thione tautomer in the solid state. In spite of our attempts to generate different crystalline forms, polymorphism was not observed for this molecule.

On the other hand, in the course of solid state investigations, a new polymorph of 2-[(1*H*-Imidazol-2-yl)disulfanyl]-1*H*-imidazole (a dimer of 2MI) was synthetized and characterized by Raman spectroscopy and single crystal X-ray diffraction. X-ray results revealed a structure with four symmetry independent molecules in the unit cell (Z' = 4), which assume conformations similar to all of the possible

conformers of the molecule predicted by the calculations performed on the single molecule of the compound. Detailed analyses of the structure of the new polymorph of this compound and of its thermal properties were also undertaken.

Resumo

Apesar da sua relevância em vários processos químicos, o tautomerismo tiona-tiol não tem sido objecto de muitos estudos. O trabalho apresentado nesta tese centra-se no estudo deste tipo de tautomerismo nas moléculas 2-mercaptoimidazol, 2-mercaptobenzimidazol e dos seus derivados metilados (1-metil-2-mercaptoimidazol e 1-metil-2-mercaptobenzimidazol).

O foto-tautomerismo nestes compostos foi investigado usando espectroscopia de infravermelho com isolamento em matrizes criogénicas e métodos computacionais. Antes da irradiação dos compostos previamente isolados numa matriz criogénica (árgon), a comparação da informação espectral experimental e calculada levou à conclusão de que o tautómero tiona era único tautómero presente nas matrizes. Este resultado é coerente com os cálculos realizados ao nível DFT (B3LYP)/6-11++G(d,p), através dos quais foi possível concluir que o tautómero tiona é o tautómero termodinamicamente mais estável. Após a irradiação das matrizes com luz UV de banda estreita, a comprimento de onda criteriosamente selecionado, os tautómeros tiona das espécies isoladas foram parcialmente convertidos nos respectivos tióis. Para além disso, a reversibilidade do tautomerismo foi confirmada para o caso dos 2-mercaptoimidazóis benzo substituídos através da irradiação selectiva a λ = 246 nm. Este último processo revelou-se mais eficiente que a conversão thiona → thiol.

Uma vez que nas moléculas isoladas dos compostos estudados não existem ligações de hidrogénio intramoleculares, facto que é sustentado pelas estruturas cristalinas dos compostos e pelos cálculos teóricos realizados para as moléculas isoladas, o mecanismo por transferência de protão intramolecular (ESIPT) não pode ser considerado para explicar as reacções de tautomerização observadas. Um possível mecanismo consiste na transferência de átomo de hidrogénio do anel imidazol para o átomo de enxofre (ou vice-versa), através de um processo de clivagem de ligação (N-H ou S-H), seguida da recombinação do átomo de hidrogénio com o radical inicialmente formado em posição distinta da original (S ou N, respectivamente).

A investigação sobre o tautomerismo do 2-mercaptoimidazole no estado sólido foi realizada por microespectroscopia de Raman, difração de raios X, termomicroscopia com luz polarizada e calorimetria diferencial de varrimento. Os resultados das experiências realizadas comprovaram que apenas que o

tautómero mais estável existe em fase cristalina. Apesar das tentativas realizadas, não foi possível obter mais do que um polimorfo do composto.

Por ouro lado, no decorrer das investigações do estado sólido, foi sintetizado um novo polimorfo do composto 2-[(1*H*-imidazol-2-il)dissulfanil]-1*H*-imidazo (um dímero do 2-MI), que foi posteriormente caracterizado por espectroscopia de Raman e difração de raios-X de monocristal. Os resultados revelaram uma estrutura com quatro moléculas independentes (Z '= 4) na célula unitária. A estrutura deste polimorfo foi caracterizada em detalhe e foi também efetuado o estudo das propriedades térmicas deste novo material. Um resultado muito interessante, foi a observação, no cristal, de unidades monoméricas com conformações que se assemelham a todos os possíveis confórmeros previstos para a molécula isolada deste composto.

CHAPTER I

Chapter I. Introduction

1.1 2-Mercaptoimidazoles, 2-Mercaptobenzimidazoles and their 1-Methyl Substituted Derivatives

The applications of 2-mercaptoimidazoles, 2-mercaptobenzimidazoles and their 1-methyl-derivatives are vast. The interest on the chemistry of this type of nitrogen and sulphur containing molecules results mostly from their significant role in coordination chemistry, since they can effectively act as N, S bridging/chelating ligands of a wide range of metal ions[1-3], and also because their applications in organic and medicinal chemistry as antithyroid drugs.[3-6] 1-methyl-2-mercaptoimidazole, commonly known as methimazole, is a coordination drug which is currently used for the treatment of Graves disease.[4,5] These compounds have also been applied in materials science as dyes, catalytic agents, and rubber antioxidants.[7] Furthermore, these type of molecules can exhibit tautomerism and may exist as thione and/or thiol tautomeric forms[8] (**figure 1**). Another interesting feature is that the thiol forms can be easily oxidized into to the corresponding symmetrical disulfide compounds, which, in turn, can also be easily reduced to the initial thiols.[9]

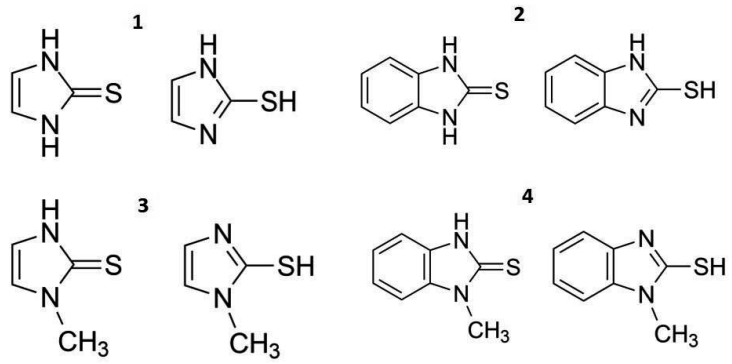

Figure 1. Tautomeric molecular structures of the compounds studied in this work. **1.** 2-mercaptoimidazole **2.** 2-mercaptobenzimidazole **3.** 1-methyl-2-mercaptoimidazole **4.** 1-methyl-2-mercaptobenzimidazole.

Despite the well-established applications, several features concerning the structure and properties of these type of molecules still remain unclear. In fact, the thione/thiol tautomerism, involving the sulphur atom, has been much less studied than the related oxo/ hydroxy oxygen tautomerism.

1.2 Tautomerism

1.2.1 Concept

According to the IUPAC definition[10] tautomerism is an isomerism of the overall form:

$$\mathrm{G\text{-}X\text{-}Y} = \mathrm{Z} \leftrightarrows \mathrm{X} = \mathrm{Y\text{-}Z\text{-}G} \qquad (\mathbf{1.2.1})$$

where the isomers (tautomers) are interconvertible; the atoms which connect the groups X, Y, and Z are typically C, N, O or S atoms, and G is a group that act as electrofuge or nucleofuge through the isomerization.

Tautomers of a molecule usually have different physical and chemical properties and tridimensional shape and, consequently, molecular fingerprints. A well-known and extremely relevant result of tautomerism and differences between tautomers occurs in both purine and pyrimidine bases of DNA.[11] Since tautomers have different structures, and consequently the protons occupy different positions in the molecules, when a nucleotide base shifted into one of its rare tautomers the result may be a pair mismatching, with all possible consequences of this.[11,12]

1.2.2 Tautomerism and Environment

During several years, the knowledge around the concept of tautomerism was only empirical and qualitative. Near the eighties of the previous century, the understanding of the thermodynamic aspects of the tautomerism of heteroaromatic molecules was improved and, nowadays, the dependence of the tautomeric forms on the surrounding chemical environment[13,14] as the influence of substituent, solvents, temperature and pH, is well known, and both qualitative and quantitative analyses can be performed on tautomeric systems due to the increasing accuracy of calculations and of experimental methodologies.

Currently, it is possible to determine thermodynamic and kinetic aspects related to tautomerism in solution, solid and gas phases, comprising ground and excited states.

Tautomerism may be of various types.[10,15] Usually, tautomerization involves proton transfer and hydrogen bonding is often associated. This process can be both intra and intermolecular, and solvent molecules can participate in it. Tautomerism comprising excited states can also occur by other mechanism,[19-22] which is discussed below.

1.2.2.1 Phototautomerism

In matrix isolation experiments, tautomerization can occur by thermal activation[18] or can be photoinduced. The typically known photochemical process of the proton-transfer occurring after excitation is defined as ESIPT (Excited-State Intramolecular Proton Transfer).[15-17] ESIPT processes can occur in systems which possess a proton donor and proton acceptor linked by a hydrogen bond. However, several phototautomerisms have been induced in molecular species which do not bear any intramolecular H-bond interactions.[23-36] The first observation of an UV-induced hydrogen-atom-transfers process from a nitrogen atom of a heterocyclic ring to an exocyclic oxygen in this type of molecular systems, and in inert gas matrices, was reported by Łapiński et al. for 4(3H)-pyrimidinone.[23-25] After this study, similar hydrogen-atom-transfer processes for molecules bearing one, two or more heteroatoms were observed, such as in 2(1*H*)-pyrdinone,[26,27] 3(2*H*)-pyridazinone,[28] 4(3*H*)-pyrimidinethione,[29] 3(2*H*)-pyridazinethione,[29] maleic hydrazide,[30] cytosine,[31-33] isocytosine,[34] phenol,[35] thiophenol[36] and 7-azaindole[37] isolated in low temperature matrices .

Since no intramolecular H-bonds exist in these type of systems the phototautomerization mechanism must be completely different from the ESIPT process. Such hypothesis has been supported by experiments using solid hydrogen as a matrix-host material.[38-41] The proposed mechanism involves the hydrogen atom detachment, occurring after excitation of the chemical species under study, with subsequent radical formation, followed by radical recombination. This mechanism was not yet completely elucidated, and has been drawn from the theoretical model proposed by Sobolewski et al.[19-22]

1.2.2.2 Solid State

In the solid state, the concept of tautomerism is often referred to tautomeric polymorphism. However, the oldest definition of polymorphism, suggested by McCrone,[42,43] implies that existence of

polymorphism requires that “at least two different arrangements of the molecules of that compound in the solid state exist that give rise to the same species in the melted state”. Such definition excludes the tautomerism, because this one lead, *a priori*, to the formation of different molecules.

The term desmotropy was introduced by Jacobson[44,45] and refers to the crystallization of a compound in different tautomers. If a compound can be isolated in different tautomeric forms (separately), as rhodanine[46-48] shown in **figure 2**, it shall be named desmotropic. Desmotropy is not a very rare phenomenon, but is often found under the headings “tautomerism” or “polymorphism”.[49-51] Tautomerization in the solid state is an example of dynamic desmotropy.[52-53]

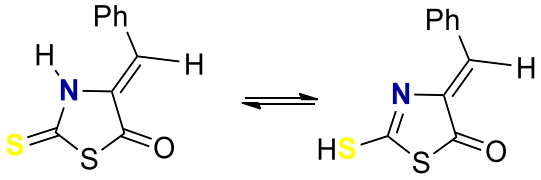

Figure 2. Desmotropic Rhodanine.[46-48]

Besides desmotropy, another interesting phenomenon can occur upon the crystallization of chemical species that can exhibit tautomerism: the same crystal can contain, simultaneously, two tautomers, usually establishing hydrogen bonds.[54-56] However, in contrast to solution, in which tautomers in general coexist, in the crystalline state typically only one the tautomer is present in the crystal. Commonly, this corresponds to the most stable tautomer (thermodynamic crystal), especially if the energy difference (and activation energy) between the two tautomers is large. However, since the crystallization process depends on the balance of thermodynamics and kinetics, and that in solution both tautomers are generally present, the final product may result from the less stable but faster growing crystallization nuclei. It is also relevant to take into account that intermolecular forces may play an important role in stabilizing of less stable tautomers in the solid state (metastable tautomers).

1.3 The Aim of this Thesis

The work presented in this thesis aims to contribute to a better understanding of tautomerism in 2-mercaptoimdazole, 2-mercaptobenzimidazole, and their 1-methyl-derivatives (1-methyl-2-mercaptoimidazole and 1-methyl-2-mercaptobenzimidazole). This includes an investigation of the molecular structure of the compounds by quantum chemical calculations, in order to clarify structure-

energy relations between their two tautomeric forms (and also between the four molecules), an experimental determination and characterization of the most stable tautomeric forms in low temperature matrices, an investigation of the effect of *in situ* narrowband UV irradiation on the tautomerism of the isolated molecules, as well as the reactional mechanism. The work aimed also the elucidation of structural aspects of the solid state phases of the compound using infrared spectroscopy, Raman microspectroscopy, X-ray diffraction, polarized light thermal microscopy and differential scanning calorimetry, besides computational studies performed using contemporary computational methods of quantum chemistry.

1.4 Computational Chemistry

Theoretical chemistry can be considered the mathematical representation of chemistry. In this field, the study of chemical properties and reactions is done using the combination of mathematical models and fundamental laws of physics.

Computers development has led to an increase of the application of quantum chemical calculations as a tool to aid the interpretation of experimental results. Nowadays, it is possible to determine the relative stability of species and calculate their vibrational spectra, for example, with a very satisfactory level of approximation, allowing the direct comparison of theoretical and experimental data.

In this work, quantum chemical calculations performed using the Density Functional Theory (DFT) method with the Becke's three-parameter Lee, Yang and Parr exchange functional (B3LYP), were used to estimate geometries, energies, and vibrational spectra of the tautomeric species of the molecules under investigation, their possible conformers and also products of their photolysis, including reactive intermediates. These calculations proved to be essential to the correct and detailed analysis/interpretation of the experimental results. The theoretical foundations of the method used in this study are briefly described in more detail in the next subsection **1.4.1.**

1.4.1 Density Functional Theory

The proper treatment of electron-electron interactions in molecular systems which contain two or more electrons has been the major difficulty of all electronic structure methods developed hitherto.[57-60] In the Hatree-Fock (HF) method, the electronic energy is overestimated.[57,58,60] Møller-Plesset (MP) perturbation theory[57,58] and Configuration Interaction method (CI),[57,58] developed from the Hartree-Fock

theory, can give accurate electronic energies results, but they are limited to small molecules. When applied to large systems, the computation time becomes very expensive. These large computational demands, arise mainly from the expensive computation of the molecular wave-function used to determine the electronic energy, which becomes too complex with the increasing number of electrons.

Density Functional Theory (DFT) is computationally very efficient approach to solve polyelectronic systems,[59] and is, nowadays, the most widely-used quantum chemical method.

The DFT method is based in the work of Hohenberg, Kohn and Sham.[57-59;61,62] Hohenberg and Kohn established that the electronic energy, E, of a chemical system is determined through a physical property, the total electron density , $\rho(r)$. This means that the energy is a function of a function, i.e., it is a functional. Moreover, they further proved that the exact ground state corresponds to the global minimum value of the functional. However, the Hohenberg-Kohn theorems do not establish the form of the functional relating E and $\rho(r)$, although the equations developed later by Kohn and Sham made the DFT method applicable. According to the Kohn-Shank formulation, the total energy, as function of density, $E[\rho(r)\,]$, is described in the following terms:

$$E[\rho(r)] = E_T[\rho(r)] + E_V[\rho(r)] + E_J[\rho(r)] + E_{XC}[\rho(r)] \qquad (\mathbf{1.4.1})$$

where E_T is the kinetic energy, E_V is the nuclear - electronic attraction potential energy, E_J is the classic Coulombic inter-electronic repulsion and E_{XC} the exchange-correlation energy functional.

In fact, there is a relation between the total electron density and the normalized wave function, since the electron density is the result of the square of the normalized wave function divided by the total number of electrons of the system. The electron density $\rho(r)$ is represented by a linear combination of basis sets and is related with the Kohn-Sham orbitals, ψ_i^{ks}, equation **1.4.2**:

$$\rho(r) = 2\sum_{i}^{orb}\left|\psi_i^{ks}(r)\right|^2 \qquad (\mathbf{1.4.2})$$

In turn, the Kohn-Sham orbitals, ψ_i^{ks}, that allow the calculation of the electronic density, are determined by the solution of the equation:

$$\hat{h}_i^{ks}\,\psi_i^{ks} = \varepsilon_i\psi_i^{ks} \qquad (\mathbf{1.4.3})$$

where $\hat{h}_i^{ks}$ is the Kohn-Sham operator and ε_i are the Kohn-Sham orbital energies.

Some relevant problems of this method are related to the approximated nature of the exchange-correlation energy functional. In order to solve this problem, some approximations have been developed to calculate this functional, including the Local Spin Approximation (LSDA), the Generalized Gradient Approximations (GGA), and the simplest one, based on the uniform electron density through the system under analysis, the Local Density Approximation (LDA).[59,] Other methods, designated by hybrid methods, have been developed with the same purpose. The hybrid B3LYP functional,[63-67] used in this work, is one of the most widely used to perform chemical calculations. In the B3LYP functional, the exchange term was developed by Becke,[63] and the correlation functionals were developed by Lee, Yang and Parr (LYP)[67] and Vosko, Wilk and Nussair (VWN):[66]

$$E_{xc}^{\mathrm{B3LYP}} = (1-\mathrm{a})E_x^{\mathrm{LSDA}} + E_x^{\mathrm{HF}} + \mathrm{b}\Delta E_x^{\mathrm{B}} + (1-\mathrm{c})\,E_C^{VWN} + \mathrm{c}E_C^{\mathrm{LYP}} \qquad (\mathbf{1.4.4})$$

where the a, b and c are the three Becke parameters, E_x^{LSDA} is the exchange-energy functional with the Local Spin Density Approximation (LSDA), E_x^{HF} is the HF exchange functional, ΔE_x^{B} is the Becke exchange functional, E_C^{VWN} is the Vosko, Wilk and Nussair correlation functional, and $\mathrm{c}E_C^{\mathrm{LYP}}$ is the Lee, Yang and Parr correlation functional.

This method has been shown to provide a useful balance between computational efficiency and accuracy, and it has been frequently applied in the research carried out in LMCB group, particularly for calculation of geometries, relative energies and vibrational spectra.

1.4.2 Basis Sets

As referred to above, the molecular orbitals are expressed as linear combination of basis functions (see equation **1.4.2**), generally centered on atomic nuclei. Nowadays, a large number of basis sets are available to perform the calculations, and a correct choice of the basis set is crucial to guarantee both good accuracy in the results and affordable computational cost.

Pople basis sets are also known by split-valence basis sets and are the most commonly used.[68,69] The name comes from the fact that the valence orbitals are represented by more than one set of functions, thus improving the flexibility of the basis set in the description of the regions of molecular space that are more relevant to chemistry, since the valence electrons are those that mainly contribute to bonding. Further flexibility in the basis set can be attained by the additional use of polarization and diffuse functions.

In this work, the Pople 6-311++G(d,p) basis set was used to perform all calculations. This basis is a split-valence triple-ζ basis set augmented with polarization functions in both hydrogen and heavier atoms as well as diffuse functions. In the name of the basis set, the number 6 refers to the number of the Gaussian functions used to represent the core orbitals. The numbers followed by the hyphen refer to the description of the valence shell and correspond to the number of Gaussian functions used in the treatment of the valence orbitals (three sets of primitive Gaussians: 3 contracted functions plus two single Gaussians, affording three basis functions per valence orbital). The polarization functions describe atomic orbitals of higher quantum numbers than those necessary to describe the ground state atomic configuration and, in this case, correspond to *d* and *p*-type orbitals, for heavy atoms and hydrogens, respectively.[69] The included diffuse functions are represented by the symbol "+", and correspond to Gaussian functions of small exponent, which then cover regions of the space far from the nucleus where they are centered.[70] These type of functions are usually necessary to the description of molecular systems that contain lone pairs of electrons or species participating in weak closed-shell type interactions. They are also relevant for a correct prediction of polarizabilities and dipole moments, so being in general considered to be relevant for a proper prediction of IR and Raman intensities.

1.4.3 Normal Coordinate Analysis

The normal coordinate analysis allows the characterization of the vibrational modes. The FG Wilson method,[71] which was the selected method to perform the vibrational calculations in this study, is based in the Classical Mechanics and is the most widely used method to perform the normal mode analysis. The normal mode frequencies are calculated taking into account the force constants, reduced masses and molecular geometries. The composition of the normal modes in terms of internal, or symmetry, coordinates, is possible to acquire by this method and is represented by the potential energy distribution (PED) matrix. [72]

The five extended degrees of freedom for movement of the nuclei for a linear molecule are three coordinates for the motion of the center of mass and two rotational angles; hence, 3N-5 internal coordinates refer to the molecular vibrations. In the case of non-linear molecules, there are three possible rotational angles instead of two, hence 3N-6 non-linear internal coordinates for vibrations description.

According to the laws of Classical Mechanics, the vibrational modes and frequencies can be obtained by solving the Newton's equations of motion. Succinctly, the description of the vibrational energy can be defined in terms of kinetic and potential energies. This terms can be described in terms of internal coordinates by the following matricial equations:

$$T = \frac{1}{2}\boldsymbol{D'^{t}G^{-1}D'} \qquad (\mathbf{1.4.5})$$

$$V = \frac{1}{2}\boldsymbol{D^{t}FD} \qquad (\mathbf{1.4.6})$$

In this matricial notation, $\boldsymbol{D}$ in the column vector of the internal coordinates and $\boldsymbol{D'}$ the vector of their time derivatives. $\boldsymbol{F}$ represents the force constants matrix in terms of internal coordinates, and the $\boldsymbol{G}$ matrix is related to the masses of atoms and geometry. The $\boldsymbol{F}$ and $\boldsymbol{G}$ matrices are symmetric and their dimensions are equal to the number of internal coordinates of the molecule. The elements of the $\boldsymbol{G}$ matrix can be obtained from the nuclei masses and molecular geometries by the following relation:

$$\boldsymbol{G = BM^{-1}B^{t}} \qquad (\mathbf{1.4.7})$$

where $\boldsymbol{M^{-1}}$ is a diagonal matrix (3N x 3N) of the inverse nuclear masses, in which the nuclear mass of each nuclei is repeated three consecutive times in the diagonal. $\boldsymbol{B}$ is the matrix that converts the Cartesian displacement coordinates into the internal coordinates of the molecule. This conversion is given by the expression:

$$\boldsymbol{D = BR} \qquad (\mathbf{1.4.8})$$

The normal coordinates, represented by the vector $\boldsymbol{Q}$, are the 3N-6 orthogonal coordinates that describe the atoms motion in each molecular vibration. This vector is related to the internal coordinates by the linear transformation $\boldsymbol{D = LQ}$**.** The $\boldsymbol{L}$ matrix results from the juxtaposition of the 3N-6 eigenvectors of the $\boldsymbol{FG}$ product matrix.

The kinetic and potential energies can be written, in terms of the normal coordinates and their derivatives with time, as the following matricial equations:

$$T = \frac{1}{2}\boldsymbol{Q'^{t}L^{t}G^{-1}LQ'} = \frac{1}{2}\boldsymbol{Q'^{t}EQ'} \qquad (\mathbf{1.4.9})$$

$$V = \frac{1}{2}\boldsymbol{Q^{t}L^{t}FLQ} = \frac{1}{2}\boldsymbol{Q^{t}\Lambda Q} \qquad (\mathbf{1.4.10})$$

where $\boldsymbol{E}$ and Λ are the diagonal identity matrix and the diagonal matrix composed by the eigenvalues of the $\boldsymbol{FG}$ matrix, respectively. In this way, the vibrational energy of a molecule is given by the following equation:

$$E_{vib} = \frac{1}{2}\boldsymbol{Q'^{t}EQ'} + \frac{1}{2}\boldsymbol{Q^{t}\Lambda Q} \qquad (\mathbf{1.4.11})$$

Taking into account that $\boldsymbol{L^{t}FL = \Lambda}$, since $\boldsymbol{L^{t}G^{-1}L = E}$ or $\boldsymbol{L^{t} = L^{-1}G}$, the following equation is obtained:

$$\boldsymbol{L^{-1}FGL = \Lambda} \qquad (\mathbf{1.4.12})$$

which describes the diagonalization of the $\boldsymbol{FG}$ matrix. In fact, the normal modes determination implies finding the $\boldsymbol{L}$ matrix that works as operator for diagonalizing the $\boldsymbol{FG}$ product matrix. In practice, the 3N-6 solutions of the diagonalization procedure, that are related one-by-one to the vibrational frequencies, are obtained by solving the following secular determinant:

$$|\boldsymbol{FQ - E\lambda_i}| = 0 \qquad (\mathbf{1.4.13})$$

Each solution, $\boldsymbol{\lambda_i}$, of the previous equation corresponds to one of the eigenvalues of the $\boldsymbol{FG}$ matrix and is related to a group of eigenvectors, $\boldsymbol{L_i}$, which differ from each other by a constant.

The most relevant results extracted from the FG method are the frequencies and the composition of each vibrational mode in terms of internal coordinates. As said above, the frequencies are directly related with the eigenvalues of the $\boldsymbol{FG}$ matrix. On the other hand, the characterization of each vibrational mode can be performed by taking into account the calculated potential energy distributions (PEDs), i.e., the composition of the force constant expressed in the normal coordinates system in terms of the force constants in the internal coordinates system. This last result can be easily understood: the kinetic energy term of a vibrational mode is equal to zero when the atoms reach the vibration turning point (i.e., the maximal distance from the equilibrium position); then, the vibrational energy is equal to the potential energy, which is proportional to $\boldsymbol{\lambda_i}$ **,** which is associated to the normal coordinate $\boldsymbol{Q_i}$. Since $\boldsymbol{\lambda_i}$ is in fact the force constant associated with the normal coordinate $\boldsymbol{Q_i}$., it can be expanded in terms of the force constants expressed in the internal coordinates system:

$$\boldsymbol{L_i^{t}FL_i} = \lambda_i \qquad (\mathbf{1.4.14})$$

Then, since the first member of the equation can be expressed as a sum:

$$\sum_{(\alpha;\beta)} \boldsymbol{L_i}^{\alpha} \boldsymbol{L_i}^{\beta} \boldsymbol{F}_{(\alpha;\beta)} \qquad (\mathbf{1.4.15})$$

where β and α refer to the internal coordinates, the potential energy distribution (PED), in percentage, is given by the expression:

$$[PED]_i^{F_{(\alpha;\beta)}} = \frac{100 \boldsymbol{L_i}^{\alpha} \boldsymbol{L_i}^{\beta} \boldsymbol{F}_{(\alpha;\beta)}}{\lambda_i} \qquad (\mathbf{1.4.16})$$

1.5 Matrix Isolation

Matrix isolation was initially developed, almost simultaneously, by George Pimentel (in USA) and by George Porter (in UK), in 1954, and refers to a method whereby guest chemical species are mixed with a large excess of a host gas (usually inert and non-reactive) and condensed onto a cold window (4-30 K) in order to ensure the quickly solidification of the mixture.[73,74] Thus, the target chemical species are trapped in a rigid cage of inert material as represented in **figure 3**, the "matrix", and isolated from each other by layers of the host gas (usually noble gases or other cryogenic "inert" solids). Under these conditions, the interactions between the solute molecules are virtually absent, and, due to the inertness of the matrix host gas, the solute-solvent interactions are also negligible. This makes the matrix isolation method an excellent approach for simulating the gas phase and trapping unstable species.[73-76;78]

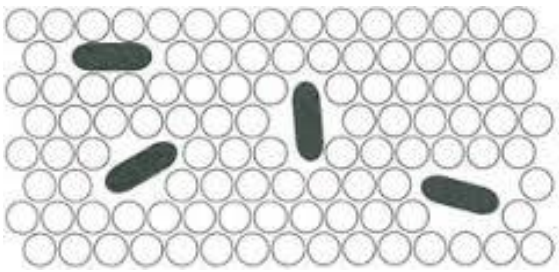

Figure 3. Schematic representation of trapped molecular species in a matrix host.[73]

The absence of relevant contacts between potentially reactive species, and the very low work temperature provide a perfect environment for stabilizing short-lived chemical species, such as reactive intermediates or other unstable species, which are stabilized in their ground electronic and vibrational

states and, subsequently, can be detected and characterized by stationary spectroscopic methods (*e.g.*, infrared, Raman, UV/vis spectroscopies). Moreover, since the molecules are trapped in a rigid material the diffusion is prevented and molecular aggregation minimized.

Another relevant aspect is that the gases used to perform matrix-isolation experiments (Ar, Xe, Ne, N_2, etc.) offer the advantage of transparency over a wide range of wavelengths, from the vacuum UV to the far-infrared (FIR).

1.5.1 Experimental Details

Because very low temperatures are necessary to solidify the above referred matrix host gases a specialized cryogenic equipment has to be used. Nowadays, closed-cycle helium refrigerators are used to achieve these conditions.[73,74] The experiments are performed in a vacuum chamber at very low pressure ($\leq 10^{-6}$ mbar) to promote the thermal insulation of the interior of the cryostat from the exterior environment. The matrix deposition requires that the compounds of interest have to be volatilizable. Compounds with enough vapor pressure can be premixed with the matrix host gas in a vacuum line or evaporated from glass tubes. For the case of solids and liquids without enough high vapor pressure, an additional equipment is required to heat and perform the vaporization or sublimation (such as mini ovens, Knudsen cells, etc.). The vapors enter the vacuum chamber at controlled flow and condensate onto the cold window attached to the cold tip of the cryostat, usually a closed cyclic helium refrigerator system. The matrix deposition procedure employed in this work is described in detail in the next chapter of this thesis.

1.5.2 Infrared Spectroscopy in Cryogenic Inert Matrices

Infrared spectroscopy is one of the most useful spectroscopic techniques employed for the elucidation of the molecular structure of samples in a wide range of temperatures and different physical states.

According to quantum mechanics, a molecule can take a quantity of energy, $h\nu$, to reach a higher energy state. In infrared spectroscopy, this transition generally occurs between the ground state and the first vibrational excited state.[72;82-84] A molecule which is irradiated with a continuous spectrum of infrared radiation can absorb light quanta (photons) that possess this quantized energy. The infrared spectrum reveals the incident radiation which is absorbed (or transmitted) at each vibrational frequency of the

molecule. However, interaction between infrared radiation and the molecular system is only possible if the oscillating frequency of the electric field of the incident radiation is the same as that of the molecular dipole moment. Then, a vibration is infrared active only if this interaction leads to the change of molecular dipole moment during the vibrational movement:

$$\left(\frac{\partial \mu}{\partial Q}\right)_0 \neq 0 \qquad (\mathbf{1.5.1})$$

In equation **(1.5.1)**, μ is the molecular dipole moment and Q is the normal coordinate which describes the motion of the atoms during a vibration.

As it was mentioned previously, polyatomic molecules possess 3N-6 normal modes of vibration, which have to obey to the particular feature above described above to be active in infrared. There are two main classes of molecular vibrations. Those which mostly alter the bond lengths, which are designated as stretching vibrations, and those that change predominantly the angles, which correspond to the bending and torsional vibrations. The vibrations can also be classified as symmetric or anti-symmetric, taking into account the symmetry of the molecule, and as in-plane or out-of-plane vibrations, if the molecule has planar fragments.

Although the infrared spectra can provide relevant structural information, those obtained using conventional techniques most of times do not afford the needed information to perform a detailed structural analysis. Indeed, the molecular motion in solution samples and a wide range of different types of intermolecular interactions in both solution, liquid phase and solid samples, lead to broadband spectra, which may hinder the extraction of the desired structural information. In gas phase IR spectroscopy, on the other hand, the rotational bands that accompany the vibrational bands (resulting from the excitation of rotational movements) complicate the analysis of the spectra. In turn, by coupling infrared spectroscopy and matrix isolation narrowband spectra can be obtained since, as mentioned above, the molecular interactions felt by a matrix-isolated species are almost negligible, and consequently, there is a decrease of dispersion of vibrational levels (comparatively to other condensed phase conditions). Another factor that enhances the spectral resolution under matrix isolation conditions is that the vibrational spectra are not complicated by rotational effects, Doppler effects and presence of aggregates. [73,74] Since this combination is an excellent approach for simulating the gas phase but allowing to get rid of the major complications appearing under those experimental conditions, it makes possible the direct comparison of the experimental spectra with calculated spectra, in which the chemical species are usually considered to be *in vacuo*. On the whole, the multiple advantages of the combination of infrared spectroscopy with the matrix isolation method enable the extraction of detailed structural information about the molecular systems of interest.[23-39;75-81]

1.5.3 Matrix Effects

The physical conditions that are achieved under matrix isolation conditions are still the key for the exclusive capabilities of this technique. The inert trapping medium allows the molecular structures preservation and makes possible to obtain a detailed information about the molecular structures under investigation. However, there are some relevant physical and chemical effects, commonly referred as matrix effects that can influence the shape, intensity and frequency of the vibrational bands and that shall be considered during the results interpretation.[73,74]

It was referred above that matrix isolation IR spectra are not complicated by rotational movements. Nevertheless, the matrix environment does not avoid small molecules and small molecular fragments, as methyl groups, from rotating, leading to characteristic features in the spectra.

Another relevant phenomenon is the site splitting. Owing to the narrowband character of the matrix IR spectra, bands splits turn out to be more evident than in liquid or solid conventional IR spectra. The molecular species may be trapped by the matrix host in different orientations and in cavities with various morphologies. This leads to different matrix-guest interactions and may result in the splitting of the bands in multiplets. Other main causes for band splitting in the IR spectra are the molecular aggregation and Fermi resonances. Band split due to aggregation is a result of guest-guest interactions and can be identified by changing the matrix concentration or by annealing experiments. This makes the matrix isolation a powerful method to investigate some intermolecular interactions also (e.g., the study of dimers and small aggregates). Fermi resonance results in the appearance of pairs of bands in the vibrational spectra and may occur an overtone or combination mode has nearly the same frequency as a fundamental vibration of the same symmetry.

The cage effects are recognized to influence the paths of the reactions taking place in matrices and are relevant for experiments where several molecular species are produced. Excited molecules can deactivate through collisional processes or molecular fragments generated by photolysis can recombine to form other molecular entities. In a matrix, these last type of processes are cage confined and, as we will see, this fact was found to be very important in determining the characteristics of the photoinduced reactions described in this thesis.

1.5.4 Photochemistry in Cryogenic Inert Matrices

Matrix Isolation has been greatly succeeded when applied to the study of photochemical reactions.[76,78] The matrix-isolated species can be irradiated by near-IR, visible and UV light and the photoproducts stabilized in the rigid cages of the matrix. Once the processes taking place are monitored by IR spectroscopy, it is possible to identify and distinguish the photoproducts and, in many cases, elucidate the mechanism pathways of the photoinduced reactions. The most common, UV-induced photoprocesses are photoisomerizations and transformations that involve bond breaking/bond forming acts, such as photofragmentations and recombination processes. *In situ* irradiation of suitable matrix isolated-precursors with UV light has allowed the detection of high-energy photoproduced chemical species that in other conditions might be difficult to detected and characterize, such as high-energy conformers, unstable fragmentation products and new isomeric species, including rare tautomers.[23-39;78]

1.6 Raman Spectroscopy

Over the last decades, Raman spectroscopy has emerged as a powerful and versatile tool for chemical analysis and structural characterization, due to its sensitivity to molecular structure and molecular environment, its easy operation, and sampling. The use of Raman spectroscopy has now been extended to a great number of applications in materials science, biology, medicine and others domains. Moreover, the combination with the high spatial resolution of confocal microscopy, yielding molecular imaging, enhanced the range of applications of the technique. In this work, the confocal Raman microspectroscopy technique was used to investigate the solid state of the compounds presented in the first section of this thesis. Since it does not require additional samples preparation, changing the sample morphology (e.g. by applying pressure), Raman spectroscopy is a convenient technique to investigate desmotropy or polymorphism.

Although both infrared and Raman spectroscopy afford information about vibrational normal modes, the different vibrational excitation mechanism and different selection rules make them complementary techniques.[82,83;85-88]

In the case of Raman spectroscopy, the incident radiation does not need to have the same energy of the difference between the two vibrational levels to promote a vibrational excitation, as in the case of IR spectroscopy. In this case, the excitation mechanism occurs by inelastic scattering of light quanta with higher energy. This phenomenon is known by Raman scattering. The chemical species are irradiated with a monochromatic laser beam, which have quantized energy equal to $h\nu_0$ (visible, UV or near IR). Through

the inelastic impact of the laser beam with the molecular system, vibrational energy may be exchanged. Thus, the energy of light scattered, $h\nu_R$, corresponds to the difference or sum between the energy of incident, $h\nu_0$, and vibrational energy , $h\nu_s$, according to the following expression:

$$h\nu_R = h\nu_0 \mp h\nu_s \qquad (\mathbf{1.6.1})$$

The energy of quanta, $h\nu_R$, led to the Raman spectra. However, the Raman scattering is not the main process occurring, and has in fact a low probability. Another phenomenon, known by elastic scattering process, or Rayleigh scattering, has a much higher probability. In this case, the scattered light quanta have the same energy, $h\nu_0$, as the incident radiation.

Electrons and nuclei are forced to move in opposite directions when exposed to an electric field. Thus, a dipole moment is induced that is proportional to the electric field strength and molecular polarizability, α. A molecular vibration only can be observed in Raman spectroscopy if there is a change in the polarizability due to the vibration **(1.6.2)**.

$$\left(\frac{\partial \alpha}{\partial Q}\right)_0 \neq 0 \qquad (\mathbf{1.6.2})$$

1.7 X-ray Diffraction

X-ray diffraction (XRD) has become the classic method to obtain information about crystalline structures. As the typical interatomic distances in a crystal are a few angstroms, the wavelength of the probing radiation needs to be of same order of magnitude. Therefore, X-rays are ideal for structural investigations. In this work, suitable single crystals were grown and their structure was obtained by XRD.

Briefly, the main effect that occurs when an X-ray beam hits a crystal is scattering of the X-ray photons by the atoms. Although electrons and nuclei interact with electromagnetic waves, the contribution of electrons to that scattering is more effective due to their lighter masses. The structure determination requires the measurement of the spatial distribution of the scattered radiation from which the electron density can be determined. Since the crystal structure is periodic, the unit cell parameters can be determined from the XRD pattern.[83,89]

The diffraction patterns characteristic of crystalline samples can be well understood taking into account the simplest and intuitive explanation given by William Bragg and Laurence Bragg. The crystal can be regarded as a stacking of parallel planes of atoms (*h, k, l*) equally spaced by a distance, *d*. When a beam

of X-rays strikes the crystallographic planes, it is reflected and interference occurs between the waves reflected by the different planes. The condition for diffraction is known as Bragg's Law and is traduced in the following equation:

$$n\lambda = 2d \sin\theta \qquad (\mathbf{1.7.1})$$

where λ is the wavelength, θ is the angle of incidence of the beam, *n* is the order of reflection, i.e. *n* =1, 2, …, correspond to first, second,…, order maxima of the interference pattern. This law results from the constructive interference condition that the path length difference between the two incident waves has to be a multiple of the wavelength.

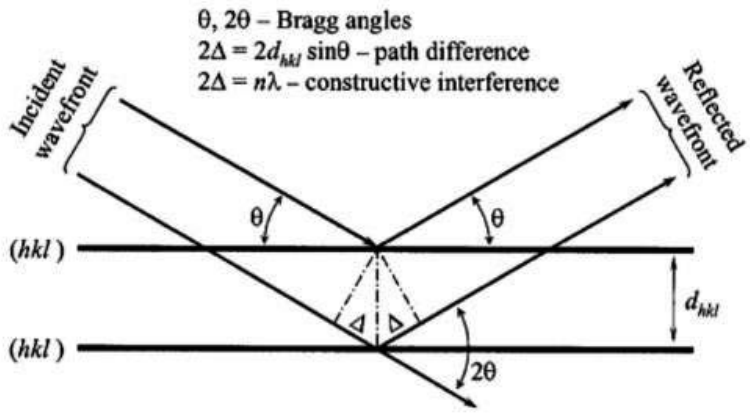

Figure 4. Illustration of Bragg reflection. The geometry for interference of a wave scattered from two planes similar spaced by a distance *d.* [89]

The scattered amplitude from the unit cell is denoted by F_{hkl} and is given by the following expression:

$$F_{hkl} = \sum_{j}^{N} f_j \, e^{[2i\pi(hx_j + ky_j + lz_j)]} \qquad (\mathbf{1.7.2})$$

where f_j is the atomic scattering factor for atom *j* in the unit cell, whose coordinates are respectively x_j, y_j, z_j. The intensity of the diffracted beam, I_{hkl}, is proportional to the square of the scattered amplitude from the unit cell **(1.7.3)**.

$$I_{hkl} \propto |F_{hkl}|^2 \qquad (\mathbf{1.7.3})$$

From the diffraction pattern it is possible to obtain the electronic density at each point of the crystal unit cell. The electronic density can be expressed as a Fourier series involving the structure factors:

$$\rho_{hkl} = \frac{1}{V} \sum_{hkl} F_{hkl}\, e^{-2\pi i(hx+ky+lz)} \qquad (\mathbf{1.7.4})$$

where the sum is extended to all the measured structure factors and *V* is the volume of the unit cell.

1.8 Polarized Light Thermal Microscopy

Polarized light thermal microscopy (PLTM) has a wide application in the characterization of solid state compounds. In this work, this technique was used to investigate tautomerism in solid state, with the aid of other techniques also described here.

PLTM allows the direct observation of samples submitted to heating/cooling programs. Therefore, it is very useful to determine the morphology of materials and observe the physical transformations that occur in the sample during the heating/cooling runs.[90,91] The direct observation is possible due to the use of polarized light microscopy, which is a contrast-inducing technique that improves the quality of image in the presence of anisotropic materials.[90] In anisotropic materials, the refractive index change with the direction of light propagation along the structure. Alternatively, in isotropic materials, such amorphous solids and crystalline solids with a cubic crystal system, the refractive index is the same along all directions of light propagation. PLTM is then a very useful (and powerful) technique for the identification of different phases.

The sample visualization offers an advantage in relation to differential scanning calorimetry (DSC), in which some physical transformations cannot be detected due to the low heat transfer involved in the process. Nevertheless, the DSC measurements are more accurate, and, in general, PLTM appears as a good complementary technique to perform a detailed thermal analysis of the substances.

1.9 Differential Scanning Calorimetry

Calorimetry is a very useful technique for measuring the thermal properties of materials, and is the only method that allows the direct measurement of the enthalpy of some processes making it possible to stablish a relation between temperature and specific properties.

Differential scanning calorimetry (DSC) means the measurement of the variation of the difference in the heat flow rate to the sample and to the reference as they are submitted to a controlled temperature program.[92]

To perform the experiments reported in this thesis a power compensation calorimeter, which belongs to the class of heat-compensating calorimeters, was used. In this type of equipment, the sample and reference are held in two independent holders, which are two small furnaces, each one with a temperature sensor and a heat font. The same temperature program is applied to both sample and reference (commonly empty) pans and the two are maintained at the same temperature. If an endothermic or exothermic transformation (or heat capacity change) occurs in the sample, a temperature difference between the small furnaces will arise. In order to maintain the condition of ΔT (difference between the temperature of the two pans) equal to zero, a compensating electrical heating power proportional to the temperature difference is applied. The obtained output signal is proportional to the differential heat flow rate.[93,94]

CHAPTER II

Chapter II. Materials and Methods

2.1 Samples

The compounds 2-mercaptoimidazole (crystalline; purity 98%), 2-mercaptobenzimidazole (powder; purity 98%), 1-methyl-2-mercaptoimidazole (powder; purity 97%), and 1-methyl-2-mercaptobenzimidazole (powder; purity 95%) were purchased from Sigma-Aldrich.

2.2 Computational Details

The density functional theory (DFT) calculations were performed with the Gaussian 09[95] software package. The B3LYP functional[63,64,66,67] together with the 6-311++G(d,p)[68] basis set, was used. Equilibrium geometries and harmonic frequency calculations were carried out using the same level of theory. Since several approximations are employed, the harmonic vibrational frequencies were scaled by a factor of 0.954, above 2700 cm^{-1}, and by 0.978 below this frequency. The normal modes were analyzed by carrying out potential energy distribution (PED) calculations using a modified version of the program BALGA, which implements computationally the methodology first described by Schachtschneider and Mortimer.[96] The internal symmetry coordinates used in this investigation were defined as suggested by Pulay et. al.[97] The aromaticity indexes were obtained using the program Multiwfn.[98]

2.3 Experimental Details

2.3.1 Matrix Deposition

To perform the matrix isolation experiments, the compounds were sublimated from a mini glass oven placed in the vacuum chamber of the cryostat (see **figure 5**). The resultant vapors were deposited

together with a large excess or argon (N60, supplied by Air Liquide) onto a CsI window cooled (10-15 K) by a closed-cycle helium refrigerator whose principal component is an APD Cryogenics DE-201A expander. The temperature of the CsI window was measured by a silicon diode temperature sensor connected to a digital temperature controller (Scientific Instruments, Model 9650-1). A pumping system whose main component is an Alcatel turbomolecular pump is connected to the cryostat in order to maintain the required high-vacuum in the system ($\leq 10^{-6}$ mbar).

Since the compounds are hygroscopic and exhibit great trend to aggregate, it was necessary to dry them before the experiments and take special care with the deposition conditions, such as argon outflow and rate of sublimation (2-mercaptoimidazole appears to be less hygroscopic than the remaining compounds and was easier to handle during the experiments).

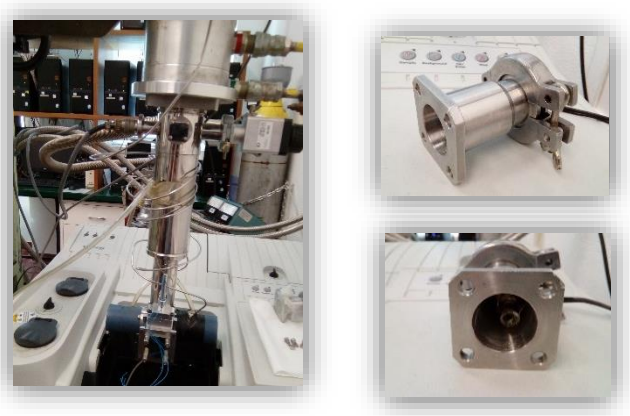

Figure 5. Matrix Isolation setup of the Laboratory for Molecular Cryospectroscopy and Biospectroscopy (LMCB).

2.3.2 Infrared Spectra

The infrared spectra of matrix isolated species were recorded in the 4000-400 cm^{-1} range, with 0.5 cm^{-1} resolution, using a Thermo Nicolet 6700 Fourier transform infrared (FTIR) spectrometer equipped with a deuterated triglycine sulphate (DTGS) detector and a Ge/KBr beam splitter. In order to avoid interferences from carbon dioxide and water, the optical path was purged by a stream of dry and filtered air.

2.3.3 UV Irradiation

The matrices were irradiated through a quartz window of the cryostat using a tunable narrowband UV light provided by an optical parametric oscillator (fwhm 0.2 cm^{-1}), pumped with a pulsed Quanta Ray Pro-Series Nd: YAG laser (repetition rate = 10 Hz, pulse energy 10 mJ, duration = 10 ns; see **figure 6**).

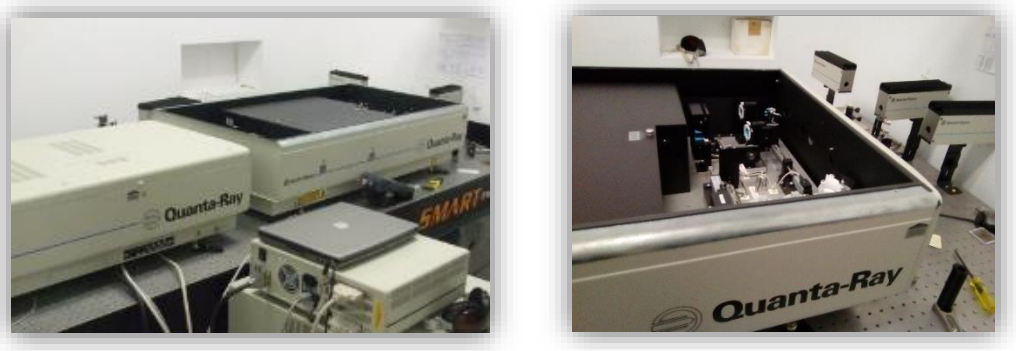

Figure 6. Pulsed Quanta Ray Pro-Series Nd: YAG laser and MOPO-SL Optical Parametric Oscillator of the LMCB laboratory.

2.3.4 Raman Spectra

The Raman spectra of single crystals were collected using a Raman micro-system (Horiba LabRam HR Evolution, equipped with a Synapse CCD detector, a high-stability BXFM open space confocal microscope, and a 600 gr mm^{-1} grating; see **figure 7**) in the 50-4000 cm^{-1} region. The excitation was promoted by a 633 nm Helium-Neon laser, with a power of approximately 17 mW at the sample. In these experiments, a 100x objective lens was used, resulting in a laser spot diameter of 0.8 µm.

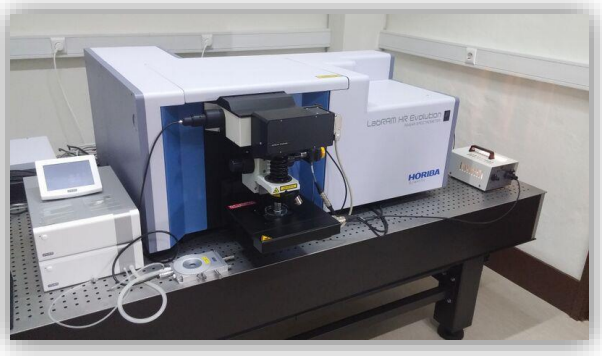

Figure 7. Horiba LabRam HR Evolution equipment of the LMCB laboratory.

2.3.5 Single-Crystal X-ray Diffraction

To perform the single crystal X-ray measurements a Bruker APEX II diffractometer was used, using graphite monochromated MoK$_\alpha$ ($\lambda = 0.71073$ Å) excitation. The absorption corrections were performed using the software SADABS,[99] and the structural refinements were performed using the SHELXL-2014/7 package.[100]

2.3.6 Polarized Light Thermal Microscopy

Polarized light thermal microscopy (PLTM) studies were obtained using a DSC 600 hot/cold stage from Linkam, which allow heating/cooling runs between −160 and 600 °C at rates from 0.1 to 130 °C/min. The optical observation instrumentation was a Leica DMBR microscope and an adapted video camera CCD-IRIS/RGB. To undertake image analyses, The Real Time Video Measurement System software from Linkam was used. The images were obtained by the use of polarized light and wave compensators, using a 200x magnification objective.

2.3.7 Differential Scanning Calorimetry

Differential scanning calorimetry (DSC) measurements were performed using a Pyris 1 power compensation calorimeter from Perkin-Elmer, with an intra-cooler cooling unit, working at a -25 ^{o}C (ethylene glycol-water, 1:1 v/v, cooling mixture), and a 20 mL min^{-1} nitrogen purge flow. Temperature and enthalpy calibrations were carried out using indium (PerkinElmer, Purity (%) = 99.99%, T_{fus} = 156.60 ^{o}C) and biphenyl (CRM LGC, T_{fus} = 68.93 ± 0.03 ^{o}C).[101] Samples were placed in hermetically sealed aluminum pans. The experiments were carried out using a scan rate β = 10 ^{o}C min^{-1} from 25 to 250 ^{o}C.

2.3.8 Recrystallization

The samples were recrystallized using different solvents. Solutions with different concentrations (3 – 25 cm^3 of solvent and 3 – 25 mg of sample) were prepared and allowed to evaporate at room temperature in petri dishes with different sizes. Tetrahydrofuran, ethanol, methanol, dioxane, water and 1,4-dicloromethane were the solvents used.

CHAPTER III

Chapter III. Structural Characterization of 2-Mercaptoimidazole, 2-Mercaptobenzimidazole and their 1-Methyl Substituted Derivatives

3.1 Introduction

In the first chapter of this thesis some chemical properties and applications of 2-mercaptoimidazoles (2-mercaptoimidazole and 1-methyl-2-mercaptoimidazole) and 2-mercapo-benzimidazoles (2-mercaptobenzimidazole and 1-methyl-2-mercaptobenzimidazole) were mentioned. These molecules can exhibit tautomerism, and may be exist as two tautomeric structures. It is well established that the tautomerism depends on the physical state, chemical environment, temperature and may be of different types.[10,15] Structural modifications, as substituents addition, may influence the tautomers stability and, then, tautomeric equilibria.

Although some studies on 2-mercaptoimidazoles and 2-mercaptobenzimidazoles have been reported, such as spectroscopic and X-ray diffraction investigations[103-106], there is still a lack of structural information about this type of nitrogen and sulphur containing heterocyclic molecules. In particular, the predominance of one tautomer over the other and the mechanism of tautomerization in different physical states or chemical environments still remain open to investigation. For such reasons, the starting point of this work consisted in the elucidation of structural properties of the isolated molecules and of mechanistic aspects related with the thiol-thione tautomerism.

The structural characterization of 2-mercaptoimidazoles (2-mercaptoimidazole and 1-methyl-2-mercaptoimidazole) and 2-mercaptobenzimidazoles (2-mercaptobenzimidazole and 1-methyl-2-mercaptobenzimidazole) was then undertaken by the combination of theoretical methods with matrix isolation infrared spectroscopy. First, the geometries, energies and vibrational spectra of the two tautomeric structures of the studied molecular systems were determined at the DFT(B3LYP)/6-311++G(d,p) level of theory, as referred in the first chapter of this thesis. The DFT/B3LYP method conjugated with the 6-311++G(d,p) basis set has been widely used in the LMCB, due to its accuracy in predicting structural parameters, thermochemical properties, infrared and Raman spectra.[79-81] The results obtained using the theoretical methods were then compared with experimental data. The observed

similarity of experimental and predicted vibrational spectra indicates that the theoretical approach used is appropriate for use in the vibrational analysis of the studied systems. The most relevant structural pieces of information obtained from both the calculations and experimental data will be discussed in the next sections.

3.2 Molecular Structure

According to the theoretical results for the electronic ground state, the thione tautomer is, for all the studied molecules, more stable than the thiol tautomer. The simplest molecule, whose structure served as a model for this overall investigation, is 2-mercaptoimidazole (2-MI), which is depicted in **figure 8.** The other three studied molecules differ from this one in the substituents, benzo or/and methyl groups, and the effect of substitution on the tautomers stability will be discussed in the present and in the next chapters.

2-Mercaptoimidazole

According to the calculations, 2-mercaptoimidazole thione tautomer (A in **figure 8**) is 33.9 kJ mol^{-1} more stable than the experimentally relevant form of the thiol tautomer (B). This value corresponds to electronic energy with zero-point vibrational correction. As shown below, some structure-energy relationships could be proposed from the analysis of the calculated geometrical parameters of the two tautomers.

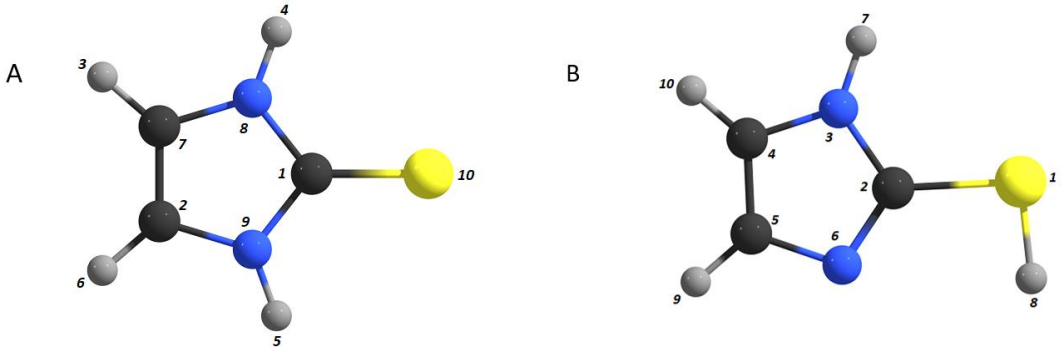

Figure 8. Structures of 2-mercaptoimidazole tautomers (with atom numbering) optimized at the DFT(B3LYP)/6-311++G(d,p) level of approximation. A) thione tautomeric form. B) thiol tautomeric form (lowest energy thiol structure).

The optimized geometrical parameters for thione 2-MI are presented in **table 1**. This tautomer has a planar equilibrium structure, with C_{2v} symmetry. In general, the geometry predicted for the isolated

molecule is very similar to that determined experimentally for crystalline 2-MI by X-ray diffraction.[102] One interesting result concerns the C=S bond length for the isolated molecule (1.672 Å, as shown in the **table 1**) and for the constituting monomeric unit of the crystal (1.702 Å).[102] These bond lengths are in the range of the values reported in the Cambridge Structural Database (CSD) for similar thiones (1.650 to 1.708 Å). Such values are typical for exocyclic thiones and demonstrate that the C=S bond in the thione 2-MI tautomer has, in fact, a predominantly double bond character. The longer bond length observed in the crystal, compared to that estimated for the isolated molecule, is a consequence of the involvement of the thione group in intermolecular H-bonding in the solid phase.

Table 1. Calculated structural parameters of C_{2v} 2-mercaptoimidazole thione (A).[a]

Bond Lengths /Å		**Angles /°**		**Dihedral Angles /°**	
C1-N8	1.373	N8-C1-N9	103.2	N9-C1-N8-H4	180.0
C1-N9	1.373	C1-N9-C2	111.7	N9-C1-N8-H7	0.0
N9-C2	1.390	C1-N8-C7	111.7	S10-C1-N8-H4	0.0
N8-C7	1.390	N9-C2-C7	106.7	S10-C1-N8-H7	180.0
C7-C2	1.352	N8-C7-C2	106.7	N8-C1-N9-C2	0.0
S10-C1	1.672	N9-C1-S10	128.4	N8-C1-N9-C2	180.0
N9-H5	1.007	N8-C1-S10	128.4	S10-C1-N9-C2	180.0
N8-H4	1.007	C1-N9-H5	121.5	S10-C1-N9-H5	0.0
C2-H6	1.076	C2-N9-H5	126.9	H6-C2-C7-H3	0.0
C7-H3	1.076	C1-N8-H4	121.5	H6-C2-C7-N8	180.0
		C7-N8-H4	126.5	N9-C2-C7-H3	180.0
		N9-C2-H6	122.6	N9-C2-C7-N8	0.0
		C7-C2-H6	130.6	H6-C2-N9-C1	180.0
		N8-C7-H3	122.6	H6-C2-N9-H5	0.0
		C2-C7-H3	130.6	C7-C2-N9-C1	0.0
				C7-C2-N9-H5	180.0
				C2-C7-N8-C1	0.0
				C2-C7-N8-H4	180.0
				H3-C7-N8-C1	180.0
				H3-C7-N8-H4	0.0

[a] See figure 8 for atom numbering.

Another important feature deserving here a comment is the predicted value for the ∡N-H···S angles. The DFT(B3LYP)/6-311++G(d,p) value is around 67.2°, which is considerably smaller than the ideal value for a typical proton donor/acceptor interaction (180°) and substantially smaller than the smaller value accepted for the ∡ D–H···A (D, donor; A, acceptor) angle compatible with the existence of a H-bond interaction.[106] This indicates that, in the studied molecule, no intramolecular N-H···S hydrogen bonds exist. Such result is in agreement with the electron density study reported by Minas da Piedade et al.,[102] using the Atoms in Molecules theory (AIM),[107] which failed to locate a bond critical point within the NH fragments and the S atom. In the case of the thiol tautomer of 2-MI, three minimum energy structures result from the internal rotation around the C-S bond, as shown in the potential energy profile presented in **figure 9**. The most stable conformation (I) predicted by the calculations is planar, belonging to the C_s symmetry point group (see Table 2 for geometric parameters). The other two energy minima belong to the C_1 point group and are symmetry equivalent structures (II, II'), with N6-C2-S1-H8 dihedral angles equal to 61° and -61°, respectively (the structural parameters for these forms are given in **Appendix**). However, the energy barrier separating structures II (or II') from the lowest energy minimum I is only 0.09 kJ mol^{-1}, i.e., it stays below the zero-point vibrational energy level of the torsional coordinate at the geometry of the higher-energy minima. For this reason, structures II/II' are not relevant in practical terms, being better described as vibrational excited states of the most stable conformer. The maximum energy structure along the torsional path exhibits also a planar structure, with an N6-C2-S1-H8 dihedral angle of 180°, as seen in **figure 9.**

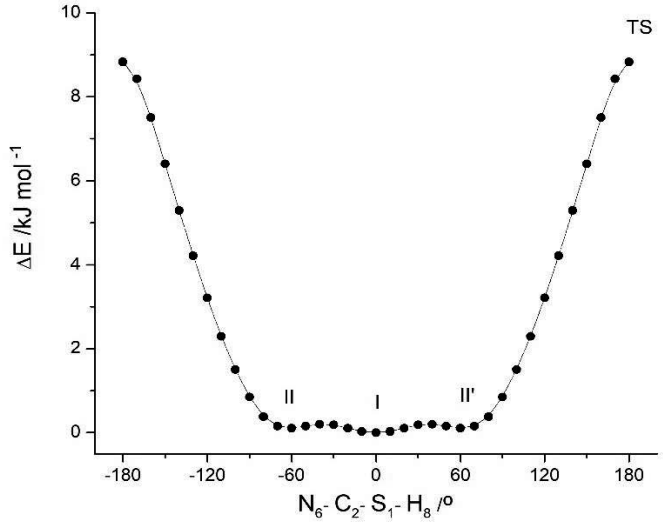

Figure 9. DFT(B3LYP)/6-311++G(d,p) potential energy profile for internal rotation about the C-S bond in the thiol tautomer of 2-MI. In the performed potential energy scan, the N6-C2-S1-H8 dihedral angle was incremented in 10° steps and all the remaining geometrical parameters optimized. The lowest energy form of thiol tautomer corresponds to the structure with the N6-C2-S1-H8 dihedral angle equal to 0°; in the two symmetry-equivalent higher energy minima this angle is ±61°.

In a similar way to what was found for the thione tautomer, also in the thiol form the structural data indicate that no intramolecular H-bonds exist. In this case, the ∢ S1-H8…N6 angle is 84.4°, i.e., also far from matching the criteria for existence of a hydrogen bond (see above). The enhanced stability of the C_s structure (form I) in the thiol tautomer (compared to the non-planar geometries, and also in relation to the highest energy transition state structure with H8-S1-C2-N6 dihedral angle equal to 180°) can be explained mostly in terms of through-space bond-dipole / bond-dipole interactions, as follows: in form I, the bond-dipoles associated with the two relevant opposing pairs of bonds, (S1–H8 and N6=C2) and (S1–C2 and N3–H7) are aligned nearly anti-parallelely (see **figure 10**), thus stabilizing the structure, while in the high-energy planar transition state these interactions are replaced by the strongly repulsive S1–H8 / N3–H7 interactions (both associated with the parallel alignment of the associated bond-dipoles, and steric and charge repulsions between the H8 and H7 atoms). The non-planar structures are, naturally, intermediate regarding the relevant intramolecular interactions just discussed, justifying their relative energies.

Table 2. Calculated structural parameters of the more stable form (C_s) 2-MI thiol tautomer (B).[a]

Bond Lengths /Å		**Angles /°**		**Dihedral Angles /°**	
C2-N6	1.311	C2-S1-H8	93.1	H8-S1-C2-N3	180.0
C2-N3	1.367	N3-C2-S1	121.5	H8-S1-C2-N6	0.0
N6-C5	1.382	N6-C2-S1	126.6	S1-C2-N3-C4	180.0
N3-C4	1.387	N3-C2-N6	111.9	S1-C2-N3-H7	0.0
C4-C5	1.366	C2-N3-C4	106.9	N6-C2-N3-C4	0.0
S1-H8	1.347	C2-N3-H7	126.7	N6-C2-N3-H7	180.0
C2-S1	1.770	C4-N3-H7	126.3	S1-C2-N6-C5	180.0
N3-H7	1.008	N3-C4-C5	105.1	S1-C2-N6-C5	0.0
C5-H9	1.078	N3-C4-H10	132.8	C2-N3-C4-C5	0.0
C4-H10	1.077	C3-C4-H10	122.1	C2-N3-C4-H10	180.0
		C5-C4-H10	132.8	H7-N3-C4-C5	180.0
		C4-C5-N6	110.7	H7-N3-C4H10	0.0
		C4-C5-H9	128.1	N3-C4-C5-N6	0.0
		N6-C5-H9	121.1	N3-C4-C5-H9	180.0
		C2-N6-C5	105.4	H10-C4-C5-N6	180.0
				H10-C4-C5-H9	0.0
				C4-C5-N6-C2	0.0
				H9-C5-N6-C2	180.0

[a] See figure 8 for atom numbering.

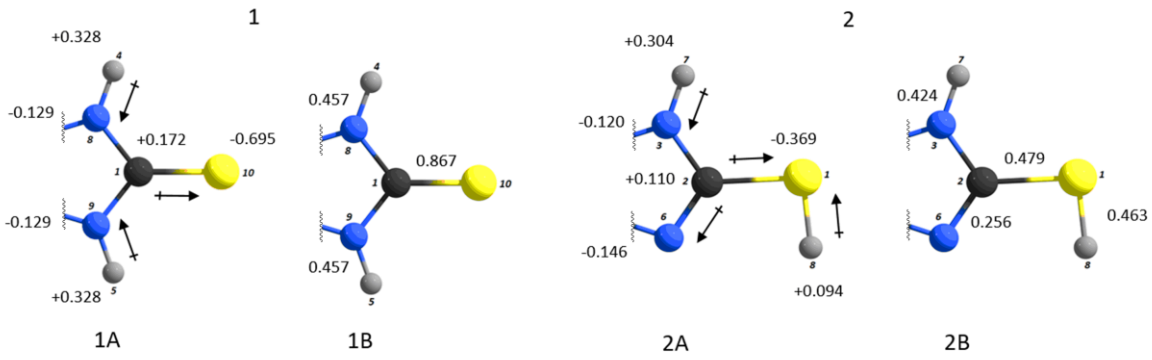

Figure 10. DFT(B3LYP)/6-311++G(d,p) Mülliken atomic charges (A) and difference between the charges of the atoms making a bond (B) of thione (1) and thiol (2) fragments of 2-MI tautomers. Charges in units of electron: 1e = 1.60217646 x 10^{-19} C.

Intramolecular interactions of bond-dipole / bond-dipole type are also the major effects determining the relative energies of the two tautomers of 2-MI. In **figure 10**, the dominant bond-dipole / bond-dipole interactions in the two tautomeric forms can be compared. It is easy to conclude that the stabilizing interactions involving anti-parallelely aligned bond-dipoles in the thione form are by far stronger than those observed for the thiol form, what results mainly from the large negative charges of the thione sulphur atom and large positive charges of the two H atoms connected to the nitrogens.

Another factor that shall be considered to explain the relative energy of the two tautomers is the degree of π-electron delocalization, as measured by the well-known aromaticity indexes, Harmonic Oscillator Model of Aromaticity (HOMA) index, defined by Kruszewski and Krygowsky,[108] and BIRD index,[109] which have been widely used in structural determinations.

The HOMA index is based on molecular geometry. It is defined as:

$$\mathrm{HOMA} = 1 - \sum_{i} \frac{\alpha_{i,j}}{N} \left(\mathrm{R_{Ref}} - \mathrm{R}_{i,j}\right)^2 \qquad (\mathbf{3.2.1})$$

where *N* is the total number of the atoms considered, *j* denotes the atom next to atom *i*, α and R_{Ref} are pre-calculated constants given in the original paper for each type of atom pair, and $R_{i,j}$ denotes the actual bond length between atoms *i* and *j*. If HOMA equals to 1, that means that the length of each bond is identical to the corresponding optimal value R_{Ref} and thus the ring is fully aromatic, while if HOMA equals to 0, that means the ring is completely nonaromatic. If HOMA is a significantly negative value, then the ring shows anti-aromaticity characteristics.

In the case of the BIRD index (*I*), the aromaticity is related not to bond lengths, but to bond orders, and the closer this index is to 100, the more aromatic is the system. It is defined as

$$I = 100\left[1 - \left(\frac{V}{V_k}\right)\right] \quad \textbf{(3.2.2)}$$

with

$$V = \frac{100}{\bar{N}}\sqrt{\frac{\sum_i \left(N_{i,j} - \bar{N}\right)^2}{n}} \quad (\mathbf{3.2.3})$$

and

$$N_{i,j} = \frac{a}{R_{i,j}} - b \quad (\mathbf{3.2.4})$$

where *n* is the total number of the bonds considered. *N* denotes Gordy bond order,[109] $\bar{N}$ is the average value of the *N* values, and *a* and *b* are predefined parameters for each type of bond. V_K is a pre-determined reference value of *V*, that for five and six-membered rings assumes the values 35 and 33.2, respectively.

The two indexes were calculated for all the studied molecular structures with the program Multiwfn,[98] based on the calculated DFT(B3LYP)/6-311++G(d,p) geometries. The results obtained for the 2-MI tautomers are presented in **table 3**. The results allow to conclude that both tautomers are stabilized by mesomerism, but the two indexes point to a larger stabilization by this effect of the thiol tautomer.

Table 3. HOMA and BIRD indexes for thiol and thione 2-MI tautomers determined at DFT(B3LYP)/6-311++G(d,p) level of theory.

	2-MI thiol	2-MI thione
HOMA		
Imidazole ring	0.85	0.76
BI		
Imidazole ring	59.6	53.5

2-Mercaptobenzimidazole

2-Mercaptobenzimidazole (2-MBI) is analogous to the compound previously discussed, but possesses a benzene ring fused to the 2-mercaptoimidazole heterocycle through the C=C bond. The equilibrium structures of the two tautomeric forms of 2-MBI are presented in the **figure 11**. The calculations predicted an energy difference of 44.6 kJ mol^{-1} between the most stable thione tautomer (C) and the thiol tautomer (D). This energy difference is higher by 10 kJ mol^{-1} than that found (33.9 kJ mol^{-1}) for the unsubstituted 2-mercaptobenzimidazole (2-MI; see previous section). The optimized geometrical parameters for the heterocyclic ring of the two tautomers of 2-MBI are presented in **tables 4 and 5.** According to the calculations, the thione tautomeric structure belongs to C_{2v} symmetry point group, and has all the atoms in the same plane.

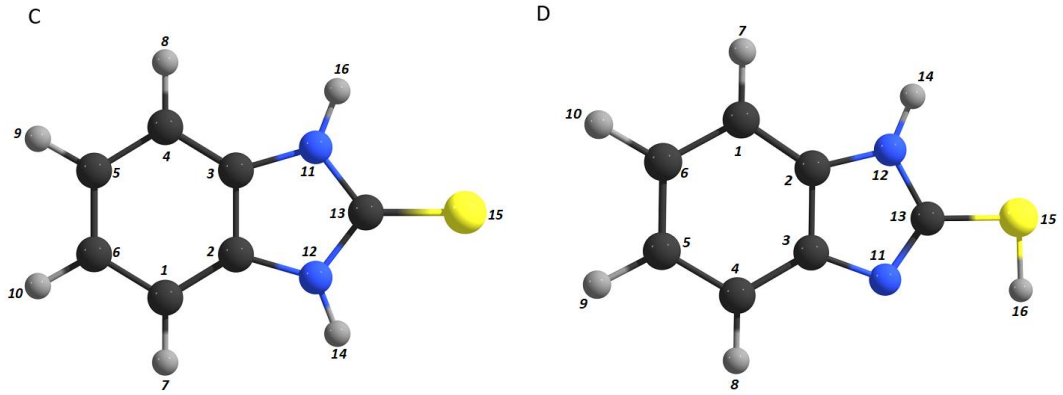

Figure 11. Structures of 2-mercaptobenzimidazole tautomers optimized at the DFT(B3LYP)/6-311++G(d,p) level of approximation. C) thione tautomeric form. D) thiol tautomeric form (less energetic conformation).

The same finding was obtained by X-ray diffraction for crystalline 2-MBI,[103] where the thione tautomer was found to be the sole tautomeric form present. Like for 2-MI, the estimated C=S bond length for the isolated molecule is somewhat shorter than that found in the crystal structure (1.664 vs. 1.671 Å, respectively), in view of the participation of the thione fragment as proton acceptor in the intermolecular H-bonding in the solid phase. Also, the calculated value for this bond length in 2-MBI is slightly smaller than that estimated for 2-MI (1.672 Å; see previous section), indicating that the C=S bond in 2-MBI has a larger double bond character than in the unsubstituted compound.

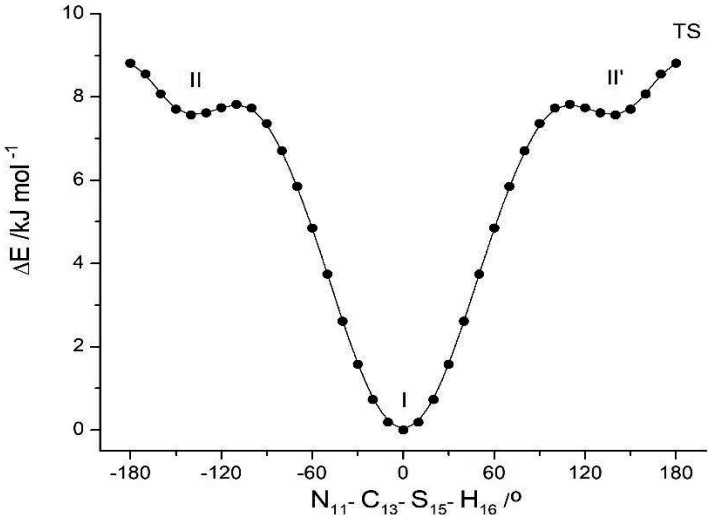

Figure 12. DFT(B3LYP)/6-311++G(d,p) potential energy profile for internal rotation about the C-S bond in the thiol tautomer of 2-MBI. In the performed potential energy scan, the N11-C13-S15-H16 dihedral angle was incremented in 10° steps and all the remaining geometrical parameters optimized. In the lowest energy form of thiol tautomer, the N11-C13-S15-H16 dihedral angle is equal to 0°; the structures II/II' are better considered as vibrational excited states of the most stable conformer, since the energy barrier that separates II/II' from I is only 0.25 kJ mol^{-1} (i.e., below the zero-point level of II/II'). In the two symmetry-equivalent higher energy minima the N11-C13-S15-H16 dihedral angle is ±139.4°.

Table 4. Calculated structural parameters of the heterocyclic ring of 2-MBI thione (C).[a]

Bond Lengths / Å		Angles /°		Dihedral Angles /°	
C2-C3	1.407	C3-C2-N12	106.1	N12-C2-C3-N11	0.0
N11-C13	1.377	C3-N11-H16	127.1	C3-C2-N12-C13	0.0
N11-H16	1.007	C13-N11-H16	121.2	C3-C2-N12-H14	180.0
N12-C13	1.377	C2-N12-C13	111.6	C2-C3-N11-C13	0.0
C12-H14	1.007	C2-N12-H14	127.1	C2-C3-N11-H16	180.0
C13-S15	1.664	C13-N12-H14	121.2	C3-N11-C13-N12	0.0
N11-C3	1.390	N11-C13-N12	104.5	C3-N11-C13-S15	180.0
N12-C3	1.390	N11-C13-S15	127.7	H16-N11-C13-N12	180.0
		C2-C3-N11	106.1	H16-N11-C13-S15	0.0
		C3-N11-C13	111.6	C2-N12-C13-N11	0.0
		N12-C13-S15	127.7	C2-N12-C13-S15	180.0
				H14-N12-C13-N11	180.0
				H14-N12-C13-S15	0.0

[a] See figure 11 for atom numbering.

Table 5. Calculated structural parameters of the heterocyclic ring of 2-MBI thiol (D).[a]

Bond Lengths / Å		Angles /°		Dihedral Angles /°	
C2-C3	1.413	C3-C2-N12	104.5	N12-C2-C3-N11	0.0
C2-N12	1.389	C2-C3-N11	110.3	C3-C2-N12-C13	0.0
C3-N11	1.391	C3-N11-C13	104.9	C3-C2-N12-H14	180.0
N11-C13	1.304	C2-N12-C13	106.6	C2-C3-N11-C13	0.0
N12-C13	1.378	C2-N12-H14	126.9	C3-N11-C13-N12	0.0
N12-H14	1.007	C13-N12-H14	126.5	C3-N11-C13-S15	180.0
C13-S15	1.766	N11-C13-N12	113.6	C2-N12-C13-N11	0.0
S15-H16	1.347	N11-C13-S15	126.1	C2-N12-C13-S15	180.0
		N12-C13-S15	120.2	H14-N12-C13-N11	180.0
		C13-S15-H16	93.2	H14-N12-C13-S15	0.0
				N11-C13-S15-H16	0.0
				N12-C13-S15-H16	180.0
				N12-C2-C3-N11	0.0

[a] See figure 11 for atom numbering.

In the case of the thiol tautomer, the results obtained for 2-MBI essentially mimic those of 2-MI. In particular, they predict the planar (C_s) conformation with the N12-C13-S15-H16 dihedral equal to 0° as the experimentally relevant structure, while accounting also for two equivalent-by-symmetry minima separated from the planar form by an energy barrier that stays below the zero-point level associated with the torsion about the C–S bond at the geometries of the higher-energy minima (see **Figure 12**).

The reasons determining the lower energy of the thiol tautomer of 2-MBI (in relation to other possible conformations differing by internal rotation around the C–S bond) are identical to those found for 2-MI and were discussed in details in the previous section. More interesting is to present here an explanation for the different relative energies of the thiol vs. thione tautomers in 2-MBI and 2-MI. As mentioned before, the energy difference increases by about 1.3 times in the benzosubstituted molecule (44.7 vs. 33.9 kJ mol^{-1}). Comparison of the charges on atoms defining the relevant bond-dipole interactions in the two tautomers for the two molecules (**figure 13**) cannot account for this difference, implying that the relative stabilization of the thione tautomer compared to the thiol form in 2-MBI shall relate predominantly with the relative importance of ring mesomerism. Indeed, while in 2-MI both the HOMA and BIRD aromaticity indexes yield the thiol form more aromatic than the thione (see **table 3**), in 2-MBI the trend is the opposite one when the BIRD index is considered (**table 6**). In turn, the HOMA index predict nearly equal aromaticity for the two tautomers (**table 6**), but, in any case, compared with the situation in 2-MI, the thione form is predicted relatively more aromatic than the thiol tautomer. It is appropriate to stress here that one does not intend to extract strictly quantitative conclusions but only present some

simple data that qualitatively may help to understand the factors determining the energetics of the different forms in the various studied molecules. As shown below, this qualitative description can also account properly for the results obtained for the investigated methyl-substituted 2-mercaptoimidazoles.

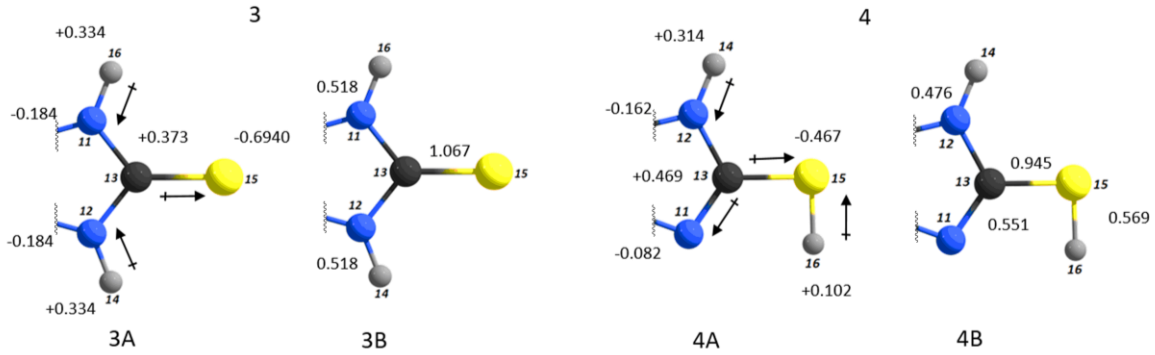

Figure 13. DFT(B3LYP)/6-311++G(d,p) Mülliken atomic charges (A) and difference between the charges of the atoms making a bond (B) of thione (3) and thiol (4) fragments of 2-MBI tautomers. Charges in units of electron: 1e = 1.60217646 x 10^{-19} C.

Table 6. HOMA and BIRD indexes for thiol and thione 2-MBI tautomers determined at DFT (B3LYP)/6-311++G(d,p) level of theory.

	2-MBI thiol	2-MBI thione
HOMA		
Phenyl ring	0.96	0.97
Imidazole ring	0.80	0.80
BI		
Phenyl ring	93.2	94.7
Imidazole ring	64.2	72.7

1-Methyl-2-Mercaptoimidazole

The substitution of the hydrogen directly linked to a nitrogen by a methyl group in 2-mercaptoimidazole results in an asymmetrically-substituted compound. As in the case of the other studied molecules, 1-methyl-2-mercaptoimidazole (1-M-2MI; commonly known as methimazole) may exist in two tautomeric forms, shown in **figure 14**. The optimized thione (E) and thiol (F) structures of 1-M-2MI differ in energy by 38.7 kJ mol^{-1}, the thione form being the most stable tautomer, as for the

previous molecules. Compared to 2-MI, the hydrogen substitution by the methyl group in 1-M-2MI leads to an increase of only 4.9 kJ mol^{-1} in the relative energy of the two tautomers. The optimized geometrical parameters of the thione and thiol 1-M-2-MI are shown in **tables 8** and **9**, respectively. The thione tautomer belongs to C_s symmetry point group. Also as both in 2-MI and 2-MBI molecules, only the thione tautomer structure of 1-M-2-MI was determined by X-ray diffraction, since this is the sole species present in the crystal of the compound.[104]

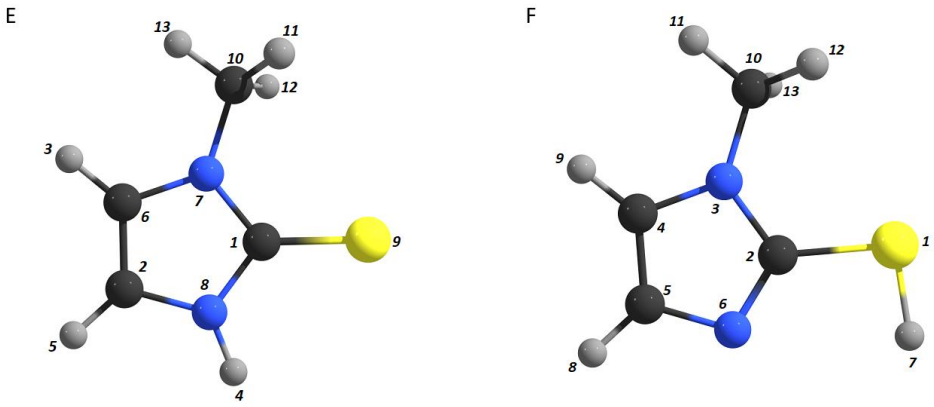

Figure 14. DFT(B3LYP)/6-311++G(d,p) optimized structures of 1-methyl-2-mercaptobenzimidazole tautomers. E) thione tautomeric form. F) thiol tautomeric form.

While in the case of the thione tautomer the structural results obtained for 1-M-2-MI are essentially similar to those obtained for 2-MI and 2-MBI (in particular the fact that the stable structure belongs to the C_s point group), the results obtained for the thiol tautomer are slightly different. According to the calculations, the 1-M-2-MI minimum energy structure belongs to C_1 symmetry point group, while for 2-MI and 2-MBI the thiol tautomer is planer (C_s). As it is possible to see in the potential energy profile presented in **figure 15** and also in the optimized geometrical parameters provided in **table 9**, 1-M-2-MI has two equivalent-by-symmetry minima (I and I'), whose N6-C2-S1-H7 dihedral angles are equal to 5.6 º and –5.6º (instead of 0º, as predicted for the other molecules). This subtle deviation, may be due to a non-correct prediction by the method used. In any case, even in the case the deviation from the planarity corresponds to a true structural feature, since the energy barrier separating the two equivalent non-planar structures is very small, staying below the zero-point vibrational level of these species, the practically relevant structure (most probable geometry) is the C_s symmetry form (see **figure 15**).

The explanation for the enhanced stability of the minimum energy structure of the thiol tautomer in relation to the high-energy transition state with N6-C2-S1-H7 dihedral angle equal to 180º is identical to that presented before for 2-MI and 2-MBI. However, as in 1-M-2-MI the substituent is a methyl group (instead of a hydrogen atom), the energy of the structure of this high-energy transition state is higher than that found for the analogue structures in 2-MI and 2-MBI, because of the increased steric repulsions

between the hydrogens of the methyl group and the sulfhydryl hydrogen. A similar explanation applies to justify the above mentioned increase of the relative energy of the two tautomers in the methyl-substituted compound compared to the unsubstituted molecule.

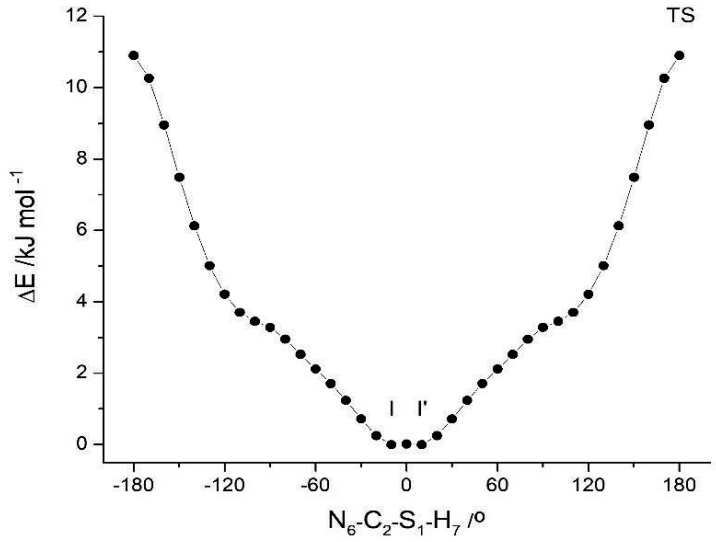

Figure 15. DFT(B3LYP)/6-311++G(d, p) potential energy profile for internal rotation about the C-S bond in the thiol tautomer of 1-M-2MI. In the performed potential energy scan, the N_6-C_2-S_1-H_7 dihedral angle was incremented in 10^o steps and all the remaining geometrical parameters were optimized.

The orientation of the methyl group in the thione and thiol optimized structures is another relevant structural feature to take into account. Indeed, the orientation of this group with the in-plane hydrogen atom pointing the opposite direction of the sulphur containing substituent, as shown in **figure 16** (see also **tables 8** and **9**), minimizes the repulsive interactions between these two fragments (either steric – in both tautomers –, or electrostatic – in the thiol form).

It shall also be pointed out that for 1-M-2MI the bond dipole / bond-dipole type intramolecular interactions also play the most important role in determining the relative energies of the two tautomers, while, as for 2-MI, the 1-M-2MI thiol tautomer is predicted to be somewhat more aromatic by both HOMA and BIRD indexes than the thione tautomer. In fact, the methyl group seems to practically not influence the aromaticity of the ring (compare data in **tables 7** and **3**). These results are also consistent with a relatively similar energy difference between the two tautomers predicted for 2MI and 1-M-2-MI (as already mentioned, 33.9 kJ mol^{-1} and 38.7 kJ mol^{-1}, respectively).

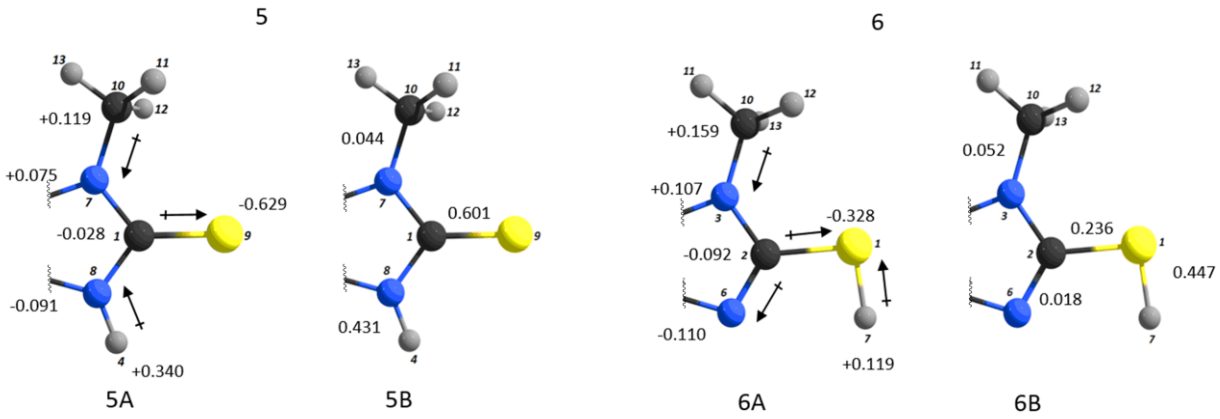

Figure 16. DFT(B3LYP)/6-311++G(d,p) Mülliken atomic charges (A) and difference between the charges of the atoms making a bond (B) of thione (5) and thiol (6) fragments of 1-M-2MI tautomers. Charges in units of electron: 1e = 1.60217646 x 10^{-19} C.

Table 7. HOMA and BIRD indexes for thiol and thione 1-M-2-MI tautomers determined at DFT(B3LYP)/6-311++G(d,p) level of theory.

	1-M-2-MI thiol	1-M-2MI thione
HOMA		
Imidazole ring	0.86	0.77
BI		
Imidazole ring	60.5	53.9

Table 8. Calculated structural parameters for 1-methyl-2-mercaptoimidazole thione (E).[a]

Bond Lengths / Å		Angles /°		Dihedral Angles / °	
C1-N7	1.375	N7-C1-N8	104.1	N8-C1-N7-C6	0.0
C1-N8	1.373	N7-C1-S9	128.2	N8-C1-N7-C10	180.0
C1-S9	1.676	N8-C1-S9	127.8	S9-C1-N7-C6	180.0
C2-H5	1.076	H5-C2-C6	130.7	S9-C1-N7-C10	0.0
C2-C6	1.353	H5-C2-N8	122.8	N7-C1-N8-C2	0.0
C2-N8	1.386	C6-C2-N8	106.5	N7-C1-N8-H4	180.0
H3-C6	1.076	C2-C6-H3	130.4	S9-C1-N8-C2	180.0
H4-C8	1.007	C2-C6-N7	107.6	S9-C1-N8-H4	0.0
C6-N7	1.391	H3-C6-N7	122.0	H5-C2-C6-H3	0.0
N7-C10	1.454	C1-N7-C6	110.4	H5-C2-C6-N7	180.0
C10-H11	1.091	C1-N7-C10	123.3	N8-C2-C6-H3	180.0
C10-H12	1.091	C6-N7-C10	126.2	N8-C2-C6-N7	0.0
C10-H13	1.090	C1-N8-C2	111.5	H5-C2-N8-C1	180.0
		C1-N8-H4	121.4	H5-C2-N8-H4	0.0
		C2-N8-H4	127.1	C6-C2-N8-C1	0.0
		N7-C10-H11	110.1	C6-C2-N8-H4	180.0
		N7-C10-H12	110.1	C2-C6-N7-C1	0.0
		N7-C10-H13	108.6	C2-C6-N7-C10	180.0
		H11-C10-H12	108.3	H3-C6-N7-C1	180.0
		H11-C10-H13	109.8	H3-C6-N7-C10	0.0
		H12-C10-H13	109.8	C1-N7-C10-H11	-59.7
				C1-N7-C10-H12	59.7
				C1-N7-C10-H13	180.0
				C6-N7-C10-H11	120.3
				C6-N7-C10-H12	-120.3
				C6-N7-C10-H13	0.0

[a] See figure 14 for atom numbering.

Table 9. Calculated structural parameters for 1-methyl-2-mercaptoimidazole thiol (F).[a]

Bond Lengths / Å		Angles / °		Dihedral Angles / °	
S1-C2	1.772	C2-S1-H7	92.8	H7-S1-C2-N3	174.6
S1-H7	1.347	S1-C2-N3	121.5	H7-S1-C2-N6	-5.6
C2-N3	1.368	S1-C2-N6	126.0	S1-C2-N3-C4	179.4
C2-N6	1.313	N3-C2-N6	112.6	S1-C2-N3-C10	1.8
N3-C4	1.388	C2-N3-C4	106.0	N6-C2-N3-C4	-0.4
N3-C10	1.455	C2-C3-C10	127.3	N6-C2-N3-C10	-178.1
C4-C5	1.367	C4-N3-C10	126.7	S1-C2-N6-C5	-179.7
C4-H9	1.077	N3-C4-C5	105.8	N3-C2-N6-C5	0.2
C5-N6	1.378	N3-C4-H9	121.6	C2-N3-C4-C5	0.5
C5-H8	1.079	C5-C4-H9	132.6	C2-N3-C4-H9	-179.8
		C4-C5-N6	110.6	C10-N3-C4-C5	178.2
		C4-C5-H8	128.1	C10-N3-C4-H9	-2.1
		N6-C5-H8	121.2	C2-N3-C10-H11	-164.3
		C2-N6-C5	105.1	C2-N3-C10-H12	-45.5
		N3-C10-H11	108.9	C2-N3-C1-H13	75.6
		N3-C10-H12	110.1	C4-N3-C10-H11	18.5
		N3-C10-H13	111.2	C4-N3-C10-H12	137.3
		H11-C10-H12	108.5	C4-N3-C10-H13	-101.7
		H11-C10-H13	109.0	N3-C4-C5-N6	-0.4
		H12-C10-H13	109.1	N3-C4-C5-H8	179.4
				H9-C4-C5-N6	179.9
				H9-C4-C5-H8	-0.3
				C4-C5-N6-C2	0.1
				H8-C5-N6-C2	-179.7

[a] See figure 14 for atom numbering.

1-Methyl-2-Mercaptobenzimidazole

The structures of 1-methyl-2-mercaptobenzimidazole (1-M-2-MBI) tautomers are presented in **figure 17**. For this molecule, the calculations predicted an energy difference of 49.8 kJ mol^{-1} between the thione (G) and the thiol (H) tautomer. When compared with the value obtained for 2-MBI (44.6 kJ mol^{-1}) this value increases by 5.2 kJ mol^{-1}, i.e., the introduction of the methyl group in the benzosubstituted 2-mercaptoimidazole leads to an increase of the energy difference between the two tautomers similar to that resulting from the methyl substitution in 2-MI. This result demonstrates that the methyl substitution does not affect strongly the properties of the ring-system, as already pointed out above.

On the whole, the energy difference between thiol and thione forms in 1-M-2-MBI is the highest among all the studied molecules.

The optimized geometry parameters for the two tautomers of 1-M-2-MBI are presented in **tables 10** and **11**. According to the performed calculations, the thione structure belongs to C_s symmetry point group. The molecule was also found to adopt the same configuration in the crystalline state of the compound, as determined by X-ray diffraction.[105] As for the other studied molecules, the thione tautomer is the single form existing in the crystal. Furthermore, also as in the other molecules, the C=S bond length now calculated for the isolated thione molecule is shorter than that observed in the crystalline state (1.684 Å),[105] due to the involvement of the sulphur atom as proton acceptor in intermolecular H-bonding interactions in the solid state.

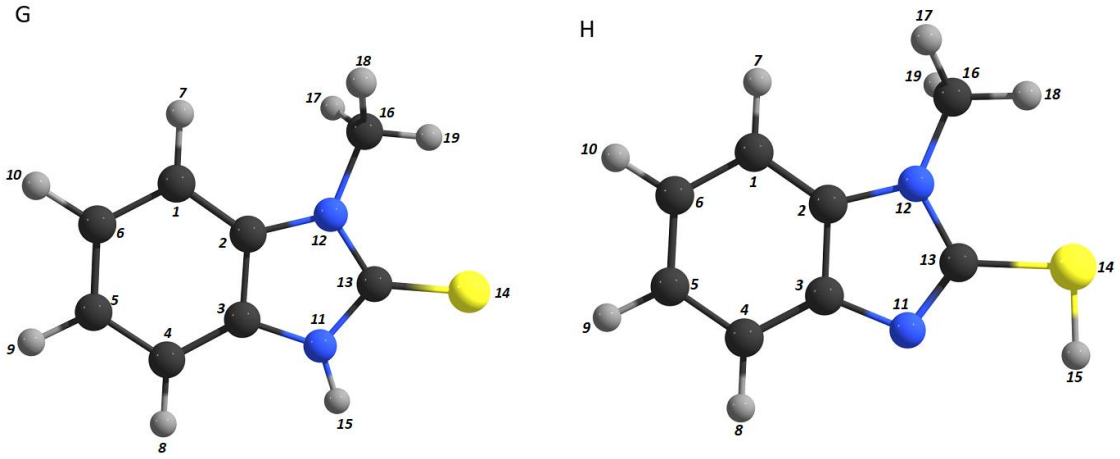

Figure 17. DFT(B3LYP)/6-311++G(d,p) optimized structures of 1-methyl-2-mercaptobenzimidazole tautomers. G) thione tautomeric form. H) thiol tautomeric form (less energetic conformation).

The thiol tautomer exhibits structural features similar to those found for 1-M-2-MI, in particular in what concerns the fact that the minimum energy structures correspond to a symmetry-related pairs of C_1 symmetry forms separated from each other by a very low energy barrier (see **figure 18**). The minimum

structures possess N11-C13-S14-H15 dihedral angles of 3.8/-3.8º and 129.4/-129.4 º as it possible to see in **figure 18**.

A common structural feature to both tautomers of 1-M-2-MBI is the orientation of the methyl group, which differs from that observed for 1-M-2-MI. As stressed above, in this later molecule, the methyl group is oriented in such a way that the hydrogen atom placed in the molecular plane points away from the sulphur substituent, in order to minimize the methyl/S steric repulsions. On the other hand, in 1-M-2-MBI, the methyl hydrogen atom placed in the molecular plane points towards the sulphur substituent (compare **figures 17** and **14**), because in this molecule the presence of the benzosubstituent introduces stronger steric repulsions (in particular between H7 and the in-plane methyl hydrogen) when the methyl orientation is similar to that found in 1-M-2-MI.

Globally, the structural and energetic results obtained for 1-M-2-MBI follow the trends found for the other molecules and show the effects of the simultaneous presence in the molecule of the benzo and methyl substituents (see also the calculated charges, bond dipoles and aromaticity indexes calculated for this molecule shown in **figure 19** and **table 12**), discussed in details above when describing the properties of the 2-MBI and 1-M-2-MI molecules, respectively. What shall be pointed out here is that the effects of the substituents are essentially additive and do not appear to show synergetic effects.

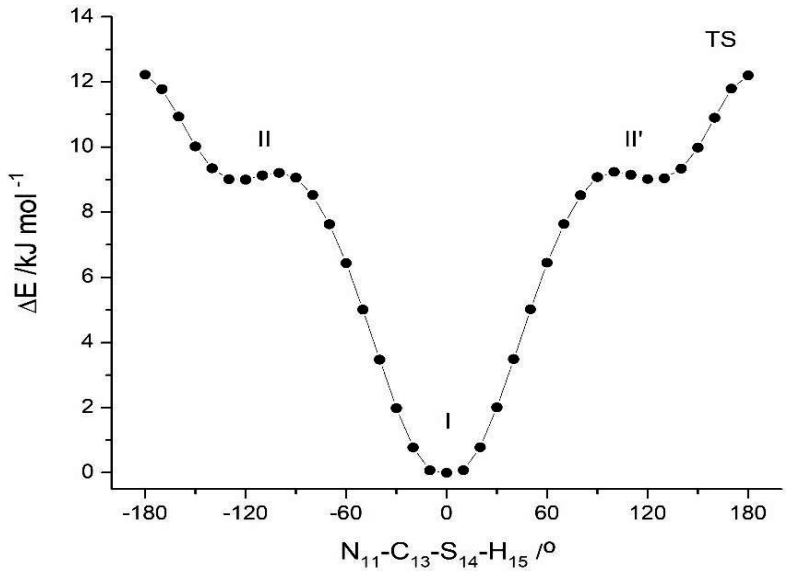

Figure 18. DFT(B3LYP)/6-311++G(d,p) potential energy profile for internal rotation about the C-S bond in the thiol tautomer of 1-M-2MBI. In the performed potential energy scan, the N11-C13-S14-H15 dihedral angle was incremented in 10 º steps and all the remaining geometrical parameters optimized. The structures II/II' are better considered as vibrational excited states of the most stable conformer is below the zero-point level of II/II'. In the two symmetry-equivalent higher energy minima the N11-C13-S14-H15 dihedral angle is ±129.4º.

Table 10. Calculated structural parameters of the heterocyclic ring of 1-M-2-MBI thione (G).[a]

Bond Lengths / Å		Angles /°		Dihedral Angles / °	
C2-C3	1.406	C3-C2-N12	107.1	N12-C2-C3-N11	0.0
C2-N12	1.392	C2-C3-N11	105.8	C3-C2-N12-C13	0.0
C3-N11	1.386	C3-N11-C13	111.6	C3-C2-N12-C16	180.0
N11-C13	1.377	C3-N11-H15	127.3	C2-C3-N11-C13	0.0
N11-H15	1.007	C13-N11-H15	121.1	C2-C3-N11-H15	180.0
N12-C13	1.382	C2-N12-C13	110.3	C3-N11-C13--N12	0.0
N12-C16	1.451	C2-N12-C16	125.0	C3-N11-C13-S14	180.0
C13-S14	1.668	C13-N12-C16	124.7	H15-N11-C13-N12	-180.0
C16-H17	1.093	N11-C13-N12	105.2	H15-N11-C13-S14	0.0
C16-H18	1.093	N11-C13-S14	126.2	C2-N12-C13-N11	0.0
C16-H19	1.089	N12-C13-S14	128.6	C2-N12-C13-S14	180.0
		N12-C16-H17	110.3	C16-N12-C13-N11	180.0
		N12-C16-H18	110.3	C16-N12-C13-S14	0.0
		N12-C16-H19	107.8	C2-N12-C16-H17	-60.5
		H17-C16-H18	109.5	C2-N12-C16-H18	60.5
		H17-C16-H19	109.5	C2-N12-C16-H19	180.0
		H18-C16-H19	109.5	C13-N12-C16-H17	119.5
				C13-N12-C16-H18	-119.5
				C13-N12-C16-H19	0.0

[a] See figure 17 for atom numbering.

Table 11. Calculated structural parameters of the heterocyclic ring of 1-M-2-MBI thiol (H).[a]

Bond Lengths / Å		Angles /°		Dihedral Angles /°	
C2-C3	1.412	C3-C2-N12	105.3	N12-C2-C3-N11	-0.5
C2-N12	1.390	C2-C3-N11	110.1	C3-C2-N12-C13	0.7
C3-N11	1.388	C3-N11-C13	104.7	C3-C2-N12-C16	178.5
N11-C13	1.307	C2-N12-C13	105.6	C2-C3-N11-C13	0.1
N12-C13	1.380	C2-N12-H16	126.0	C3-N11-C13-N12	0.3
N12-C16	1.452	C13-N12-H16	128.3	C3-N11-C13-S14	-179.7
C13-S14	1.770	N11-C13-N12	114.2	C2-N12-C13-N11	-0.6
S14-H15	1.347	N11-C13-S14	124.9	C2-N12-C13-S14	179.3
C16-H17	1.092	N12-C13-S14	120.8	C16-N12-C13-N11	-178.4
C16-H18	1.090	C13-S14-H15	92.6	C16-N12-C13-S14	1.6
C16-H19	1.094	N12-C16-H17	109.7	C2-N12-C16-H17	46.7
		N12-C16-H18	109.7	C2-N12-C16-H18	165.4
		N12-C16-H19	111.2	C2-N12-C16-H19	-74.1
		H17-C16-H18	108.1	C13-N12-C16-H17	-135.9
		H17-C16-H19	109.1	C13-N12-C16-H18	-17.3
		H18-C16-H19	108.9	C13-N12-C16-H19	103.2
				N11-C13-S14-H15	-3.8
				N12-C13-S14-H15	176.2

[a] See figure 17 for atom numbering.

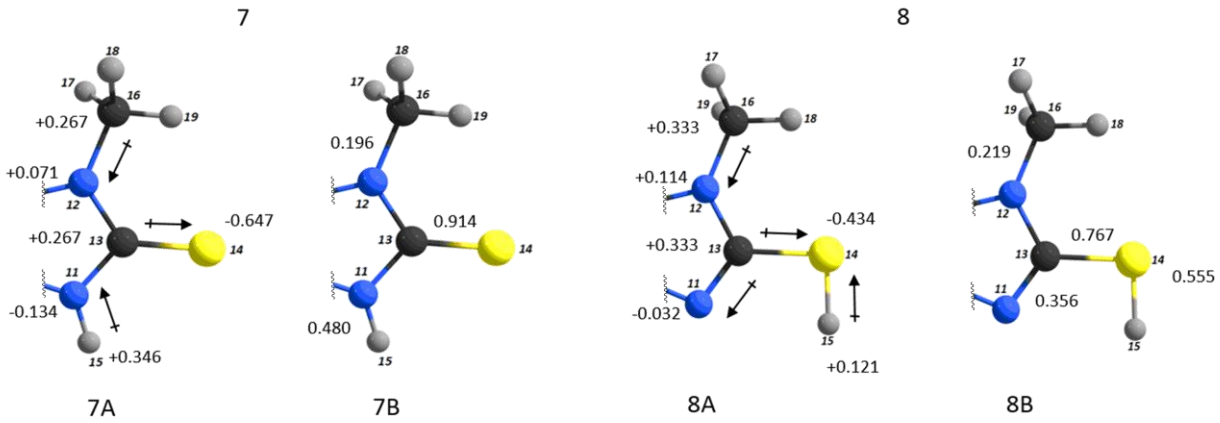

Figure 19. DFT(B3LYP)/6-311++G(d,p) Mülliken atomic charges (A) and difference between the charges of the atoms making a bond (B) of thione (7) and thiol (8) fragments of 1-M-2MBI tautomers. Charges in units of electron: 1e = 1.60217646 x 10^{-19} C.

Table 12. HOMA and BIRD indexes for thiol and thione 1-M-2-MBI tautomers determined at the DFT (B3LYP)/6-311++G(d,p) level of theory.

	1-M-2-MBI thiol	1-M-2-MBI thione
HOMA		
Phenyl ring	0.96	0.97
Imidazole ring	0.80	0.79
BI		
Phenyl ring	93.5	95.0
Imidazole ring	64.9	72.1

3.3 Matrix Isolation Infrared Spectroscopy

The molecules under study were investigated by matrix isolation infrared spectroscopy. The obtained results were analyzed and interpreted with the aid of harmonic frequencies calculated by the FG method with data extracted from the DFT(B3LYP)/6-311++G(d,p) results. Since the compounds are very hygroscopic, they had to be dried first for some hours in vacuo (at ~10^{-6} mbar). After this process, the compounds, placed in a mini-glass oven attached to the vacuum chamber, were sublimated (~380-390 K) and the vapors were then condensed onto an optical cold (10-15 K) CsI window, simultaneously with a large excess of argon (~1:1000 solute to matrix ratio). All but the simplest compound, 2-mercaptoimidazole, exhibit also a great trend to aggregate. It was then necessary to take special care in defining the deposition conditions, such as the rates of argon outflow and of sublimation. This task proved to be rather difficult, requiring a considerable number of experiments to achieve the ideal conditions to obtain good-quality infrared spectra of well-isolated monomers.

All the matrix isolation instrumentation and procedures are described in detail in Chapter 2 of this thesis.

The experimental results that will be discussed here proved that the thione form was the only tautomer that exists in the low temperature matrices immediately after deposition, which is in accordance with the calculations performed for the isolated molecule in vacuo.

2-Mercaptoimidazole

To perform the matrix isolation experiments, the compound was sublimated in vacuo at approximately 380 K. The IR spectrum of 2-MI isolated in argon (15 K) along with the theoretical spectra of the two 2-MI tautomers is presented in **figure 20**. Since the calculated harmonic frequencies for the studied systems show systematic deviations in relation to the experimental values (this is also due to other approximations of the used theoretical method, e.g., basis set limitation), appropriate scale factors were used to improve the agreement of the results. For all the experiments performed in this work, the calculated vibrational frequencies were scaled by a factor of 0.954, above 2700 cm^{-1}, and by 0.978 below this frequency.

The theoretical spectra predicted for the thione and thiol tautomers are substantially distinct, thus making easy to distinguish these species experimentally. In fact, the comparison of the spectrum of the as-deposited matrix with the theoretical data for the two tautomers led to the unequivocal conclusion that the thione was the sole 2-MI tautomeric species present in the matrix after deposition. Indeed, it is clear from **figure 20** that the predicted spectrum of the thione form fits very well the experimental spectrum, while that of the thiol tautomer shows a distinct profile. This result is also in agreement with the calculated relative energies of the two tautomers (the thione form was found to be 33.9 kJ mol^{-1} lower in energy than the thiol tautomer; see above).

The molecule of 2-mercaptoimidazole has 10 atoms, which results in 24 normal modes of vibration. In the case of thione 2-MI, which has a C_{2v} planar structure, 21 of the 24 normal modes are active in the infrared, while all modes are active in Raman. **Table 25** (in **Appendix**) presents the definition of the internal coordinates used in the performed normal mode analysis of 2-MI thione and their forms. **Table 13** provides the assignment of the spectra, with the calculated potential energy distribution (PED) resulting from the normal coordinate analysis.

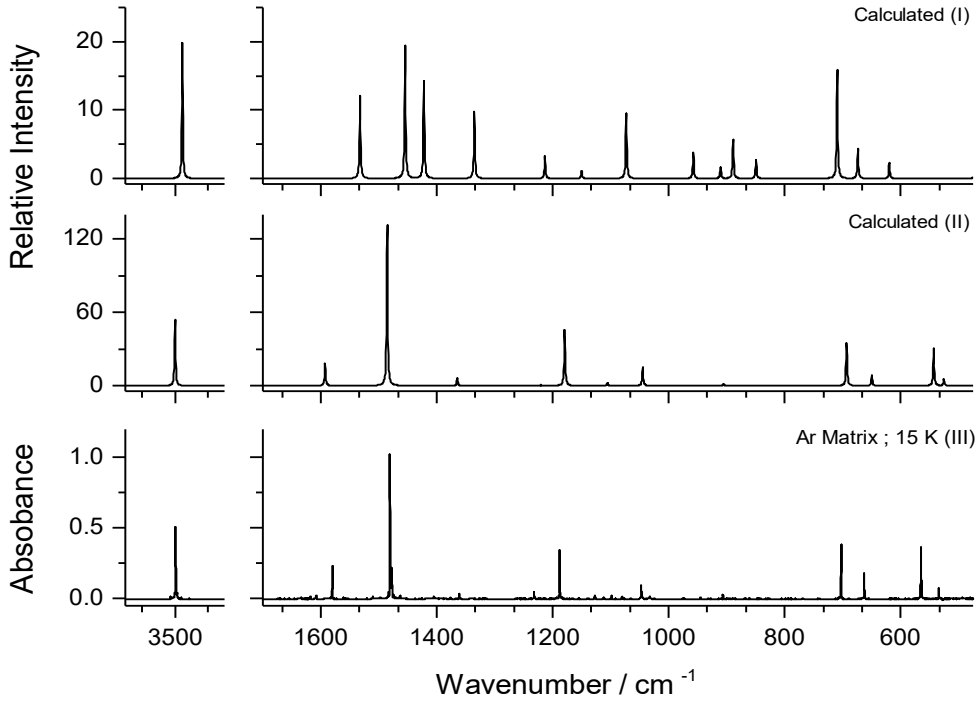

Figure 20. Experimental infrared spectrum of 2-MI isolated in an argon matrix at 15 K (III) compared with the DFT/(B3LYP)6-311++G(d,p) calculated spectra (scaled) of thione and thiol tautomers (II and I, respectively). The calculated spectra were simulated by Lorentzian functions. The calculated intensities of the simulated bands correspond to the areas below the Lorentzian functions.

Table 13. Experimental and calculated DFT(B3LYP)/6-311G++(d,p) frequencies of 2-MI and Potential Energy Distributions (PED).[a]

Experimental	**Calculated**			
$\tilde{\nu}^b$	$\tilde{\nu}^b$	$I_{IR}{}^c$	Sym.	PED[d]
3508/ 3499/ 3496/3487	3501	0.004	A_1	$\nu(NH)_s$ (100)
	3500	181	B_2	$\nu(NH)_{as}$ (100)
3193	3143	0.1	A_1	$\nu(CH)_s$ (99)
3158	3123	3	B_2	$\nu(CH)_{as}$ (100)
1580	1593	58	A_1	ν(C=C) (58) + $\delta(NH)_s$ (18) + $\delta(CH)_s$ (17)
1483/ 1480/ 1478/1474	1486	413	A_1	$\delta(NH)_s$ (32) + $\nu(CN)_s$ (21) + ν(C=C) (13) + $\nu(NC)_s$ (13) + $\delta(ring)_1$ (12)
1405	1395	0.3	B_2	$\delta(CH)_{as}$ (33) + $\nu(NC)_{as}$ (34) + $\delta(NH)_{as}$ (23)
1366	1365	19	B_2	$\delta(NH)_{as}$ (50) + $\nu(CN)_{as}$ (23) + $\delta(CH)_{as}$ (21)
1232/ 1231	1220	2	B_2	$\nu(CN)_{as}$ (55) + $\delta(CH)_{as}$ (18) + $\delta(NH)_{as}$ (12)
1188/ 1187	1179	146	A_1	$\nu(NC)_s$ (34) + ν(C=S)(25) + $\nu(CN)_s$ (25) + $\delta(NH)_s$ (14)
1128/1126 ?	1128	0.1	A_1	$\delta(CH)_s$ (64) + ν(C=C) (18)
1099	1106	7	A_1	$\nu(NC)_s$ (46) + $\delta(NH)_s$ (34) + ν(C=C) (10)
1047/ 1046	1045	50	B_2	$\nu(NC)_{as}$ (58) + $\delta(CH)_{as}$ (26) + $\delta(NH)_{as}$ (13)
945	946	0.8	A_1	δ_1(ring) (47) + $\nu(CN)_s$ (30) + $\delta(CH)_s$ (18)
906	906	5	B_2	δ_2(ring) (86) + $\nu(CN)_{as}$ (11)
-	813	-	A_2	$\gamma(CH)_{as}$ (113.6)
703	693	115	B_1	$\gamma(CH)_s$ (63) + $\tau(ring)_2$ (25) + γ(C=S) (12)
663	650	23	B_1	γ(C=S) (42) + $\tau(ring)_2$ (30) + $\gamma(CH)_s$ (29)
-	608	-	A_2	$\tau(ring)_1$ (100)
565/ 564	543	98	B_1	$\gamma(NH)_s$ (100) + γ(C=S) (10)
534	525	17	A_1	ν(C=S) (56) + $\delta(ring)_1$ (29) + $\nu(CN)_s$ (11)
-	482	-	A_2	$\gamma(NH)_{as}$ (92) + $\tau(ring)_1$ (10)
n.i	316	0.8	B_2	δ(C=S) (89)
n.i	201	3	B_1	$\tau(ring)_2$ (66) + γ(C=S) (36)

[a] See table 25 (Appendix) for the definition of symmetry coordinates. Abbreviations: s, symmetric; as, anti-symmetric; ν, stretching; δ, in-plane bending; γ, out-of-plane bending; [b] Wavenumbers in cm^{-1}; n.i., not investigated. [c] IR intensities in km mol^{-1}. [d] PED's lower than 10% are not shown.

2-Mercaptobenzimidazole

To perform the matrix isolation experiment, the compound was deposited at 10 K, following the general procedure used in the studies reported in this thesis.

The experimental infrared spectrum of the 2-MBI isolated in argon is presented in **figure 21**, where it may be compared with the calculated spectra of the two tautomers. As for the unsubstituted mercaptoimidazole (2-MI), the results clearly show that only the thione tautomer of 2-MBI is present in the deposited matrix. The reproduction of the experimentally obtained spectrum by the calculated one for this tautomer is excellent, both regarding the frequencies and band intensities. On the other hand, no features could be identified in the experimental spectrum that could be assigned to the thiol tautomer. At first sight, observation of two low-intensity bands at 1410 and 1450 cm^{-1} rose the question of presence of the thiol tautomer in the matrix in trace amounts, since these two bands appear at the approximate positions of the two most intense predicted bands of this species. However, we could safely rule out this by taking into account the results obtained in the photochemical experiments (described in Chapter IV of this thesis in detail), where the full vibrational signature of the thiol tautomer could be obtained.

It is also interesting to note that for this molecule the experimental spectrum evidences extensive site-splitting, with most of the bands exhibiting multiplet structure. Particularly striking site-splitting occurs in the 1492-1483 cm^{-1} region, where the observed bands are also broader than all the others in the spectrum. The bands in this spectral region are assigned to the δNH symmetrical bending, and the extended site-splitting and broadening can then be easily explained considering the involvement of the NH moieties in specific interactions with the host matrix atoms, which reflects in its high sensitivity to local environment. Extensive site splitting is also noticeable in the case of the features observed in the 1362-1356 and 1141-1137 cm^{-1} spectral ranges, which correspond to vibration exhibiting also relevant contributions from the δNH bending coordinates (either symmetrical or anti-symmetrical bendings), the same applying also to the features ascribed to the νNH stretching vibration, in the 3495-3488 cm^{-1} region.

The molecule of 2-mercaptobenzimidazole has 16 atoms which give rise to 42 normal modes of vibration. The C_{2v} symmetry of the as-deposited 2-MI thione tautomeric form led to 36 normal modes active in the infrared. The internal coordinates used in the normal modes description of the 2-MBI thione are shown in **table 26** (see **Appendix**). The spectral attributions, together with the calculated energy distribution (PED), are shown in **table 14.**

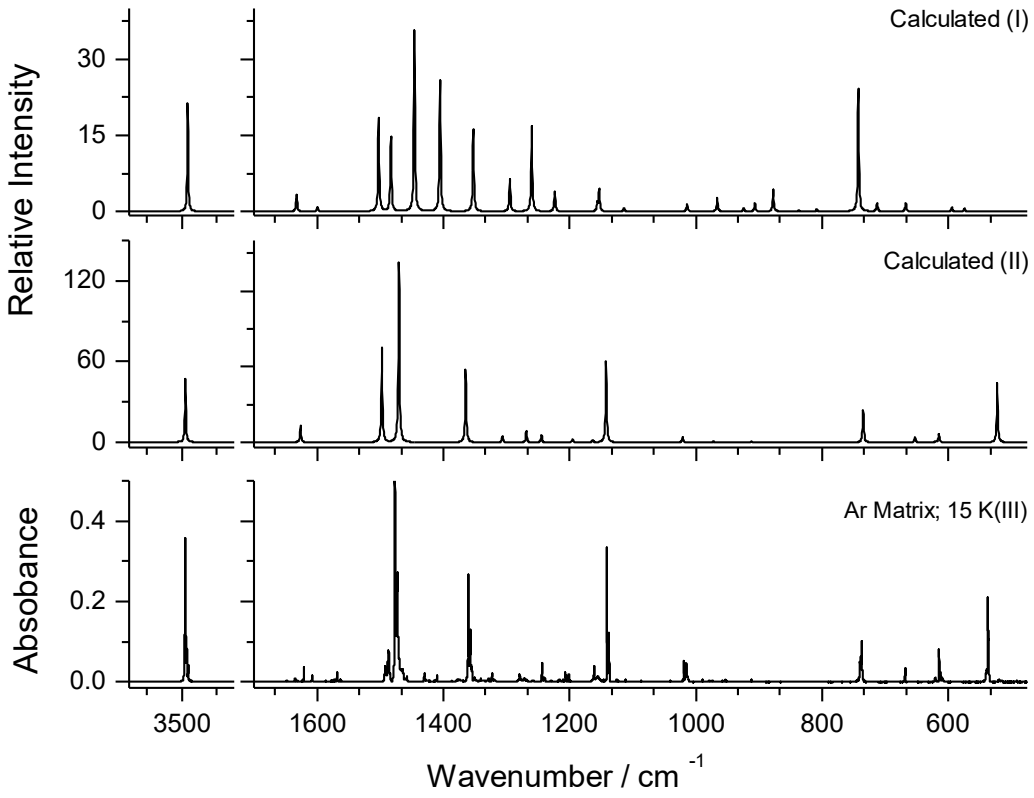

Figure 21. Experimental infrared spectrum of 2-MBI isolated in an argon matrix at 15 K (III) compared with the DFT(B3LYP)/6-311++G(d,p) calculated spectra of thione and thiol tautomers (II and I, respectively). The calculated spectra (scaled) were simulated by Lorentzian functions. The calculated intensities of the simulated bands correspond to the areas below the Lorentzian functions.

Table 14. Experimental and calculated DFT(B3LYP)/6-311G++(d,p) frequencies of 2-MBI thione and Potential Energy Distributions (PED).[a]

Experimental (Ar Matrix)	**Calculated**			
$\tilde{\nu}^b$	$\tilde{\nu}^b$	$I_{IR}{}^c$	Sym.	PED[d]
3495/3493/3490/3488	3495	8	A_1	$\nu(NH)_s$ (100)
	3493	145	B_2	$\nu(NH)_{as}$ (100)
3081	3053	7	A_1	$\nu(CH)_1$ (96)
3077	3045	12	B_2	$\nu(CH)_3$ (92)
3072/3071/3069	3037	5	A_1	$\nu(CH)_2$ (97)
	3029	0.006	B_2	$\nu(CH)_4$ (93)
1622	1631	1	B_2	$\nu(CC)_3$ (60)
1621	1626	42	A_1	$\nu(CC)_1$ (27) + $\nu(CC)_5$ (25) + $\nu(CC)_6$ (15)
1492/1488/1487/1483	1497	235	A_1	$\delta(NH)_s$ (33) + $\delta(CH)_1$ (27) + $\nu(NC)_s$ (16)
	1495	0.1	B_2	$\nu(CC)_4$ (26) + $\delta(CH)_3$ (26) + $\delta(ring2)_1$ (10)
1478/1477/1476/1474/1473/1471	1470	452	A_1	$\nu(CN)_s$ (20) + $\nu(CC)_2$ (16) +$\delta(CH)_1$ (15) + $\nu(CC)_5$ (15) + $\delta(NH)_s$ (10)
1362/1360/1358/1357/1356	1365	24	B_2	$\nu(CC)_2$ (33) + $\nu(CC)_6$ (17) + $\delta(CH)_1$ (13)
	1364	158	A_1	$\delta(CH)_2$ (49) + $\delta(NH)_{as}$ (36)
1323/1320	1306	17	B_2	$\nu(NC)_{as}$ (49) + $\nu(CN)_{as}$ (13) + $\delta(ring1)_2$ (12)
1279/1273/1272/1271/1269	1268	30	A_1	$\nu(CN)_s$ (34) + $\nu(CC)_1$ (15) + $\delta(CH)_1$ (13) + $\nu(CC)_5$ (12) + $\nu(CC)_2$ (11)
1244	1245	20	B_2	$\delta(NH)_{as}$ (34) + $\delta(CH)_2$ (34)
1207/1206/1201	1195	8	B_2	$\nu(CN)_{as}$ (28) + $\nu(NC)_{as}$ (21) + $\delta(CH)_3$ (18) + $\delta(NH)_{as}$ (13) + δ(ring2)
1161	1163	5	A_1	$\nu(CC)_6$ (14) + $\delta(CH)_4$ (72)
1141/1140/1138/1137	1142	206	A_1	$\delta(NH)_s$ (43) + ν(C=S) (24) + $\nu(NC)_s$ (23)
1111	1113	1	B_2	$\nu(CC)_4$ (52) + $\delta(CH)_3$ (34) + $\nu(CC)_3$ (10)
1020/1019/1015/1013/1012	1021	15	A_1	$\nu(CC)_6$ (37) + $\nu(CC)_2$ (22) + $\delta(CH)_1$ (18) + $\nu(CC)_1$ (13)
978/974	972	3	A_1	$\delta(ring1)_1$ (46) + $\nu(NC)_s$ (33) + $\nu(CC)_5$ (10)
-	958	-	A_2	$\gamma(CH)_4$ (110) + $\gamma(CH)_1$ (13)
911	912	3	B_1	$\gamma(CH)_3$ (108)
n.o	888	0.09	B_2	$\delta(ring2)_1$ (52) + $\nu(CN)_{as}$ (19) + $\delta(ring1)_2$ (10)
-	837	-	A_2	$\gamma(CH)_1$ (86) + $\gamma(CH)_4$ (13)
823/822	819	0.04	A_1	$\nu(CN)_s$ (20) + $\nu(CC)_1$ (27) + $\nu(CC)_5$ (26)
-	737	-	A_2	$\tau(ring2)_1$ (71) + $\tau(ring1)_1$ (33)
740/739/737/735	735	82	B_1	$\gamma(CH)_2$ (92)
668	653	15	B_1	γ(C=S) (54) + $\tau(ring1)_2$ (51)
621	620	3	B_2	$\nu(CC)_3$ (10) + $\delta(ring1)_2$ (40) + $\delta(ring2)_2$ (27)
614/613/612/609	615	21	A_1	$\delta(ring2)_3$ (48) + ν(C=S) (18) + $\delta(ring2)_2$ (16) + $\delta(ring1)_1$ (11)
-	570	-	A_2	$\tau(ring2)_2$ (49) + $\tau(ring2)_1$ (38) + $\tau(ring1)_1$ (28)
540/539/537/536	522	148	B_1	$\gamma(NH)_{as}$ (102) + γ(C=S) (19)
467	467	4	B_2	δ(C=S) (31) + $\delta(ring2)_2$ (25) + $\delta(ring1)_2$ (17) + $\delta(ring2)_1$ (10)
-	448	-	A_2	$\gamma(NH)_s$ (106)
n.i	421	0	A_1	ν(C=S) (30) + $\delta(ring1)_1$ (19) + $\nu(CN)_s$ (14) + $\delta(ring2)_3$ (14)
n.i	418	0.08	B_1	$\tau(ring2)_3$ (78) + τ Butterfly (24)
n.i	294	0.06	B_1	τ Butterfly (47) + $\tau(ring2)_3$ (30) + $\tau(ring1)_2$ (14) + γ(C=S) (10)
-	236	-	A_2	$\tau(ring2)_2$ (53) + $\tau(ring1)_1$ (45)
n.i	222	2	B_1	δ(C=S) (58) + $\nu(CN)_{as}$ (12) + $\delta(ring2)_2$ (11)
n.i	98	0.0004	B_1	$\tau(ring1)_2$ (59) + τ Butterfly (21) + γ(C=S) (17)

[a] See table 26 (Appendix) for the definition of symmetry coordinates. Abbreviations: s, symmetric; as, anti-symmetric; ν, stretching; δ, in-plane bending; γ, out-of-plane bending; [b] Wavenumbers in cm^{-1}; n.i., not investigated. [c] IR intensities in km mol^{-1}. [d] PED's lower than 10% are not shown.

1-Methyl-2-Mercaptoimidazole

The infrared spectrum of the matrix-isolated compound (15 K) and the calculated spectra of the two tautomeric structures are presented in **figure 22.** The bands of the as-deposited sample match very well the calculated ones for the thione tautomeric species. In this case, the water bands were subtracted from the experimental spectrum in order to make possible the visualization and correct identification of the vibrational assignments in this region.

The non-observation of any evidence of the thiol tautomer in the matrix, as the absence of any band in a position matching its most intense band at near 1445 cm^{-1}, suggests that this tautomer is not present in the gas phase prior to deposition. This also allows to conclude that the energy transferred as heat to the solid to obtain the gaseous compound was not sufficient to cross the energy barrier associated to an intramolecular hydrogen transfer between the nitrogen and sulphur, which would putatively convert the thione form (present in the crystal) to the thiol form.

From the observation of the registered infrared spectrum (see also **table 15**, with the proposed band assignments) it is possible to verify that a widespread site-splitting does also occur for this molecule in the bands having a significant contribution from the δN-H bending modes (both symmetrical and asymmetrical bendings) or νNH stretching mode.

Another relevant feature raises with the observation of a broad feature (which exhibits also extensive site-splitting; 1505, 1500, 1496, 1485, 1482 cm^{-1}) appearing nearly at 1485 cm^{-1}, ascribable mostly to the methyl symmetric bending. The observed broadening might be due to the fact that the methyl group is undergoing a partial free rotation even in the matrix media (i.e., the methyl torsion is characterized by being a large amplitude vibration), which induces a dispersion of the vibrational levels associated with the bending modes (and also with the stretching modes, which unfortunately appear with too low intensity in the matrix spectra to allow a detailed analysis of the band profiles).

The molecule of 1-methyl-2-mercaptoimidazole has 13 atoms which gives rise to 33 normal modes of vibration. Since thione 1-M-2-MI has a C_s symmetry, all of the normal modes are active in the infrared. The internal coordinates used to normal modes description of the 1-M-2-MI thione are shown in **table 27** (see **Appendix**).

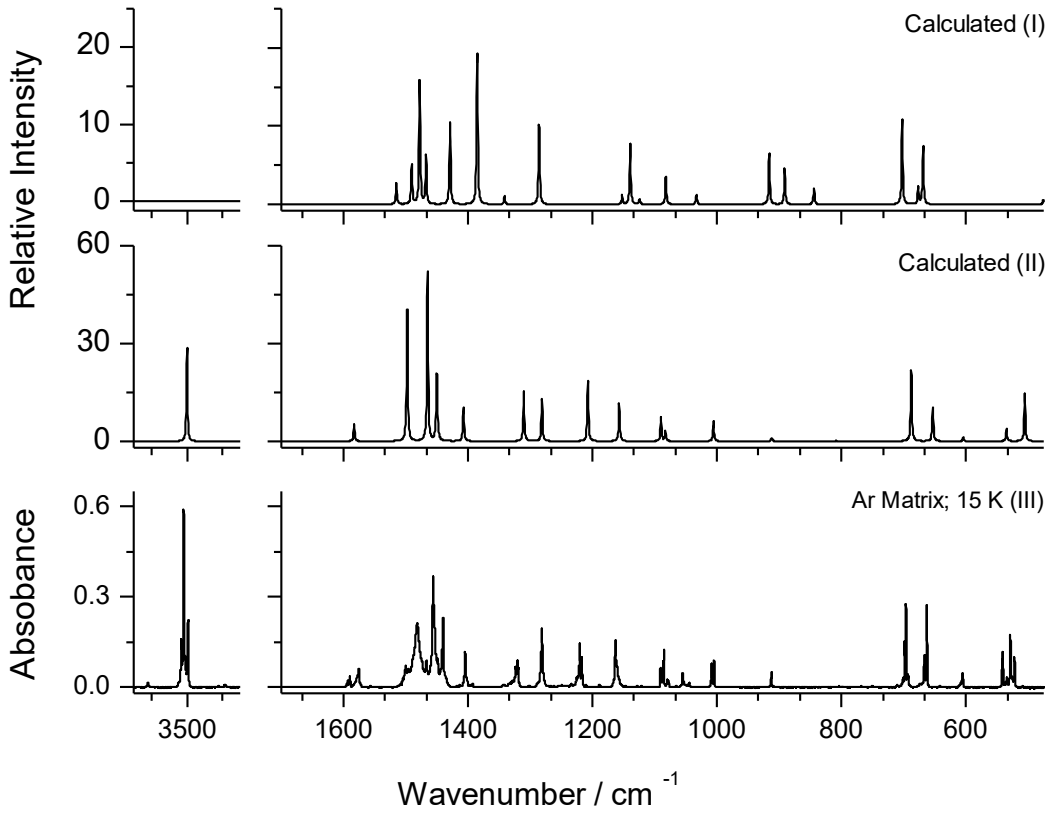

Figure 22. Experimental infrared spectrum of 1-M-2-MI isolated in an argon matrix at 15 K (III) compared with the DFT(B3LYP)/6-311++G(d,p) calculated spectra of thione and thiol tautomers (II and I, respectively). The calculated spectra were simulated by Lorentzian functions. The calculated intensities of the simulated bands correspond to the areas below the Lorentzian functions.

Table 15. Experimental and calculated DFT(B3LYP)/6-311G++(d,p) frequencies of 1-M-2-MI and Potential Energy Distributions (PED).[a]

Experimental (Ar Matrix)	**Calculated**			
$\tilde{\nu}^b$	$\tilde{\nu}^b$	$I_{IR}{}^c$	Sym.	PED[d]
3510/3506/3498	3500	90	A'	$\nu(NH)$ (100)
3170/3165	3140	0.2	A'	$\nu(CH)_1$ (96)
3152/3141	3120	3	A'	$\nu(CH)_2$ (97)
3017	2994	8	A'	$\nu(CH_3)_{as'}$ (99)
2987	2968	10	A"	$\nu(CH_3)_{as"}$ (100)
2949	2907	30	A'	$\nu(CH_3)_s$ (99)
1575	1583	16	A'	$\nu(C=C)$ (63) + $\delta(CH)_2$ (10)
1505/1500/1496/1485/1482	1498	135	A'	$\gamma(CH_3)_{as'}$ (59) + $\delta(CH_3)_{as'}$ (15)
1467/1456/1449	1465	164	A'	$\delta(CH_3)_s$ (27) + $\delta(NH)$ (21) + $\gamma(CH_3)_{as'}$ (12)
1441/1440	1450	63	A'	$\delta(CH_3)_s$ (38) + $\gamma(CH_3)_{as'}$ (13)
	1449	14	A"	$\gamma(CH_3)_{as"}$ (90) + $\delta(CH_3)_{as"}$ (10)
1404/1401	1407	33	A'	$\delta(CH_3)_s$ (32) + $\delta(CH)_1$ (11) + $\delta(CH)_2$ (11) + $\nu(CN)_3$ (10)
1323/1321/1319	1310	48	A'	$\nu(NC)_3$ (28) + $\delta(CH_3)_{as'}$ (15) + $\nu(CN)_2$ (13) + $\delta(NH)$ (12)
1287/1284/1281/1278	1281	44	A'	$\nu(NC)_3$ (26) + $\delta(CH)_1$ (19) + $\delta(CH)_2$ (14)
1222/1220	1207	59	A'	$\nu(NC)_2$ (45) + $\delta(NH)$ (20) + $\delta(CH)_2$ (12)
1163/11161	1157	36	A'	$\nu(C=S)$ (17) + $\delta(ring)_1$ (17)+ $\nu(CN)_3$ (12) + $\delta(CH_3)_{as'}$ (11)
1128/1121	1131	0.2	A"	$\delta(CH_3)_{as"}$ (88) + $\delta(CH_3)_4$ (10)
1091/1086/1085	1090	23	A'	$\nu(CN)_3$ (47) + $\delta(CH)_2$ (22) + $\delta(NH)$ (13)
1080/1078	1083	10	A'	$\delta(CH_3)_3$ (31) + $\delta(CH)_1$ (24) + $\delta(CH)_2$ (16)
1009/1005	1006	19	A'	$\nu(CN)_2$ (27) + $\delta(CH)_1$ (18) + $\gamma(CH_3)_{as'}$ (17)
913	912	3	A'	$\delta(ring)_2$ (62) + $\nu(NC)_3$ (20) + $\delta(ring)_1$ (11)
804/798	809	0.7	A"	$\gamma(CH)_1$ (61) + $\gamma(CH)_2$ (52)
701/698/696/694/692	688	68	A"	$\gamma(CH)_2$ (33) + $\gamma(CH)_1$ (26) + $\tau(ring)_2$ (23) + $\gamma(C=S)$ (19)
	687	5	A'	$\nu(NC)_1$ (43) + $\delta(ring)_2$ (12) + $\delta(ring)_1$ (11)
667/663	653	35	A"	$\gamma(C=S)$ (36) + $\tau(ring)_2$ (24) + $\gamma(CH)_2$ (19) + $\gamma(CH)_1$ (18)
608/606/605	604	4	A"	$\tau(ring)_1$ (101)
542/541	535	13	A'	$\nu(C=S)$ (49) + $\delta(ring)_1$ (29) + $\delta(NC)$ (10)
529/526/522	505	46	A"	$\gamma(NH)$ (92) + $\tau(ring)_1$ (13)
n.o	411	3	A'	$\delta(NC)$ (43) + $\delta(C=S)$ (29)
n.i	239	4	A'	$\delta(C=S)$ (56) + $\delta(NC)$ (35)
n.i	209	3	A"	$\tau(ring)_2$ (35) + $\gamma(C=S)$ (34) + $\gamma(NC)$ (30)
n.i	185	3	A"	$\gamma(NC)$ (64) + $\tau(ring)_2$ (31)
n.i	40	0.2	A"	$\tau(CH_3)$ (99)

[a] See table 27 (Appendix) for the definition of symmetry coordinates. Abbreviations: s, symmetric; as, anti-symmetric; ν, stretching; δ, in-plane bending; γ, out-of-plane bending; τ, torsion.[b] Wavenumbers in cm^{-1}; n.i., not investigated. [c] IR intensities in km mol^{-1}. [d] PED's lower than 10% are not shown.

1-Methyl-2-Mercaptobenzimidazole

The infrared spectrum of the matrix-isolated 1-M-2-MBI (10 K) and the calculated spectra of the two tautomeric structures are present in **figure 23**. As in the other studied cases, and is in agreement with the calculations, the spectrum of the as-deposited matrix corresponds to that of the thione tautomeric form.

It is possible to notice that specific interactions between the molecule and the matrix contribute to the observed broadening (the benzosubstituent has been identified as a cause of site-splitting, while the methyl groups has been show – see above – to exhibit a substantial conformational flexibility with a torsional mode of large amplitude, which is in agreement with the 1.1 kJ mol^{-1} predicted low barrier for methyl torsion).

The molecule of 1-methyl-2-mercaptobenzimidazole has 19 atoms which gives rise to 51 normal modes of vibration. Belonging to the C_s point group, the thione form has all normal modes active in the infrared. **Table 28** (**Appendix**) shows the definition of the internal coordinates used in the performed normal coordinate analysis. The spectral assignments, together with the calculated energy distributions (PED), are shown in **table 16.**

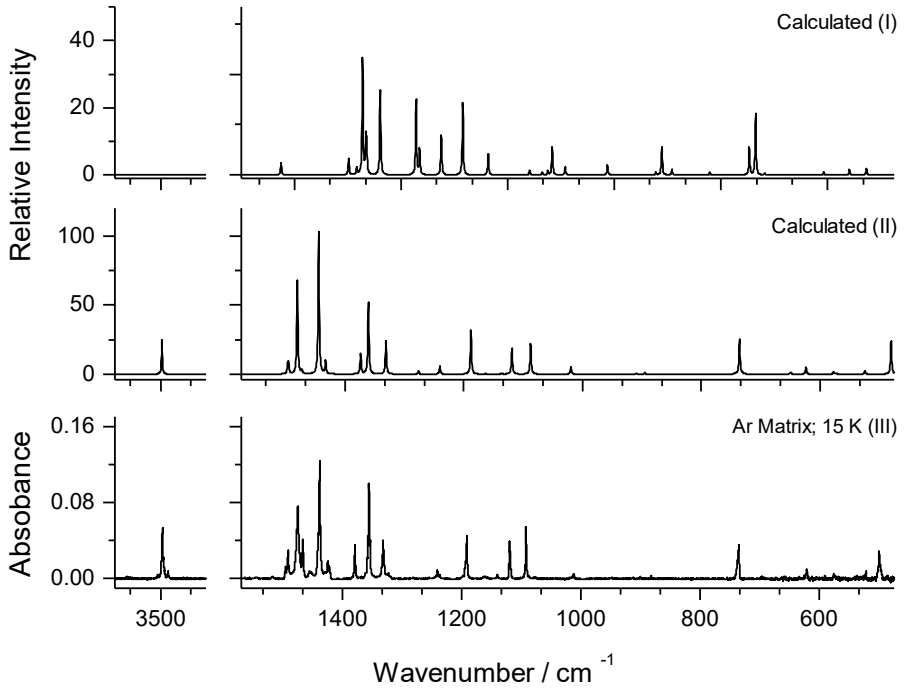

Figure 23. Experimental infrared spectrum of 1-M-2-MBI isolated in an argon matrix at 15 K (III) compared with the DFT(B3LYP)/6-311++G(d,p) calculated spectra of thione and thiol tautomers (II and I, respectively). The calculated spectra were simulated by Lorentzian functions. The relative intensities of the simulated bands correspond to the areas below the Lorentzian functions.

Table 16. Experimental and calculated DFT(B3LYP)/6-311G++(d,p) frequencies of 1-M-2-MBI and Potential Energy Distributions (PED).[a]

Experimental (Ar matrix)	**Calculated**			
$\tilde{\nu}^b$	$\tilde{\nu}^b$	$I_{IR}{}^c$	Sym.	PED[d]
3506/3496/3493/3483	3497	80	A'	$\nu(NH)$ (100)
3081	3053	7	A'	$\nu(CH)_1$ (93)
3073	3046	13	A'	$\nu(CH)_3$ (78)
3063	3037	7	A'	$\nu(CH)_2$ (90)
n.o	3028	0.05	A'	$\nu(CH)_4$ (89)
3020	2995	0.6	A'	$\nu(CH_3)_{as'}$ (95)
2974	2949	19	A"	$\nu(CH_3)_{as"}$ (100)
2936	2892	42	A'	$\nu(CH_3)_s$ (95)
1600 ?	1631	12	A'	$\nu(CC)_2$ (34) + $\nu(CC)_3$ (12)
1589	1620	10	A'	$\nu(CC)_1$ (29) + $\nu(CC)_5$ (18) + $\nu(CC)_4$ (12) + $\nu(CC)_6$ (12)
1496	1497	19	A'	$\gamma(CH_3)_{as'}$ (27) + $\delta(CH_3)_s$ (10)
1492	1496	24	A'	$\delta(CH)_2$ (20) + $\nu(CC)_3$ (14) + $\nu(CC)_4$ (14) + $\delta(CH)_1$ (12)
1475/1472	1480	212	A'	$\gamma(CH_3)_{as'}$ (35) + $\nu(CC)_5$ (10)
1467	1473	8	A"	$\gamma(CH_3)_{as"}$ (92)
1441/1439	1444	324	A'	$\delta(NH)$ (22) + $\delta(CH)_1$ (14) + $\nu(NC)_3$ (11) + $\gamma(CH_3)_{as'}$ (10)
1425/1423	1433	29	A'	$\delta(CH_3)_s$ (75)
1379	1374	48	A'	$\nu(NC)_1$ (19) + $\nu(NC)_2$ (16)
1359/1356/1354	1361	167	A'	$\nu(CC)_2$ (13) + $\nu(CC)_6$ (13) + $\delta(CH_3)_s$ (10)
1335/1332	1331	77	A'	$\delta(CH)_4$ (16) + $\nu(CN)_1$ (12) + $\delta(CH)_1$ (12) + $\delta(CH)_2$ (11)
1281	1277	7	A'	$\nu(CN)_{10}$ (25) + $\nu(NC)_8$ (15) + $\nu(CC)_4$ (12)
1241/1237	1241	18	A'	$\delta(CH)_4$ (18) + $\delta(CH)_3$ (16) + $\delta(CH_3)_{as"}$ (15) + $\nu(NC)_2$ (10)
1194/1192	1188	101	A'	$\nu(NC)_3$ (37) + $\delta(NH)$ (33)
1163	1164	1	A'	$\delta(CH)_2$ (33) + $\delta(CH)_1$ (26) + $\nu(CC)_6$ (13) + $\delta(CH)_4$ (11)
1141	1137	2	A'	$\nu(NC)_1$ (16) + $\delta(ring1)_1$ (13) + $\nu(CC)_5$ (11)
1120/1119	1135	0.5	A"	$\delta(CH_3)_{as"}$ (90)
	1119	59	A'	$\delta(CH_3)_{as'}$ (16) + $\nu(CC)_4$ (15) + $\nu(CC)_3$ (10)
1093	1087	72	A'	$\delta(CH_3)_{as'}$ (30) + $\delta(ring2)_1$ (11) + $\nu(NC)_2$ (11)
1014/1013	1020	17	A'	$\nu(CC)_6$ (38) + $\nu(CC)_4$ (18) + $\nu(CC)_3$ (16) + $\delta(CH)_3$ (11) + $\delta(CH)_4$ (11)
949	957	0.007	A"	$\gamma(CH)_4$ (110) + $\gamma(CH)_1$ (13)
901	909	2	A"	$\gamma(CH)_3$ (109)
882	895	3	A'	$\delta(ring2)_1$ (43) + $\nu(NC)_2$ (10)
n.o	836	0.004	A"	$\gamma(CH)_1$ (85) + $\gamma(CH)_4$ (13)
829	835	0.1	A'	$\nu(CC)_1$ (15) + $\nu(CC)_5$ (14) + $\nu(C=S)$ (12) + $\nu(CN)_2$ (12) + $\nu(CC)_2$ (10)
747	742	3	A"	$\tau(ring2)_1$ (70) + $\tau(ring1)_1$ (31)
737/736	735	81	A"	$\gamma(CH)_2$ (91)
	730	1	A'	$\nu(NC)_1$ (25) + $\nu(NC)_2$ (11) + $\delta(ring1)_1$ (10) + $\delta(ring2)_2$ (19)
662	650	4	A"	$\gamma(C=S)$ (60) + $\tau(ring1)_2$ (42)
626/624/622/620	624	17	A'	$\delta(ring2)_3$ (47) + $\nu(C=S)$ (15) + $\delta(ring1)_2$ (11)
576	577	7	A'	$\gamma(C=S)$ (10) + $\delta(ring1)_2$ (15) + $\delta(ring2)_2$ (36)
574	573	2	A"	$\tau(ring2)_2$ (48) + $\tau(ring2)_1$ (38) + $\tau(ring1)_1$ (28)
522	524	8	A'	$\delta(ring1)_2$ (28) + $\delta(ring2)_3$ (15) + $\delta(C=S)$ (12) + $\delta(NC)$ (11)
500	480	78	A"	$\gamma(NH)$ (97) + $\gamma(C=S)$ (10)
n.i	424	0.1	A"	$\tau(ring2)_3$ (70) + τ Butterfly (26)
n.i	421	11	A'	$\nu(C=S)$ (31) + $\delta(ring1)_1$ (19) + $\delta(ring2)_3$ (12)

n.i	305	0.06	A"	$\tau(ring2)_3$ (35) + τ Butterfly (34) + γ(C=S) (11)
n.i	266	2	A'	δ(NC) (62) + δ(C=S) (19)
n.i	258	0.8	A"	$\tau(ring2)_2$ (41) + $\tau(ring1)_1$ (26) + γ(NC) (23)
n.i	227	2	A'	δ(C=S) (48) + $\delta(ring2)_2$ (14)
n.i	132	3	A"	γ(NC) (71) + $\tau(ring1)_1$ (15) + $\tau(ring2)_2$ (12)
n.i	100	0.4	A"	$\tau(ring1)_2$ (56) + τ Butterfly (23) + γ(C=S) (17)
n.i	88	0.01	A"	$\tau(CH_3)$ (93)

[a] See table 28 (Appendix) for the definition of symmetry coordinates. Abbreviations: s, symmetric; as, anti-symmetric; ν, stretching; δ, in-plane bending; γ, out-of-plane bending; τ, torsion.[b] Wavenumbers in cm^{-1}; n.i., not investigated. [c] IR intensities in km mol^{-1}. [d] PED's lower than 10% are not shown.

CHAPTER IV

Chapter IV. Photochemistry of 2-Mercaptoimidazole, 2-Mercaptobenzimidazole and their 1-Methyl Substituted Derivatives

4.1 Introduction

The photo-induced reactions of heterocyclic compounds have been widely studied due to their relevance in many domains. Light-induced proton transfer reactions, in particular, play important roles in chemistry, materials sciences and biochemistry, justifying the large effort dedicated to this subject over the years by the scientific community. Because the advantages of the matrix isolation technique in establishing details of the mechanisms associated with such type of chemical processes, this has been one of the elected techniques since its development, but in particular after the development of affordable tunable UV-lasers.

Phototautomerization in matrix-isolated species has been one of the central subjects of investigation in the LMCB. Phototautomerism in nucleic acid bases, phenol and thiophenol derivatives, among other families of compounds, have been investigated in detail in the Laboratory.[30,32,33,35,36] However, the phototautomerism involving directly sulphur and nitrogen atoms in heterocyclic rings has not yet received much attention, and mechanistic aspects of the photo-induced H-transfer processes in this type of molecules still remain unclear. This fact has motivated the present investigation, which intends to give a contribution to further the understanding of this type of processes.

In this chapter, the results of our investigation on the photo-induced tautomerism of matrix-isolated 2-mercaptoimidazole, 2-mercaptobenzimidazole and their 1-methyl derivatives are reported. The matrix-isolated monomers of the studied compounds were subjected to *in situ* irradiations with light provided by a tunable narrowband UV source, and the photoreactions were probed by infrared spectroscopy, supported by results of quantum chemical calculations of the IR spectra of the relevant species. The results obtained for the four studied molecules are compared, and correlations between their structures and the experimental observations are proposed. Besides phototautomerism other observed photoprocesses are also described in this chapter.

4.2 Phototautomerism

As it was described in Chapter 2, only the thione tautomeric form of the molecules under study were observed in the as-deposited matrices of the compounds. As shown below, upon excitation of these species at proper wavelengths, we were able to convert them to the corresponding thiol tautomers, which have never been observed before. The first step in the design of the photochemical experiments was the selection of the excitation wavelengths to apply to the matrix-isolated compounds. Two strategies were used: (1) recording and analysis of the UV absorbance spectra of the compounds in ethanol solution; (2) searching for the most efficient excitation wavelengths by wavelength scan directly performed on the matrix-isolated compounds. The irradiations were performed with the narrowband UV light provided from the laser/MOPO system described in Chapter 2. The photo-induced reverse process (thiol→thione) was also successfully achieved for the benzene substituted compounds, upon subsequent irradiations of the initially produced thiol tautomer, using different wavelength.

2-Mercaptoimidazole

Matrix-isolated 2-MI monomers were irradiated using wavelengths in the range 300-260 nm, using the direct scan approach. The irradiations with $\lambda > 295$ nm did not lead to any observable change in the IR spectra of the matrix-isolated 2-MI. The first changes were detected after the 295 nm irradiation, while the maximum consumption of the initially present in the matrix 2-MI thione tautomeric form took place when irradiation was performed at $\lambda = 290$ nm (**figure 24**).

Figure 25 shows the results obtained after 30 min of irradiation at 290 nm. From the IR intensities, it could be estimated that the amount of thione was reduced comparatively to the initial amount. On the other hand, a set of bands appearing after irradiation could be assigned to the 2-MI thiol tautomer (see **figure 25**). Besides, other new bands due to additional photoproducts could also be observed to emerge in the infrared spectrum of the photolysed matrix.

The excitation wavelength used that found to be more effective for thione 2-MI consumption is in agreement with the absorption in the UV spectrum of 2-MI in ethanol solution. A detailed analysis of this spectrum, including its comparison with the theoretically obtained UV spectrum using time-dependent DFT (TD-DFT) calculations for both tautomers, led to the conclusion that in ethanol solution, while both tautomers can be expected to coexist, the absorption bands of the two tautomers (thione and thiol) are extensively overlapped, through the thiol form shall absorb mostly in the higher-energy wing of

the observed band. These facts, and the relative low efficiency of the observed thione→thiol process, made not possible to observe the reverse phototautomerisation for this molecule.

On the other hand, phototransformation of both forms into other species (see in section 4.3) was also observed.

The comparison of the experimental infrared spectrum of the main photoproduct resulting from the 290 nm irradiation with the theoretical one predicted for the 2-MI thiol tautomer (see **figure 25**) allowed to doubtlessly conclude that this tautomer corresponds to the observed photoproduct. The observation of the *ν*SH stretching characteristic band at 2620 cm^{-1}, in particular, is especially conclusive. **Tables 29** (**Appendix**) and **17 p**resent the chosen coordinates for the normal coordinate analysis carried on for 2-MI thiol tautomer and the assignments proposed here for the IR spectrum of this species, respectively. This tautomer belongs to C_s symmetry point group. The assignments take into account the calculated data, which is also provided in **Table 17.**

It shall be stressed here that it is also clear from the results (specifically from the observed relative IR intensities) that the consumption of the thione form does not promote a proportional formation of the thiol tautomer (30 min of irradiation at 290 nm reduces the amount of the thione form in ~80%, while the amount of thiol form produced is only ~15%; these results were obtained by taking into account the ratio of the most intense experimental bands in the spectra of the reactant and photoproduct and the corresponding ratio of the calculated IR bands). This shows that additional products are being formed, in agreement with observation of several new bands in the spectra of the photolysed matrix that cannot be explained by the sole formation of the thiol 2-MI form. This will be discussed in details in Section 4.3.

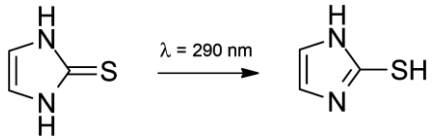

Figure 24. Photo-induced conversion of thione into thiol form of 2-MI.

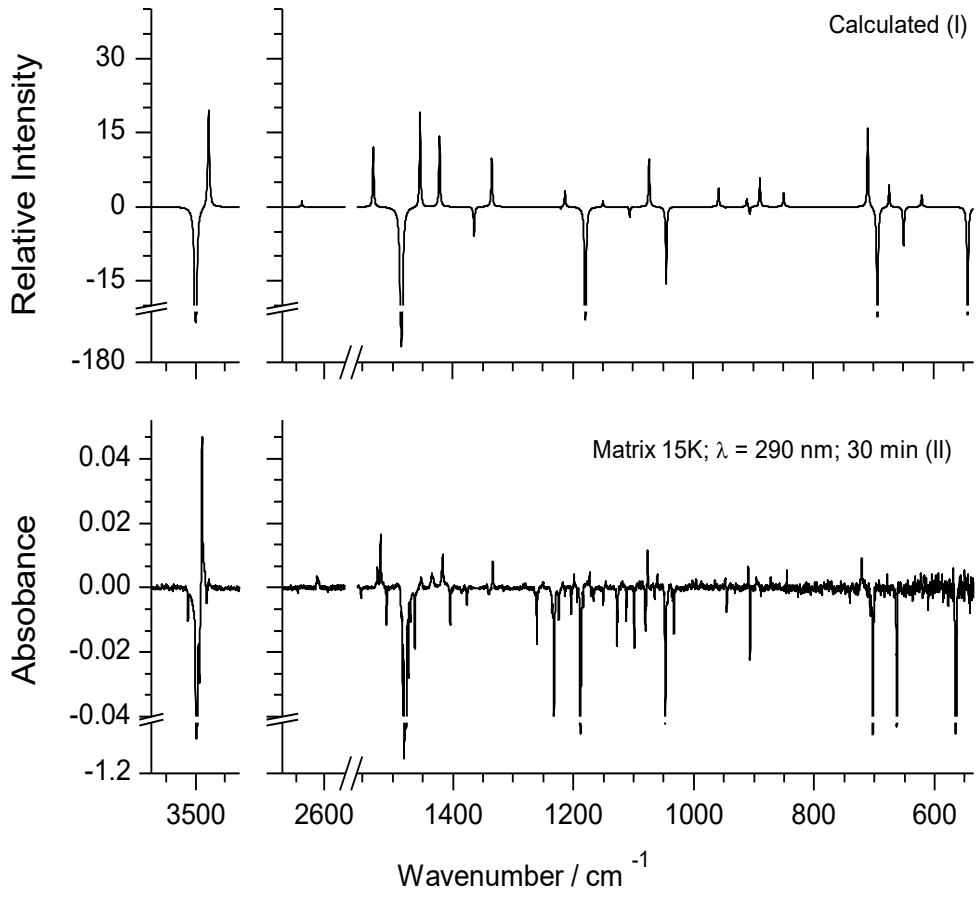

Figure 25. Infrared difference spectrum: (I) theoretical spectrum of thiol "*minus*" theoretical spectrum of thione 2-MI; (II) experimental IR spectrum after λ=290 nm (30 min) irradiation "*minus*" spectrum of the as-deposited matrix.

Table 17. Experimental and calculated DFT(B3LYP)/6-311G++(d,p) frequencies of 2-MI thiol and Potential Energy Distributions (PED).[a]

Experimental	**Calculated**			
$\tilde{\nu}^b$	$\tilde{\nu}^b$	$I_{IR}{}^c$	Sym.	PED[d]
3493	3485	63	A'	ν(NH) (100)
3158 ?	3125	0.6	A'	$\nu(CH)_1$ (87) + $\nu(CH)_2$ (12)
3140	3096	4	A'	$\nu(CH)_2$ (88) + $\nu(CH)_1$ (12)
2618	2653	3	A'	ν(SH) (100)
1526/1520	1532	39	A'	ν(C=C) (42) + δ(NH) (19) + $\nu(NC)_2$ (16) + $\delta(CH)_2$ (10)
1453/1438	1454	60	A'	$\nu(NC)_2$ (33) + ν(C=C) (22) + $\delta(CH)_1$ (14)
1419/1417	1422	46	A'	$\nu(NC)_1$ (35) + δ(NH) (23) + $\nu(NC)_2$ (12)
1334	1335	32	A'	$\nu(NC)_2$ (24) + $\delta(CH)_2$ (21) + $\nu(CN)_1$ (20) + $\nu(CN)_2$ (13) + $\delta(CH)_1$ (13)
1217	1213	10	A'	$\nu(NC)_1$ (34) + δ(NH) (21) + $\delta(CH)_2$ (21)
1146	1150	4	A'	$\nu(CN)_2$ (69) + $\nu(CN)_1$ (14) + $\delta(CH)_2$ (12)
n.o	1107	0.2	A'	$\delta(CH)_1$ (35) + ν(C=C) (30) + $\delta(CH)_2$ (15)
1060	1073	31	A'	$\nu(CN)_1$ (46) + δ(NH) (23) + $\delta(CH)_1$ (14)
965	958	12	A'	$\delta(ring)_1$ (47) + $\delta(ring)_2$ (15)
910	911	5	A'	$\delta(ring)_2$ (77)
896	889	18	A'	δ(SH) (84) + $\nu(NC)_1$ (11)
846	849	9	A"	$\gamma(CH)_2$ (96) + $\gamma(CH)_1$ (15)
722	709	51	A"	$\gamma(CH)_1$ (73) + $\tau(ring)_2$ (17)
679	674	14	A"	$\tau(ring)_2$ (65) + $\gamma(CH)_1$ (19) + γ(CS) (10)
623?	620	7	A"	$\tau(ring)_1$ (107)
475	470	0.6	A'	ν(CS) (73) + $\delta(ring)_1$ (19)
504/495	461	68	A"	γ(NH) (99)
n.i	282	9	A'	δ(CS) (92)
n.i	219	4	A"	γ(CS) (78) + $\tau(ring)_2$ (23)
n.i	64	36	A"	τ(SH) (98)

[a] See table 29 (Appendix)for the definition of symmetry coordinates. Abbreviations: s, symmetric; as, anti-symmetric; ν, stretching; δ, in-plane bending; γ, out-of-plane bending; τ, torsion.[b] Wavenumbers in cm^{-1}; n.i., not investigated. [c] IR intensities in km mol^{-1}. [d] PED's lower than 10% not shown.

2-Mercaptobenzimidazole

2-MBI was isolated in an argon matrix and irradiated with UV light. The initially used UV wavelength was 307 nm, which was selected taking into account the absorption spectrum of the compound in ethanol (**figure 27**) and the TD-DFT calculated UV spectrum, as well as literature data for similar thiones and thiols.[18,29] The analysis of these data led to the conclusion that the benzosubstituted 2-mercaptoimidazole thione should absorb at longer wavelengths than 2-MI.

Upon irradiation, the bands of 2-MBI thione tautomer decreased and new bands fitting well the predicted spectrum of the thiol tautomer emerged in the spectrum (see **figure 28** and **table 18,** with proposed assignments for this tautomer). The matrix was subjected to a total irradiation time of 240 minutes (the amount of the thione form was reduced in ~50%). A considerable amount of the thione tautomer (~30 %) could be converted into the thiol form. The average ratio of conversion was greater than that achieved for 2-MI. Nevertheless, also for 2-MBI the thione form was not fully consumed, and no photostationary equilibrium could be achieved even after the 240 min spent irradiating the sample (this could be easily noticed by plotting the decrease of intensity of the IR bands of either the thione or the thiol forms as a function of the time, whose curves do not exhibit the expected plateau of a photostationary state). We can then conclude that, in spite of its greater efficiency compared with the reaction in 2-MI, the phototautomerization efficiency of the thione→thiol conversion is not total.

The reversibility of the photoreaction was, in this case, successfully proved by the performed subsequent irradiation at λ = 246 nm (**figure 26**). This irradiation wavelength was chosen taking into account the UV absorption spectrum of 2-MBI in ethanol (see **figure 27**). The experimental IR data showing the results of the irradiation at 246 nm following the initial irradiation at 307 nm are shown in **figure 28**.

The experimental results clearly demonstrate that the two tautomers can be photochemically interconverted, with appropriate selection of the excitation wavelengths. Interestingly, the thiol→thione conversion is, contrary to the thione→thiol, very efficient, since all the thiol tautomer formed upon irradiation of the initially deposited thione form at 307 nm was consumed almost totally upon irradiation at 246 nm in 7 minutes. The reasons for the greater efficiency and rate of the reaction in the thiol→thione direction observed for 2-MBI are discussed in the next section.

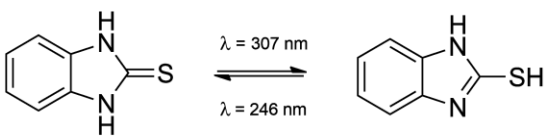

Figure 26. Photo-induced interconversion of thione and thiol forms of 2-MBI.

Another interesting observation in the spectrum obtained after the irradiation at 307 nm was the presence of two very small bands at 760 cm^{-1} and 1191 cm^{-1}, which may belong to the correspondent thyil radical. This specie is proposed as relevant intermediate in the observed phototautomerization processes, as described in detail in the next section. In any case, the proposed radical intermediate could not be established with certainty, based on the analysis of the spectral data under discussion, though the referred low intensity IR bands nearly fit the most intense bands predicted for radical. Furthermore, the detection of similar radicals in matrices by infrared spectroscopy has been proposed by other authors[35-37] and possible mechanisms involving these type of intermediary species in hydrogen-atom-transfer processes have been reported.[25;35-37] At the end of this section, after describing all the experiments involving phototautomerization (for the whole set of molecules studied), some mechanistic aspects will be briefly discussed.

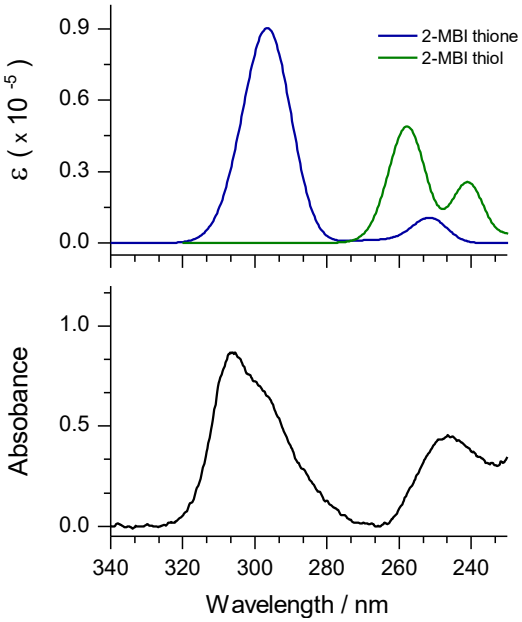

Figure 27. UV experimental absorption spectrum of 2-MBI in ethanol and TD-DFT calculated spectrum of thione and thiol 2-mercaptobenzimidazole (2-MBI).

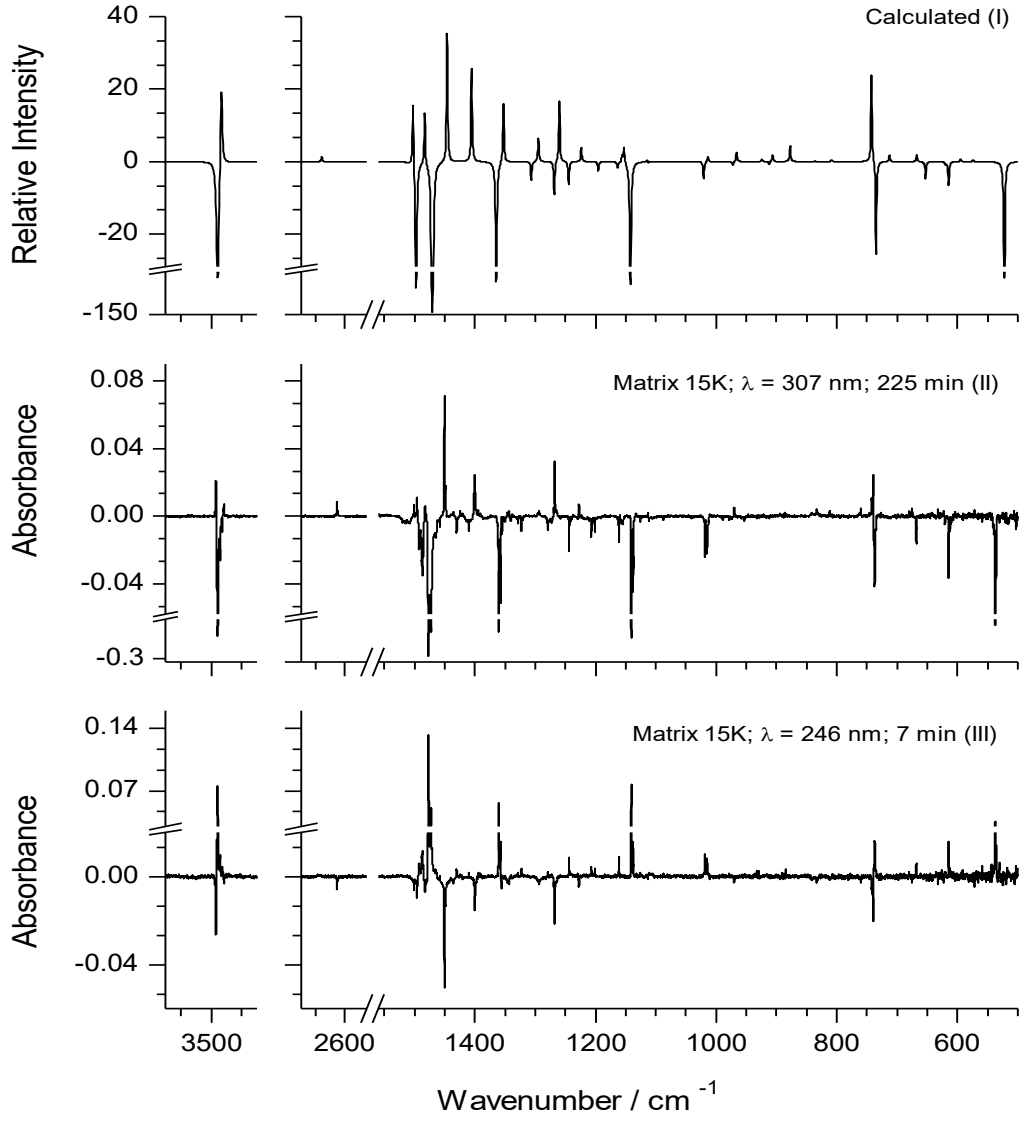

Figure 28. Infrared difference spectrum: (I) theoretical spectrum of thiol "*minus*" theoretical spectrum of thione 2-MBI; (II) experimental IR spectrum after λ= 307 nm (225 min) irradiation "*minus*" spectrum of the as-deposited matrix; (III) experimental IR spectrum after λ= 246 nm (7 min) irradiation "*minus*" spectrum after λ= 307 nm (246 min) irradiation.

Table 18. Experimental and calculated DFT(B3LYP)/6-311G++(d,p) frequencies of 2-MBI thiol and Potential Energy Distributions (PED).[a]

Experimental	**Calculated**			
$\tilde{\nu}^b$	$\tilde{\nu}^b$	$I_{IR}{}^c$	Sym.	PED[d]
3495/3486	3489	68	A'	$\nu(NH)$ (100)
3079?	3050	10	A'	$\nu(CH)_1$ (97)
3072	3042	17	A'	$\nu(CH)_2$ (47) + $\nu(CH)_4$ (35) + $\nu(CH)_1$ (10)
n.o	3031	10	A'	$\nu(CH)_3$ (72) + $\nu(CH)_4$ (24)
n.o	3022	0.05	A'	$\nu(CH)_2$ (53) + $\nu(CH)_4$ (34) + $\nu(CH)_3$ (22)
2620/2619/2617/2616	2653	4	A'	$\nu(SH)$ (100)
1630/1624	1633	10	A'	$\nu(CC)_1$ (28) + $\nu(CC)_2$ (15) + $\nu(CC)_4$ (12)
1596	1599	3	A'	$\nu(CC)_2$ (19) + $\nu(CC)_6$ (17) + $\nu(CC)_3$ (10) + $\nu(CC)_5$ (10)
1500/1496	1502	58	A'	$\delta(CH)_3$ (16) + $\delta(NH)$ (15) + $\nu(NC)_1$ (15) + $\nu(CC)_3$ (12)
1483	1483	46	A'	$\nu(NC)_1$ (36) + $\nu(CC)_1$ (13) + $\nu(CC)_4$ (10)
1450/1449	1446	114	A'	$\delta(CH)_1$ (36) + $\nu(NC)_1$ (19) + $\nu(CC)_5$ (15)
1401	1405	85	A'	$\delta(NH)$ (28) + $\nu(NC)_2$ (18) + $\delta(CH)_2$ (16)
1345/1344	1352	51	A'	$\nu(CC)_2$ (14) + $\nu(CC)_6$ (13) + $\nu(NC)_2$ (11)
1296/1293	1295	21	A'	$\delta(CH)_2$ (53) + $\nu(NC)_2$ (10) + $\nu(CN)_4$ (10) + $\delta(ring2)_1$ (10)
1269/1268	1260	53	A'	$\nu(CN)_3$ (23) + $\nu(CN)_4$ (18) + $\nu(CC)_5$ (13) + $\nu(CC)_4$ (12) + $\nu(CC)_3$ (10) +$\delta(CH)_1$ (10)
1227	1223	12	A'	$\nu(CN)_4$ (23) + $\delta(CH)_3$ (19) + $\nu(CC)_1$ (13) + $\delta(CH)_2$ (11)
n.o	1156	5	A'	$\delta(CH)_4$ (40) + $\delta(NH)$ (13) + $\nu(NC)_2$ (11)
n.o	1153	13	A'	$\delta(CH)_4$ (30) + $\delta(NH)$ (25) + $\nu(NC)_2$ (14)
1113	1114	2	A'	$\nu(CC)_3$ (26) + $\nu(CC)_4$ (24) + $\delta(CH)_3$ (36)
1012	1014	4	A'	$\nu(CC)_6$ (40) + $\delta(CH)_1$ (19) + $\nu(CC)_4$ (16) + $\nu(CC)_3$ (14)
971	966	8	A'	$\delta(ring1)_1$ (54) + $\nu(CC)_5$ (12) + $\nu(NC)_2$ (10)
n.o	963	0.03	A"	$\gamma(CH)_4$ (110)
n.o	924	2	A"	$\gamma(CH)_3$ (101)
893/886	906	5	A'	$\delta(SH)$ (45) + $\delta(ring2)_1$ (26)
842/834	877	14	A'	$\delta(SH)$ (41) + $\delta(ring2)_1$ (26) + $\delta(ring1)_2$ (10)
n.o	836	0.5	A"	$\gamma(CH)_1$ (87) + $\gamma(CH)_4$ (10)
812	808	2	A'	$\nu(CC)_5$ (24) + $\nu(CC)_2$ (16) + $\nu(CC)_1$ (14) + $\nu(CN)_3$ (12)
742/741/740	743	76	A"	$\gamma(CH)_2$ (78)
727	713	5	A"	$\tau(ring1)_1$ (32) + $\tau(ring2)_1$ (62) + $\gamma(CH)_2$ (11)
669/675	668	5	A"	$\tau(ring1)_2$ (71) + $\gamma(CS)$ (23)
623	621	0.3	A'	$\delta(ring1)_2$ (43) + $\delta(ring2)_2$ (25)
604	595	2	A'	$\delta(ring2)_3$ (54) + $\nu(CS)$ (18) + $\delta(ring2)_2$ (14)
572	575	2	A"	$\tau(ring2)_2$ (45) + $\tau(ring2)_1$ (37) + $\tau(ring1)_1$ (31)
n.o	461	10	A'	$\delta(CS)$ (22) + $\delta(ring1)_2$ (15) + $\delta(ring2)_1$ (11) + $\delta(ring2)_2$ (34)
n.o	428	12	A"	$\tau(ring2)_3$ (79) + τ Butterfly (19)
n.i	390	3	A'	$\nu(CS)$ (50) + $\delta(ring1)_1$ (16) + $\delta(ring2)_3$ (11)
n.i	363	54	A"	$\gamma(NH)$ (97)
n.i	299	0.08	A"	τ Butterfly (36) + $\gamma(CS)$ (31) + $\tau(ring2)_3$ (26)
n.i	245	3	A"	$\tau(ring1)_1$ (37) + $\tau(ring2)_2$ (57)
n.i	202	2	A'	$\delta(CS)$ (69)
n.i	147	43	A"	$\tau(SH)$ (92)
n.i	108	4	A"	$\tau(ring1)_2$ (33) + τ Butterfly (32) + $\gamma(CS)$ (29)

[a] See table 30 (Appendix) for the definition of symmetry coordinates. Abbreviations: s, symmetric; as, anti-symmetric; ν, stretching; δ, in-plane bending; γ, out-of-plane bending; τ, torsion.[b] Wavenumbers in cm^{-1}; n.i., not investigated. [c] IR intensities in km mol^{-1}. [d] PED's lower than 10% not shown.

1-Methyl-2-Mercaptoimidazole

The thione tautomeric form of 1-M-2-MI, isolated in the argon matrix, was irradiated at its maximum UV absorption wavelength in ethanol solution ($\lambda = 261$ nm; **figure 29** and **figure 31**). This value was selected by taking into account the previously described experiments where it was shown that the maximum absorbance in the UV spectra in ethanol solution was an appropriate choice for excitation wavelength in order to induce phototautomerization in these molecules. For 1-M-2MI, as for 2-MI, the interpretation of both experimental and calculated UV absorbance spectra led to the conclusion that the absorption bands due to the two tautomeric forms are extensively overlapped.

The results of the phototautomerization experiments on 1-M-2MI (data obtained after 80 min of irradiation) are presented in **figure 30.** After the first irradiation at $\lambda = 261$ nm, the absorptions due to the initially deposited tautomer started to decrease and other bands appear in the infrared spectrum. The thiol calculated spectrum clearly reproduces most of the new emerging bands (see also **table 19**, with the proposed band assignments). An amount of thione tautomer (~20%) was consumed and (~10%) was converted into thiol tautomer.

Subsequent irradiations were performed with UV light of higher energy, up to $\lambda = 230$ nm (the shortest wavelength available in the used experimental set up), in order to try to observe the reverse (thiol→thione) photoprocess. However, very unfortunately, no evidence of occurrence of this reaction could be seen, since both the remaining thione reactant and the previously produced thiol tautomer (obtained by the irradiation at $\lambda = 261$ nm) start to be lost, while formation of other photoproducts was noticed (see in the next section 4.4). The new bands emerge in the same region of the spectrum of the new photoproducts of 2-MI, which indicates that the photofragmentation nature of 1-M-2-MI follow similar pathways to those observed for 2-MI. However, a detailed study of these photofragmentation reactions is still being done.

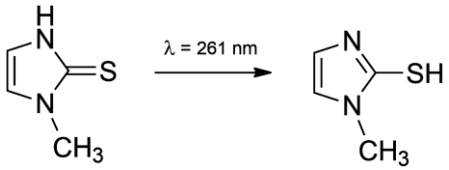

Figure 29. Photo-induced conversion of thione into thiol form of 1-M-2-MI.

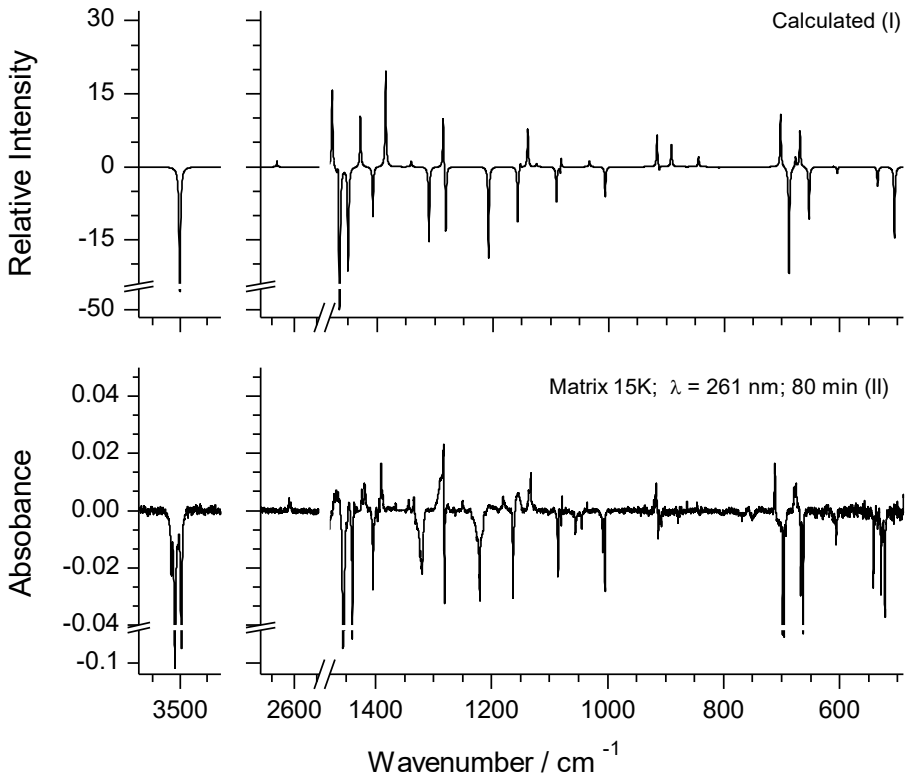

Figure 30. Infrared difference spectrum: (I) theoretical spectrum of thiol "*minus*" theoretical spectrum of thione 1-M-2-MI; (II) experimental IR spectrum after λ=261 nm (80 min) irradiation "*minus*" experimental spectrum of the as-deposited matrix.

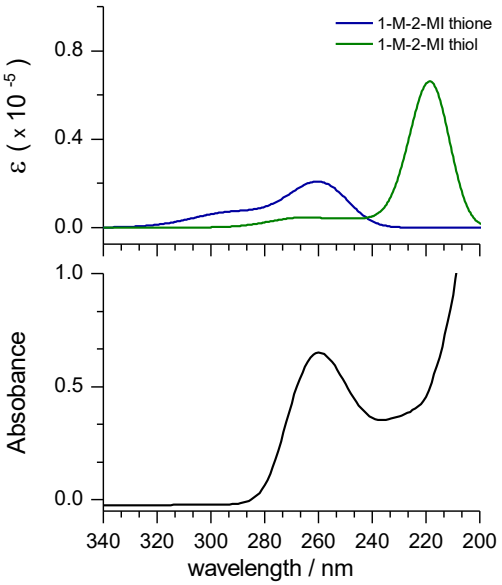

Figure 31. UV experimental absorption spectrum of 1-M-MI in ethanol and TD-DFT calculated spectrum of thione and thiol 1-methyl-2-mercaptoimidazole.

Table 19. Experimental infrared spectrum of the photoproduct 1-M-2-MI thiol compared with the DFT (B3LYP)/6-311G++(d,p) calculated infrared spectrum, and Potential Energy Distributions (PED).[a]

Experimental (Ar matrix)	**Calculated**			
$\tilde{\nu}^b$	$\tilde{\nu}^b$	$I_{IR}{}^c$	Sym.	PED[d]
-	3117	1	A	$\nu(CH)_1$ (81) + $\nu(CH)_2$ (18)
-	3093	4	A	$\nu(CH)_2$ (82) + $\nu(CH)_1$ (18)
-	2990	8	A	$\nu(CH_3)_{as'}$ (94)
-	2956	12	A	$\nu(CH_3)_{as''}$ (95)
-	2897	33	A	$\nu(CH_3)_s$ (93)
2616/2610	2652	3	A	ν(SH) (100)
1507	1515	9	A	ν(C=C) (51) + $\delta(CH)_2$ (12)
n.o	1491	16	A	$\gamma(CH_3)_{as'}$ (64) + $\delta(CH_3)_{as'}$ (10)
1468	1478	51	A	$\nu(NC)_2$ (25) + $\nu(NC)_3$ (12) + $\delta(CH_3)_s$ (20)
1456	1468	20	A	$\gamma(CH_3)_{as''}$ (82)
1424	1429	33	A	$\nu(NC)_2$ (15) + $\delta(CH_3)_s$ (66)
1360	1385	63	A	$\nu(NC)_2$ (16) + $\nu(NC)_3$ (32)
1343/1334	1341	4	A	$\nu(NC)_2$ (23) + $\nu(CN)_2$ (33)
1284/1283	1286	33	A	$\nu(NC)_1$ (20) + $\nu(CN)_1$ (15) + $\delta(CH)_1$ (28) + $\delta(CH)_2$ (15)
n.o	1152	4	A	$\nu(CN)_1$ (61) + $\delta(CH)_1$ (21)
1136/1134/1132	1139	24	A	$\delta(ring)_1$ (20) + $\delta(CH_3)_3$ (17) + $\delta(CH)_2$ (10)
1126	1124	2	A	$\delta(CH_3)_{as''}$ (78)
1078	1082	12	A	$\delta(CH)_2$ (46) + ν(C=C) (16) + $\delta(CH)_1$ (14)
1035	1033	4	A	$\delta(CH_3)_{as'}$ (35) + $\nu(CN)_2$ (31) + $\delta(ring)_2$ (15)
920/918/917	916	21	A	$\delta(ring)_2$ (42) + $\delta(ring)_1$ (19) + δ(SH) (18)
863	891	15	A	δ(SH) (67) + $\delta(ring)_2$ (18)
846	844	7	A	$\gamma(CH)_2$ (97) + $\gamma(CH)_1$ (14)
712	702	34	A	$\gamma(CH)_1$ (77) + $\tau(ring)_2$ (13)
678	677	7	A	$\nu(NC)_1$ (41) + $\delta(ring)_1$ (13) + $\delta(ring)_2$ (11) + $\nu(NC)_3$ (10)
675	669	24	A	$\tau(ring)_2$ (59) + $\gamma(CH)_1$ (13) + $\tau(ring)_1$ (11) + + γ(CS) (10)
620	611	0.2	A	$\tau(ring)_1$ (101)
n.o	476	2	A	ν(CS) (64) + $\delta(ring)_1$ (18) + δ(NC) (11)
n.i	391	2	A	δ(NC) (48) + δ(CS) (28)
n.i	229	1	A	γ(CS) (54) + γ(NC) (28) + $\tau(ring)_2$ (11)
n.i	212	4	A	δ(CS) (58) + δ(NC) (27)
n.i	188	6	A	γ(NC) (40) + τ(SH) (24) + γ(CS) (22)
n.i	124	17	A	τ(SH) (64) + γ(NC) (31)
n.i	62	2	A	$\tau(CH_3)$ (90)

[a] See table 31 (Appendix) for the definition of symmetry coordinates. Abbreviations: s, symmetric; as, anti-symmetric; ν, stretching; δ, in-plane bending; γ, out-of-plane bending; τ, torsion.[b] Wavenumbers in cm^{-1}; n.i., not investigated. [c] IR intensities in km mol^{-1}. [d] PED's lower than 10% not shown.

1-Methyl-2-Mercaptobenzimidazole

The matrix isolated 1-M-2-MBI thione was irradiated at its maximum absorption (λ = 307 nm as in the case of 2-MBI; see **figure 27**). As in the other experiments performed, after irradiation, the bands of 2-MBI thione tautomer decreased and bands due to the thiol form emerged in the infrared spectrum (see **figure 33** and **table 20,** with proposed assignments for this tautomer).

In this case, the matrix was subjected to excitation at λ = 307 nm wavelength for 51 minutes, with the almost total consumption of the thione tautomer (~65%) and formation of the thiol form (~25%).

As for 1-M-2-MBI, the photoreversibility of the phototautomerization was proved by the subsequent irradiation λ = 246 nm (the same wavelength used to promote 2-MBI photo reverse reaction; see **figure 32**) led to the total consumption of the thiol tautomeric form in 8 minutes.

Besides phototautomerization reaction, the formation of other photoproducts was observed (see the next section 4.4) which were not identified yet.

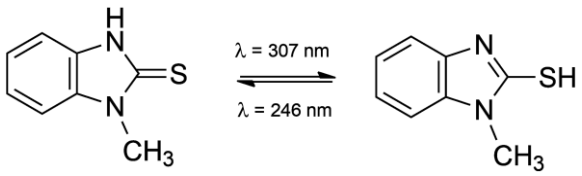

Figure 32. Photo-induced interconversion of thione and thiol forms of 1-M-2-MBI.

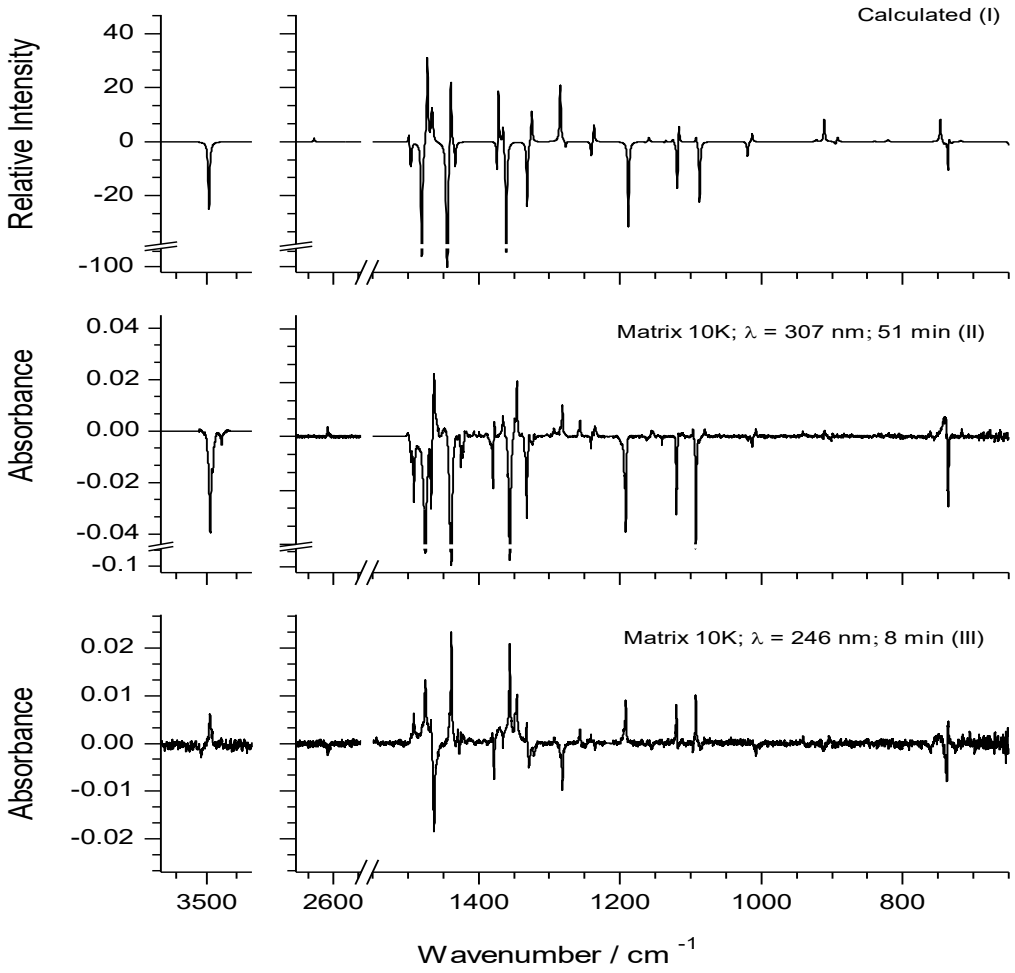

Figure 33. Infrared difference spectrum: (I) theoretical spectrum of thiol "*minus*" theoretical spectrum of thione 1-M-2-MBI; (II) experimental IR spectrum after λ= 307 nm (51 min) irradiation "*minus*" spectrum of the as-deposited matrix; (III) experimental IR spectrum after λ= 246 nm (8 min) irradiation "*minus*" spectrum after λ= 307 nm (51 min) irradiation.

Table 20. Experimental infrared spectrum of the photoproduct 1-M-2-MBI thiol compared with the DFT (B3LYP)/6-311G++(d,p) calculated infrared spectrum, and Potential Energy Distributions (PED).[a]

Experimental (Ar matrix)	**Calculated**			
$\tilde{\nu}^b$	$\tilde{\nu}^b$	$I_{IR}{}^c$	Sym.	PED[d]
n.o	3049	11	A	$\nu(CH)_1$ (79) + $\nu(CH)_4$ (15)
-	3041	18	A	$\nu(CH)_4$ (59) + $\nu(CH)_1$ (20) + $\nu(CH)_3$ (13)
-	3031	10	A	$\nu(CH)_3$ (84) + $\nu(CH)_4$ (15)
-	3021	0.2	A	$\nu(CH)_2$ (87) + $\nu(CH)_4$ (11)
-	2986	6	A	$\nu(CH_3)_{as'}$ (94)
-	2951	15	A	$\nu(CH_3)_{as''}$ (94)
-	2892	42	A	$\nu(CH_3)_s$ (91)
2615	2651	4	A	ν(SH) (100)

n.o	1625	11	A	$\nu(CC)_1$ (22) + $\nu(CC)_2$ (17) + $\nu(CC)_4$ (14) + $\nu(CC)_3$ (10)
n.o	1598	0.3	A	$\nu(CC)_5$ (21) + $\nu(CC)_6$ (19) + $\nu(CC)_2$ (15) + $\nu(CC)_1$ (10)
1500	1499	15	A	$\gamma(CH_3)_{as'}$ (56) + $\delta(CH_3)_{as'}$ (12)
1482 ?	1483	7	A	$\gamma(CH_3)_{as'}$ (18) + $\delta(CH)_2$ (16) + $\delta(CH)_1$ (14) + $\nu(CC)_4$ (14)
1463	1473	109	A	$\nu(NC)_3$ (57)
1457	1466	31	A	$\delta(CH_3)_s$ (14) + $\gamma(CH_3)_{as''}$ (25)
1456	1465	24	A	$\gamma(CH_3)_{as''}$ (64)
1439	1439	84	A	$\nu(NC)_3$ (11) + $\delta(CH_3)_s$ (57)
1379	1372	71	A	$\nu(NC)_1$ (21) + $\nu(NC)_2$ (24)
1366	1365	24	A	$\delta(CH)_2$ (14) + $\nu(CC)_6$ (12) + $\nu(NC)_2$ (10) + $\nu(CC)_2$ (10)
1329	1325	38	A	$\nu(CN)_1$ (15) + $\delta(CH)_4$ (11)
1281	1285	67	A	$\delta(CH)_3$ (22) + $\nu(CN)_2$ (18) + $\delta(CH)_1$ (12)
1223	1238	21	A	$\nu(CN)_2$ (31) + $\delta(CH)_4$ (13) + $\nu(CC)_1$ (11)
1155	1159	5	A	$\nu(CC)_6$ (10) + $\delta(CH)_1$ (14) + $\delta(CH)_2$ (36) + $\delta(CH)_4$ (17)
1138	1135	3	A	$\delta(CH)_3$ (20) + $\delta(CH)_1$ (17) + $\nu(NC)_1$ (12) + $\nu(CC)_5$ (10) + $\delta(ring1)_1$ (10)
n.o	1125	4	A	$\delta(CH_3)_{as''}$ (86)
1117/1115/1112	1117	26	A	$\nu(CC)_4$ (10) + $\delta(CH_3)_{as'}$ (29) + $\delta(ring1)_1$ (12)
1097	1092	8	A	$\nu(CC)_4$ (10) + $\delta(CH_3)_{as'}$ (24) + $\delta(ring2)_1$ (16)
1008	1013	9	A	$\nu(CC)_6$ (41) + $\nu(CC)_4$ (15) + $\nu(CC)_3$ (14) + $\delta(CH)_3$ (13) + $\delta(CH)_4$ (11)
n.o	960	0.06	A	$\gamma(CH)_4$ (110)
941	922	2	A	$\gamma(CH)_3$ (99)
911	911	27	A	δ(SH) (79)
899	892	5	A	$\delta(ring2)_1$ (39) + $\delta(ring1)_1$ (11) + $\nu(CN)_2$ (10)
n.o	840	0.5	A	$\gamma(CH)_1$ (85)
820	821	2	A	$\nu(CC)_1$ (15) + $\nu(CC)_2$ (13) + $\nu(CC)_5$ (13) + ν(CS) (11)
760	747	26	A	$\tau(ring2)_1$ (42) + $\gamma(CH)_2$ (26) + $\tau(ring1)_1$ (23)
~ 741	735	57	A	$\gamma(CH)_2$ (62) + $\tau(ring1)_1$ (12) + $\tau(ring2)_1$ (23)
716	718	2	A	$\nu(NC)_1$ (25) + $\delta(ring2)_2$ (22) + $\nu(NC)_2$ (12)
n.o	655	0.09	A	$\tau(ring1)_2$ (70) + γ(CS) (25)
616	607	2	A	$\delta(ring2)_3$ (49) + $\delta(ring1)_2$ (19) + ν(CS) (12)
n.o	576	0.03	A	$\tau(ring2)_2$ (44) + $\tau(ring2)_1$ (41) + $\tau(ring1)_1$ (27)
561	559	5	A	$\delta(ring2)_2$ (32) + $\delta(ring1)_2$ (20) + $\nu(NC)_1$ (14)
527	527	6	A	δ(NC) (17) + $\delta(ring2)_3$ (17) + $\delta(ring1)_2$ (15) + δ(CS) (14) + $\delta(ring2)_2$ (11)
n.i	432	5	A	$\tau(ring2)_3$ (76) + τ Butterfly (23)
n.i	391	3	A	ν(CS) (50) + $\delta(ring1)_1$ (16)
n.i	309	0.2	A	$\tau(ring2)_3$ (31) + τ Butterfly (29) + γ(CS) (28)
n.i	264	1	A	$\tau(ring2)_2$ (47) + $\tau(ring1)_1$ (21) + γ(NC) (16)
n.i	253	1	A	δ(NC) (60) + $\delta(ring2)_2$ (11)
n.i	206	1	A	δ(CS) (70)
n.i	192	14	A	τ(SH) (87)
n.i	117	9	A	γ(NC) (57) + τ Butterfly (18)
n.i	103	0.1	A	γ(CS) (32) + γ(NC) (21) + τ Butterfly (18) + $\tau(ring1)_2$ (17)
n.i	69	0.2	A	$\tau(CH_3)$ (94)

[a] See table 32 (Appendix) for the definition of symmetry coordinates. Abbreviations: s, symmetric; as, anti-symmetric; ν, stretching; δ, in-plane bending; γ, out-of-plane bending; τ, torsion. [b] Wavenumbers in cm^{-1}; n.i., not investigated. [c] IR intensities in km mol^{-1}. [d] PED's lower than 10% not shown.

4.4 Proposed Mechanism for Phototautomerization Reaction

A mechanism for the observed phototautomerization reactions can be postulated based on literature data for a number of heterocyclic compounds, including pyrrole,[111,112] indole,[113-115] imidazole,[116] phenol,[35] and thiophenol.[36] The proposed mechanism involves the hydrogen photodetachment, followed by recombination of the formed radical species (PIDA – photo-induced detachment association mechanism), instead the better known excited-state intramolecular proton transfer (ESIPT)[15-17] processes, in which a proton transfer is done along a pre-existing intramolecular hydrogen bond. For the studied molecular systems, we concluded that the ESIPT process is not favored, since the geometry of this type of molecules do not favor the intramolecular hydrogen bond between the nitrogen and sulphur atoms (see chapter 3).

According to the theoretical work of Sobolewski et al.,[19-22] the PIDA mechanism should be driven by a repulsive singlet (n/π)σ* state. These ^{1}(n/π)σ* states are dark in absorption (they have very small transition dipole moments with the ground state) and their potential energy surfaces are dissociative along SH/NH stretch coordinates. These properties render their spectroscopic detection extremely difficult but their existence could be inferred indirectly *via* the interpretation of the relaxation or fragmentation dynamics following photoexcitation.[19-22] On the other hand, since the ^{1}(n/π)σ* states are repulsive with respect to SH or NH stretch coordinates, they can predissociate the bound $^1\pi\pi^*$ and $^1n\pi^*$ states. Also, it has been shown that the (n/π)σ* potential energy surfaces generically exhibit a conical intersection with the electronic ground-state potential energy surface, this intersection providing a suitable mechanism for ultrafast internal conversion to the ground state, which appears as an alternative mechanism of relaxation to dissociation (useful to keep integrity of biomolecules like the nucleic acid bases, for example, upon UV light exposure).

Accordingly, one can propose that absorption of the UV photons would take the reactant species initially to a bright singlet state of (n/π)π* type, followed by internal conversion to the crucial excited singlet state of (n/π)σ* type, which promotes de dissociation though cleavage of the NH or SH bonds generating a hydrogen atom and the corresponding radical. Subsequent radical recombination might lead to the original species or attachment of the H atom to the S atom or N atom (depending if one is considering the thione→thiol or the inverse process) yielding the corresponding photoproduct as illustrated in the next figure considering the molecule 2-mercaptobenzimidazole (**figure 34**).

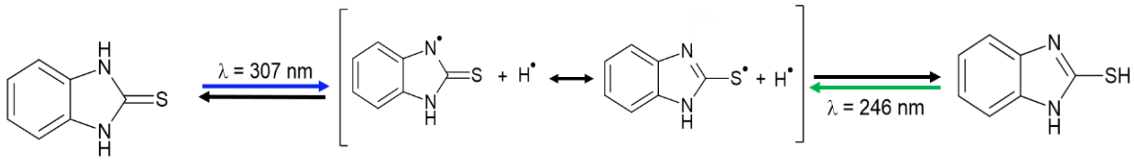

Figure 34. Proposed mechanism for phototautomerism in 2-mercaptobenzimidazole.

Note that the PIDA mechanism explains well the relative efficiency of the thione→thiol *vs.* thiol→thione tautomerizations, with the second being much more efficient than the first. In fact, since the radical species formed from both tautomers are the same, the product branch must depend essentially from the relative stability of the products resulting from recombination of the radicals, which in turn can be correlated with the affinity of the N *vs*. S atom (in the heterocyclic radical system) to the H atom, which favors the nitrogen moiety.

On the other hand, the observed observed apparent higher efficiency of the thione→thiol process in the two benzosubstituted imidazoles can be due to either a higher absorption coefficient of these species compared to the unsubstituted imidazoles (then the results are essentially kinetically determined, since independently of the involved thermodynamics the benzosubstituted molecules will transform faster – note that in the performed experiments, as duly stated in the proper place, one was not able to reach the conditions of photostationary equilibrium) or to a different detailed mechanism of intramolecular energy relaxation in the two types of molecules, associated with possible different energy levels structures in the two types of molecules.

4.4 Other Photoreactions

As referred in the previous section 4.3, besides phototautomerism other type of photoprocesses occur during the UV irradiations. In particular, formation of parent ketenimine was observed (as testified by the appearance in the spectra of the irradiated matrices of the characteristic ketenimine asymmetric stretching band in the 2000-2100 cm^{-1} region). Ketenimine type photoproducts were previously observed in other experiments performed in the LMCB, and their infrared spectra in argon matrix are well-known, in particular for the parent ketenimine.[117] All the bands of this molecule were identified in the present study, as it is shown in **table 21.**

For 2-MI, the two types of processes (photoisomerization and formation of ketenimine) were found to attain its maximum efficiency when irradiation was performed at λ = 290 nm. The identified

ketenimine photoproduct may have resulted from the photofragmentation of 2-MI, with the simultaneous cleavage of two C-N bonds of the heterocyclic ring, as shown in **figure 35**, which may have occurred by two different pathways. In the first pathway, the cleavage from 2-MI thione may lead to the initial formation of isothiocyanic acid (HNCS) together with the parent ketenimine. Although isothiocyanic acid signature was not directly observed, it was possible to identify its tautomer, thiocyanic acid (HSCN). This suggested that the tautomerization of isothiocyanic acid (HNCS) into thiocyanic acid (HSCN) may occurred at the same wavelength (λ = 290 nm). This reaction was already investigated in cryogenic matrices.[118] Besides this tautomerization, the rearrangement of thiocyanic acid into isothiofulminic acid (HSNC) may also take place.[118] Alternatively, and more acceptably due to the non-observation of isothiocyanic acid, the 2-MI thiol cleavage can be taking place, leading directly to the observed thiocyanic acid.

In addition to the thione→thiol photoisomerization and photofragmentation to ketenimine, which could be doubtlessly identified and constitute the major photoreaction channels, observation of additional bands whose origin could not be ascribed with certainty demonstrates that other processes take also place upon UV irradiation of 2-MI. The appearance of new bands in the N≡C stretching region (2100-2000 cm^{-1}) after the irradiation at 260 nm, suggests the formation of isonitriles.[119-122] The most intense band, which emerged at 2151 cm^{-1}, have been mainly attributed to ethyl isocyanide.[119-122]

The observed photochemistry of 1-M-2-MI closely follows that of 2-MI, indicating that the presence of the methyl substituent does not affect significantly the reactivity of the compound, which is essentially centered in the imidazole moiety. On the other hand, the two studied benzosubstituted compounds were found to be slightly more photostable in relation to photolysis, a result that seems to indicate that the presence of the benzenic ring fused to the reactive imidazole fragment leads to a stabilization of this later.

It shall be mentioned here that the greater photostability for fragmentation of the two benzosubstituted imidazoles is also partially responsible for the observed greater efficiency of the thione→thiol isomerization in these compounds compared to both 2-MI and 1-M-2-MI (see discussion above). Of course other factor is the fact that the photoisomerization in the benzosubstituted compounds takes place upon irradiation at longer wavelengths, which are rather inefficient in inducing the photolysis of the imidazole ring. Under these conditions, the photoisomerization channel does not have to compete with the photofragmentation channel.

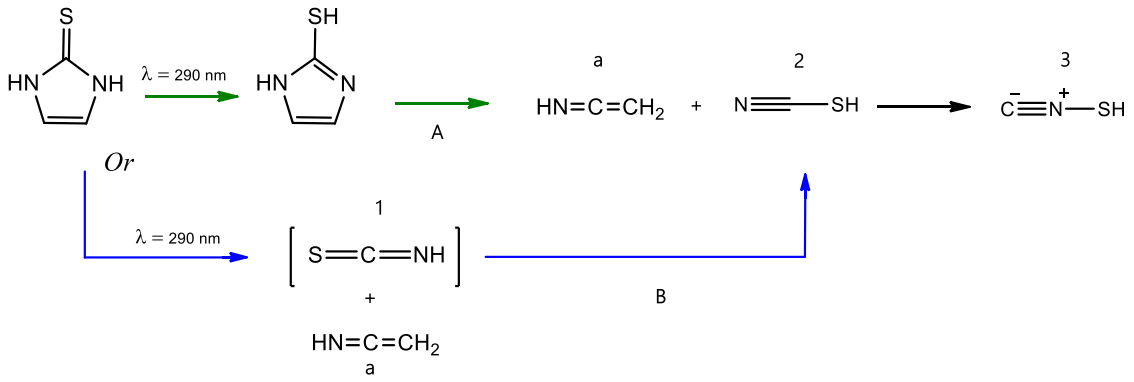

Figure 35. Proposed pathways for 2-mercaptoimidzole photolysis upon λ = 290 nm subsequent irradiations. In **A** pathway, the photolysis of 2-MI thiol leads to the direct formation of **2** (thiocyanic acid) and **a** (ketenimine). The rearrangement of **2** gives rise to the formation of **3** (isothiofulminic acid). In the proposed **B** pathway, the photolysis of 2-MI thione lead to the formation of **1** (isothiocyanic acid), which is not detected in the infrared spectra, and **a** (ketenimine). Upon λ = 290 nm irradiation, this photoproduct **1** may tautomerize into **2** (thiocyanic acid).

Table 21. Infrared spectra of photolysed of 2-mercaptoimidazole after λ = 290 nm irradiation.

Experimental $\tilde{\nu}^a$ (in this work)	Experimental $\tilde{\nu}^a$ (reported)[117, 118]	Approximate Description
Ketenimine		
3298/3294	3298	ν(N-H)
2039/2034	2039/2037	ν(N=C=C)as
1119	1124	ν(N=C=C)s + δ(CH_2)
1025	999	δ(CNH)
872	871	τ(N-H)
692	689	γ(H_2CC)
Thiocyanic acid		
2599	2581	ν(S-H)
2157	2182	ν(C-N)
964/947	958	δ(S-H)
Isothiofulminic acid		
2065	2064	ν(S-H)

[a] Wavenumbers in cm^{-1}. Abbreviations: s, symmetric; as, anti-symmetric; ν, stretching; δ, in-plane bending; γ, out-of-plane bending; τ, torsion. Literature data for isolated monomers of parent ketenimine,[117] thiocyanic acid,[118] isothiofulminc acid.[118]

CHAPTER V

Chapter V. Solid State Structural Analysis

5.1 Solid State Structural Characterization of 2-Mercaptoimidazole

It is well known that tautomerism depends on several factors, as temperature, solvent, pH and other factors.[15] Often, the tautomer present in the solid state corresponds to the most stable tautomer in solution. However, this is not a rule, since the crystallization process depends on the balance of thermodynamics and kinetics, and the final product may result from less stable but faster growing crystallization nuclei.

In this Chapter, investigations on the tautomerism of 2-mercaptoimidazole in the solid state are presented. As found in the case of gaseous phase, only the signature of 2-MI thione tautomer was observed for the compound in its neat solid phase.

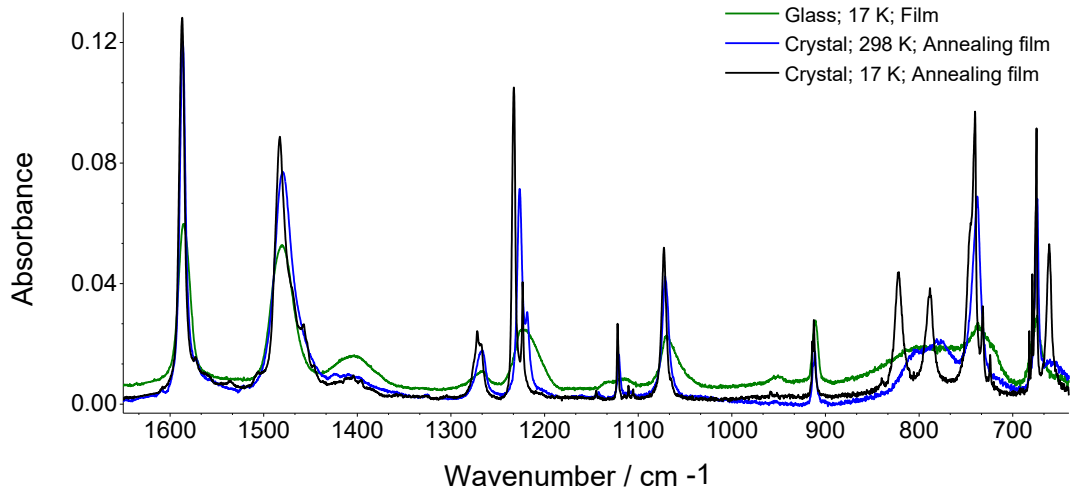

Figure 36. Infrared spectra of neat condensed phases of MIZ: (green) glassy state resulting from the fast deposition of the vapor of the compound onto a cold substrate kept at 17 K, (blue) crystalline state resulting from annealing of the glassy film up to 285 K and (black) crystalline state at 17 K after re-cooling of the sample.

Indeed, the infrared spectra of the glassy state resulting from the fast deposition of the vapor of the compound onto a cold substrate kept at 17 K, and the crystalline states resulting from annealing of the glassy film up to 285 K and then re-cooling it to 17 K (presented in **figure 36**) all are very similar (with the characteristic larger bandwidths for the spectra of the amorphous and high-temperature crystal). When the spectra of the neat condensed phases are compared with the calculated spectra of the isolated tautomers and with the IR ATR spectrum of the purchased sample of the compound, it is possible to identify the 2-MI thione tautomer as the constituting unit of the studied neat condensed phases of the compound, while no signals of presence of the thiol tautomer (as the characteristic νS-H band) were found in the spectra.

Several recrystallizations of 2-MI were undertaken using different solvents and different initial concentrations. Crystals were then analyzed by several techniques (including Raman microspectroscopy, DSC, PLTM and X-ray diffraction) and no desmotropy nor polymorphism were observed. The thermal behavior of 2-MI and its crystal structure at room temperature were previously reported:[102] the melting of 2-MI occurs at T_{fus} = (230.4 ± 0.1) K, with molar enthalpy of fusion $\Delta_{fus}H^{o}_{m}$ = (17.5 ± 0.3) kJ mol^{-1}, while no other processes were observed during the heating process from 25 to 250 ^{o}C.[102]

Besides 2-mercaptoimidazole, the other compounds addressed in this thesis in the solid state may be subject of future investigations.

5.2 Structural Characterization of a New Polymorph of 2-[(1*H*-Imidazol-2-yl)disulfanyl]-1*H*-imidazole

Disulfide bonds formation plays a central role in protein folding and for the synthesis of molecules with useful properties for biological applications.[122-125]

Here, the synthesis and structural characterization of the dimer of 2-MI bearing a disulfide bridge between the two imidazole rings (2-[(1*H*-Imidazol-2-yl)disulfanyl]-1*H*-imidazole, abbreviated as IDI; **figure 37**) are presented. Besides the theoretical investigation of the isolated molecule of the compound, studies were performed on the neat solid compound. In result of these studies, a new crystalline variety of the compound, herein designated as polymorph II, was found and characterized structurally by X-ray diffraction. The thermal behavior of the synthesized material was also evaluated, using both DSC and polarized light thermal microscopy.

The compound was obtained from a solution 2-MI in THF, after slow evaporation of the solvent at room temperature. A mixture of different materials was obtained, as found by Raman micro-spectroscopy, the major component being 2-MI; IDI crystals were found to correspond to the second more abundant material, while minor amounts of other non-characterized materials could also be observed (most probably corresponding to materials based on oligomers of 2-MI). The process was repeated with the time of solvent evaporation increased, by keeping it at a lower temperature. This procedure led to the total consumption of 2-MI, with IDI being obtained as the major product.

The afforded crystals of IDI were selected manually under microscope observation and crystals suitable for single crystal X-ray measurements were used for structure determination.

Very interestingly, the solved structure of IDI was found to constitute a new polymorph of the compound. The structure of the previously known polymorph of IDI (polymorph I) has been reported by Bazargani *et al.*,[126] being monoclinic, space group *C2/c*, with *a* = 14.083(3) Å, *b* = 6.3928(13) Å, *c* = 9.922(2) Å, and β = 122.29(3)°, and 4 molecules per unit cell. In the crystalline structure of polymorph, I, the asymmetric unit contains one half-molecule, and a twofold rotation axis passes through the middle of S—S bond (**figure 37**). The S—S bond distance is 2.0713(14) Å, the planar imidazole rings form an angle between them of 21.83(19)°, and the torsion angle of C—S—S—C is 83.62(17)°, with the two H atoms connected to the ring nitrogen atoms pointing to opposite directions (see **figure 37**). Intermolecular N—H···S hydrogen bonds result in the formation of linear chains along the *c*-direction; further π-π interactions between the imidazole rings of adjacent chains in the *a*-direction ($c_g \cdots c_g$ distance: 3.4466(19) Å) define the supramolecular structure in the crystal.

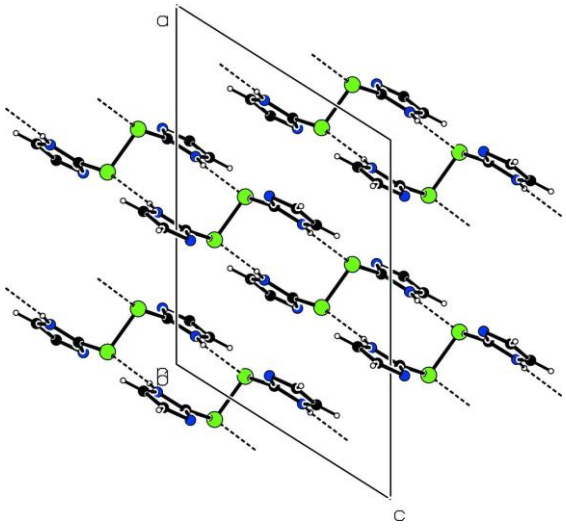

Figure 37. Projection of the crystal structure of polymorph I of IDI along the unit cell.[126]

The structure of the newly synthesized polymorph was found to be considerably more complex. The analyzed crystal was a 2-fold rotational twin through the (1 0 3) reciprocal vector or [101] direct vector. The compound crystallizes in the non-centrosymmetric *Ia* monoclinic space group, with $Z = 16$ and cell parameters: $a = 7.45910(10)$ Å, $b = 44.1680(8)$ Å, $c = 11.3522(2)$ Å and $\beta = 103.0240(10)^{o}$. The unit cell contains 4 symmetry independent molecules, which assume different conformations (**figure 38**). The crystal structure is stabilized by an extensive network of hydrogen bonds involving the NH groups as proton donors and the bare N atoms as acceptors. A total of 8 strong hydrogen bonds per molecule could be located, thus exhausting the molecules full ability for H-bonding, as shown in **table 22**.

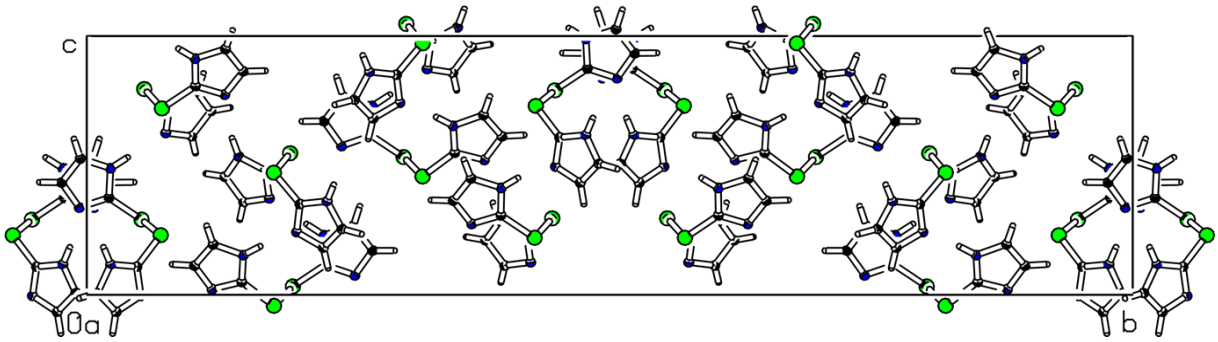

Figure 38. Projection of the crystal structure of polymorph II of IDI along the *a* axis of the unit cell.

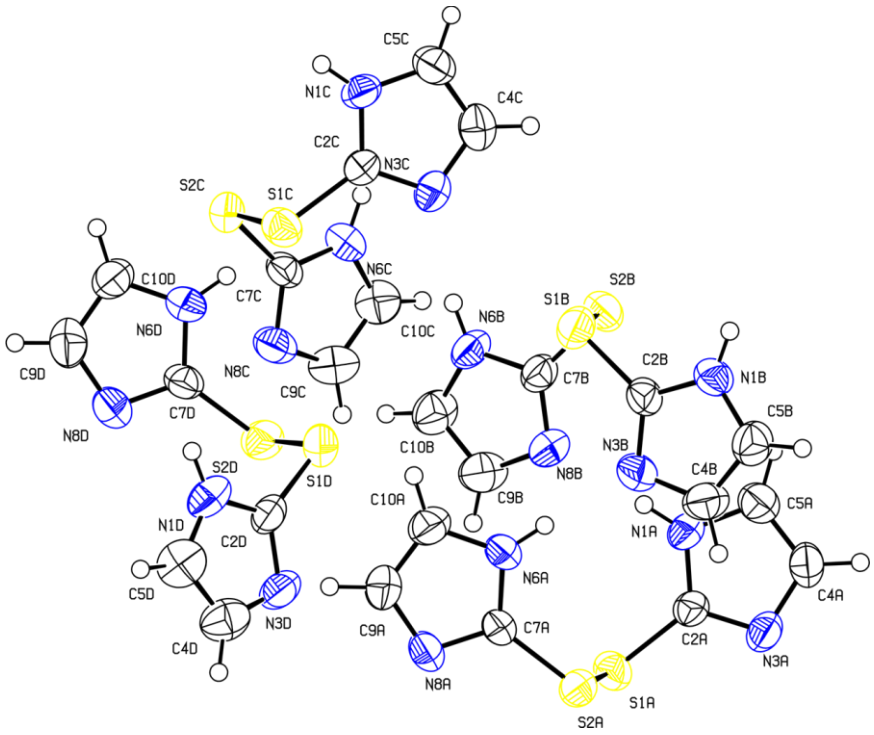

Figure 39. ORTEP drawing of the 4 symmetry independent molecules, with the adopted atom-labelling scheme.

Table 22. Distances and angles of intermolecular hydrogen bonds in IDI crystal structures. [a]

Hydrogen Bond		
D*-H···*A	***D*···*A* (Å)**	***D*-H···*A* (º)**
Polymorph II		
N1(A)-H1(A)···N8(B)	2.783 (4)	169.8
N6(A)-H6(A)···N3(B)	2.795 (5)	168.1
N1(B)-H1(B)···N3(A)$^{(i)}$	2.827 (4)	171.0
N6(B)-H6(B)···N3(C)	2.813 (5)	169.7
N1(C)-H1(C)···N3(D)$^{(ii)}$	2.778 (5)	163.3
N6(C)-H6(C)···N8(A)$^{(ii)}$	2.806 (5)	170.7
N1(D)-H1(D)···N8(D)$^{(iii)}$	2.787 (5)	171.6
N6(D)-H6(D)···N8(C)$^{(iv)}$	2.781 (4)	167.9
Polymorph I[129]		
N2-H2···S1$^{(v)}$	3.227(3)	153.0

[a] Symmetry codes: (i) 1+ x, ½ + z; (ii) x,y, 1+z; (iii) 1/2 + x,-y,z; (iv) 1+ x,y,z. (V) x, -y,z + ½.[127]

As it was referred above, in polymorph I, intermolecular N—H···S hydrogen bonds play an important role in structure stabilization, while polymorph II is mostly stabilized by the interaction between the NH groups as proton donors and the bare N atoms as acceptors. The dihedral angles C-S-S-C (º) and S-S distances (Å) for both polymorphs are presented in **table 23**. The polymorph II S-S distance average value is 2.082 Å, longer than the value measured in polymorph I (2.071 Å). This suggest that the charge delocalization from imidazole rings to the S-S bond is more effective in the case of polymorph I.

Table 23. Dihedral C-S-S-C angle and S-S distance in IDI crystal structures.

	Diedral C-S-S-C (º)	**S-S Distance (Å)**
Polymorph II		
C2(A)-S1(A)-S2(A)-C7(A)	100.77 (19)	2.079
C2(B)-S1(B)-S2(B)-C7(B)	95.49 (18)	2.089
C2(C)-S1(C)-S2(C)-C7(C)	77.81 (19)	2.082
C2(D)-S1(D)-S2(D)-C7(D)	80.21 (19)	2.079
Polymorph I[128]		
C2-S1-S2-C7	83.62 (19)	2.071

Besides the rather large number of molecules in the unit cell of polymorph II (referred to as Z), the most interesting structural feature of the crystal is that the 4 symmetry independent molecules (Z' = 4) in the unit cell exhausted the set of possible conformers for the isolated IDI molecule (see **figure 39**). The simultaneous presence in a crystal of all possible conformational states of a given species is, in fact,

noteworthy. The topic of Z' > 1 structures has been regarded as an attractive and challenging topic.[127] The interest in crystal structures and crystallization processes related to this uncommon packing phenomena (Z' > 1) have led to increase the research in this fields, mostly driven by the key relevance of understanding the properties of organic solid materials with high potential for drug development.[127] Interestingly, there have been reported several cases where Z' > 1 structures are more stable than Z = 1 polymorphs. This may be explained by the fact that high Z' structures may offer more convenient orientations of molecules for intermolecular interactions (e.g., straighter and shorter – stronger – hydrogen bonds; see **table 22**). On the other hand, Z' > 1 structures were found to exhibit most of times a lower density then Z = 1 structures, which has led to the interpretation that high Z' structures shall result from preassociated aggregates in solution and are in general less stable than the Z = 1 forms. It is also relevant to refer that Z' > 1 structures are a consequence of molecular flexibility and in general require that both compact and extended conformers exist for a given molecule. The lowest energy conformers tend to be more compact due to intramolecular stabilization (e.g., intramolecular H-bonding). Extended conformers lack these intramolecular interactions, leading to a higher molecular surface area for the establishment of intermolecular interactions. The conformers present in the crystals represent a balance of intra and intermolecular interactions.

In order to evaluate the balance of intra and intermolecular interactions that governs the formation of both polymorphs of the studied compound, and establish some energy-structure relationships, the optimized geometries and energies of the different conformers of IDI were determined at the DFT(B3LYP)/6-311++G(d,p) level of theory. The geometries of the 4 different symmetry-independent molecules in the crystal of polymorph II were used as starting structures in the optimization process (**figure 40**).

The optimized C and D structures of the compound (see **figure 41**) converge to the same geometry after optimization, which corresponds to the most stable conformation for the isolated IDI molecule, stabilized by an intramolecular interaction (conformation 3). Optimized A and B structures are higher in energy than the most stable form by 20.8 and 22.1 kJ mol^{-1} respectively (**Table 24**).

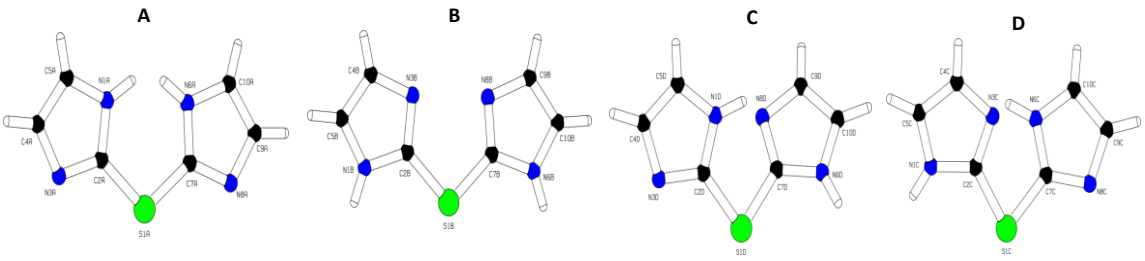

Figure 40. The 4 symmetry independent molecules of polymorph II of IDI depicted along the S1-S2 bond.

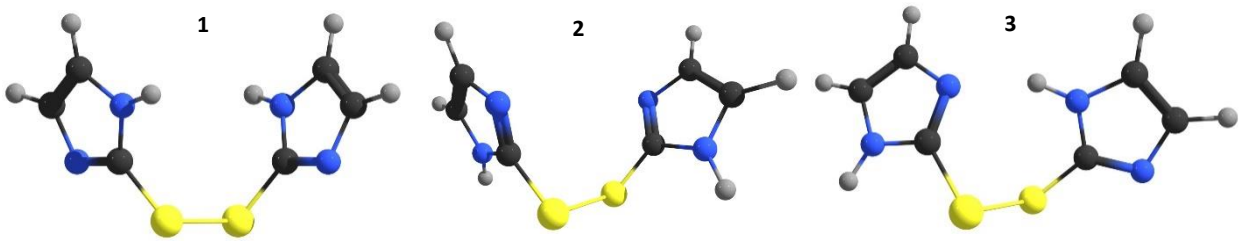

Figure 41. IDI conformations obtained by quantum chemical calculations at DFT(B3LYP)/6-311++G(d,p) level of approximation.

Table 24. DFT(B3LYP)/6-311++G(d,p) calculated relative energies values of the C-S-S-C dihedral angles for the optimized geometries of IDI starting from the 4 different geometries found in the studied crystal.

IDI Conformations	Relative Energy	Dihedral C-S-S-C (º)
1	22.1	78.4
2	20.8	75.7
3	0.0	84.3

The lowest energy conformer of IDI (conformer 3) corresponds to the most closed and compact structure, as result of the strong intramolecular H-bond type interaction established between the unprotonated nitrogen of one of the imidazole rings and the NH fragment of the second imidazole ring of the molecule. Besides, in this conformation of the IDI molecule the number of positions available for establishing intermolecular H-bonds is reduced to half, when compared with the higher energy conformers 1 and 2. Then, to fulfill the 4 H-bond valences with intermolecular H-bonds in the crystal, conformer C/D has to break the intramolecular H-bond. This fact makes the energetic balance associated with the establishment of the intermolecular H-bonds less favorable for C/D than for both A and B forms, which require only minor structural rearrangements during aggregation. These facts led to the conclusion that the simultaneous observation of the 3 conformers of IDI in the polymorph II results from a compromise between the greater intrinsic stability of the isolated C/D form, and the more efficient in energetic terms packing achieved by the higher energy conformers A and B.

As discussed above, the lowest energies conformers (predicted for the gas phase) of flexible molecules are not often the preferential structures adopted for packing arrangements. Higher energy conformers predicted for the gas phase may have a higher surface area that increases their potential to stablish intermolecular interactions and, consequently, may lead to more ordered, lower energy,

molecular packings. It is what occurs in the case of polymorph I, where the single selected conformer B has an ideal conformation to fulfil the H-bond valences of the atoms in the molecule. In this higher order crystal packing, the intermolecular interactions play the key role in stabilization, instead of the intrinsic stability promoted by the isolated C/D conformation in the case of polymorph II.

As it was referred, the polymorph II of IDI, obtained by recrystallization from THF, was first identified by Raman microscopy. The Raman spectrum recorded at room temperature and the 6-311++G(d,p) calculated spectrum of the less energetic conformer of IDI are presented in **figure 42**. The strong feature observed at 326.5 cm^{-1} is characteristic of the ν(S-S) stretching vibration (see the spectrum of 2-MI presented above).

Polymorph II of IDI was also analyzed by PLTM and DSC. According to the obtained results, an exothermic solid-solid transition occurs at T = (155 ± 02) °C, while at T = (189 ± 04) °C degradation of the resultant structure (**figure 44**) occurs. It is possible to see in the PLTM images (**figure 43**) morphological changes in the crystal due to these two processes. Although other investigations have to be performed on this compound to extract more precise conclusions, the results suggest that the less energetic polymorph I may be the form formed from polymorph II during the heating process. Thermal and spectroscopic investigations on these samples will continuing to be done in order to clarify this structure.

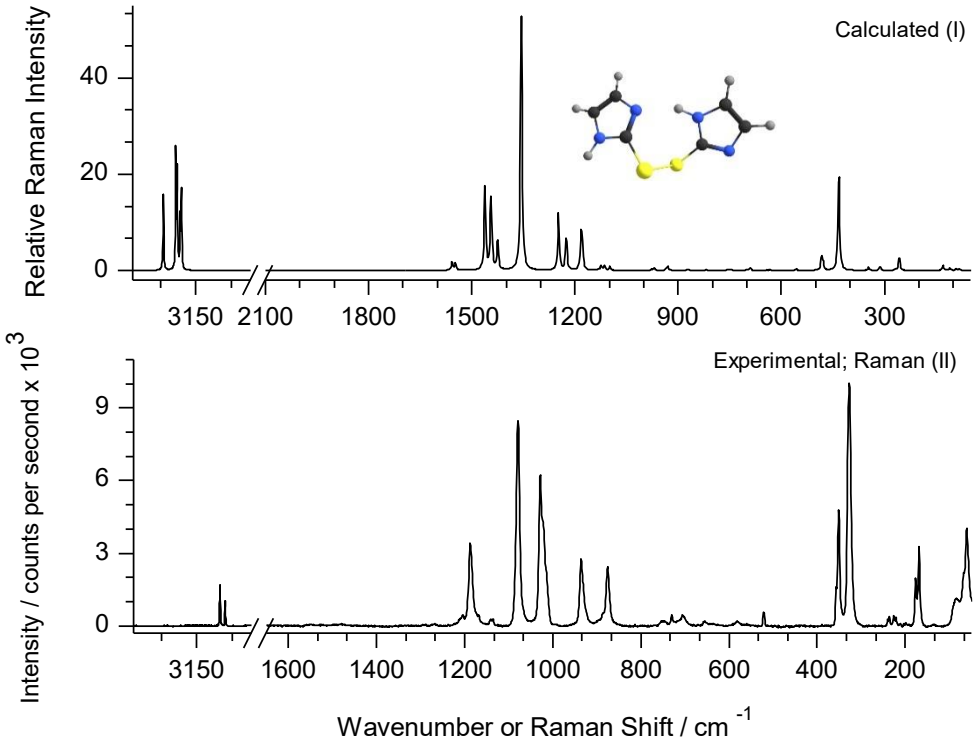

Figure 42. (I) DFT(B3LYP)/6-311++G(d,p) Raman spectrum for the minimum energy configuration of IDI simulated using Lorentzian functions with fwhw of 5 cm^{-1}. This spectrum is unscaled. (II) Experimental Raman spectrum of IDI.

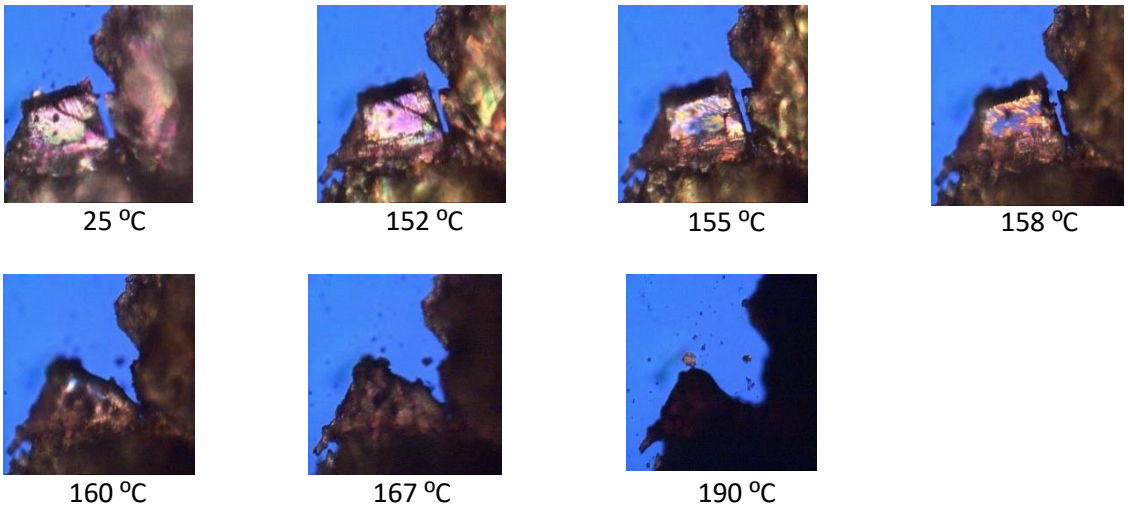

Figure 43. Polarized light thermal microscopy images collected along the IDI (polymorph II) heating from 25 ºC to 200 ºC, β = 10 ºC min^{-1}, amplification 200x.

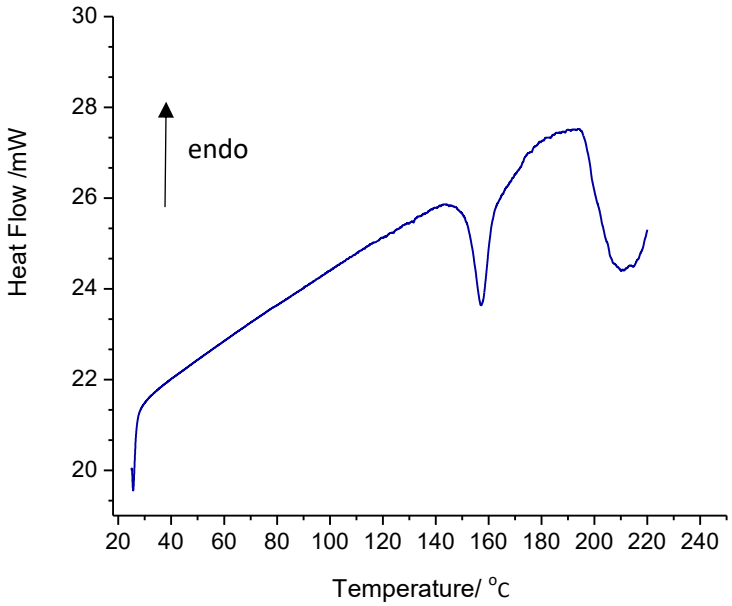

Figure 44. DSC heating curve from 25 to 220 ºC, β = 10 ºC min^{-1} of polymorph II of IDI (m = 1.56 mg).

CONCLUSION AND FUTURES PERSPECTIVES

Conclusion and Future Perspectives

Calculations predicted the thione form as the most stable tautomer of the series of molecules studied in this project. It was concluded that intramolecular interactions of bond-dipole / bond-dipole type are the major cause determining the relative energies of the two tautomers of 2-MI and 1-M-2-MI, while the relative stabilization of the thione tautomer compared to the thiol form in 2-MBI and 1-M-2-MBI (compared to 2-MI and 1-M-2-MI) is probably related predominantly with the relative importance of ring mesomerism. Another relevant conclusion extract from calculations is that the values of ∢N-H···S angles are considerably smaller than the ideal value for a typical proton donor/acceptor interaction (180°) and considerably smaller than the value generally accepted for the ∢ D–H···A angle (D, donor; A, acceptor).

The comparison of the infrared spectra of the monomeric molecules isolated in argon matrices with the spectra calculated at DFT(B3YP)/6-311++G(d,p) level of approximation led to the conclusion that molecules exist exclusively in their thione forms.

Upon *in situ* narrowband UV irradiation, the as-deposited thiones were partially converted into their thiols tautomeric forms. Irradiations were performed taking into account the experimental UV maximum absorption wavelengths of the compounds in ethanol solution and their calculated TD-DFT spectra. It was proved that than thione→thiol conversion is more efficient in the case of benzoderivatives and the asymmetry introduced by methyl group in 2-mercaptoimidazole and 2-mercaptobenzimidazole does not induce any significant change in the results. Also, the reverse photoreversibility of the process was proved for the benzosubstituted 2-mercaptoimidazoles by irradiation of the thione forms at λ = 246 nm. This photoprocess show a greater efficiency than the thione→thiol conversion.

The possibility of selectively convert each one of the tautomers of 2-MBI and 1-M-2-MBI into the other one using optical excitation at different wavelengths and their photostability make these molecules possible candidates to be exploited as UV-light-activated molecular switches for applications in several fields (*e.g.,* materials science, supramolecular chemistry and drug design).

The postulated mechanism for these reactions, which receive support from literature data on similar compounds, involves radical formation and subsequent hydrogen atom recombination. The observation of the proposed radical intermediate could not be done with certainty (but suggested for one of the compounds mentioned). Other experiments (e.g., EPR measurements) shall be undertaken in the

future to confirm the assumption here made and detect the radicals putatively involved in these photoreactions. Nevertheless, the proposed mechanism explains well the observed asymmetry in the efficiency of the thione→thiol *vs* thiol→thione processes.

Other relevant conclusion taken from this work is that methimazole, a widely used antithyroid drug, can exist as two tautomeric forms. Since the action of methimazole involves a mechanism of molecular recognition that inhibits the thyroid hormone synthesis by the enzyme thyroperoxidase and since tautomers are different molecules, with different molecular shapes, which establish different non-covalent interactions with molecular receptors, it would be noteworthy to perform other investigations to evaluate the molecular affinity between the two tautomers of methimazole and the target involved.

Besides phototautomerization, other processes occur during the UV irradiations. The 290 nm induced photolysis of 2-MI was found to occur with subsequent formation of ketenimine, thiocyanic acid and isolthiofulmic acid. These photoproducts probably result from simultaneous cleavage of two C-N bonds of the imidazole ring. The observed photochemistry of 1-M-2-MI is similar to the observed for 2-MI, demonstrating that the presence of methyl group does not influence significantly the reactivity. On the other hand, the benzosubstituted molecules were found to exhibit greater stability for fragmentation, which is in part the reason for the greater efficiency observed in these molecules in relation to the tautomerization (when compared to 2-MI and 1-M-2-MI). Photoproducts resulting from photolysis of the compounds under study will be subject of investigations.

In the solid state of 2-MI only the thione tautomer was observed. Polymorphism was not observed for this compound in spite of the attempts made to produce other crystalline forms. In the future, other recrystallization methods and the influence of pressure in polymorphism in these type of molecules can be exploited.

2-[(1*H*-Imidazol-2-yl)disulfanyl]-1*H*-imidazole (IDI) was obtained from 2-mercaptoimidazole in an easy way by oxidation reaction of 2-MI to a disulfide dimer. This makes molecule a good candidate to act as a redox switch for several applications. The structure of the new synthetized polymorph of 2-[(1*H*-Imidazol-2-yl)disulfanyl]-1*H*-imidazole was investigated in details. It is a high Z' structure with four the 4 symmetry independent molecules (Z' = 4) in the unit cell and which exhausted the set of possible conformers for the isolated IDI molecule.

References

1. Raper, E. S. *Coord. Chem. Rev*. **1996**, 153, 199–255.

2. Raper, E. S. *Coord. Chem. Rev.* **1985**, 61, 115–184.

3. Isaia, F.; Aragoni, M. C.; Arca, M.; Bettoschi, A.; Caltagirone, C.; Castellano, C.; Demartin, F.; Lippolis, V.; Pivetta, T; Valletta, E. *Dalton Trans*. **2015**, 44, 9805–9814.

4. Emiliano, A. B.; Governale, L.; Parks, M.; Cooper, D. S. *J. Clin. Endocrinol. Metab*. **2010**, 5, 2227–2233.

5. Cooper, D. S. *N. Engl. J. Med.* **2005**, 352, 905–917.

6. Lommen, G. V.; Doyon, J.; Coesemans, E.; Boeckx, S.; Cools, M.; Buntinx, M.; Hermans, B.; VanWauwe, J. *Bioorg. Med. Chem. Lett.* **2005**, 15, 497–500.

7. Alvarez-Bustamante, R.; Negron-Silva, G.; Abreu-Quijano, M.; Herrera-Hernandez, H.; Romero-Romo, M.; Cuan, A.; Palomar-Pardave, M. *Electrochim. Acta* **2009**, 54, 5393–5399.

8. Perez-Peña, J.; Gonzalez-Davila, G.; Suarez-Tangil, M.; Hernandez-Brito, J. *Collect. Czech. Chem. Com.* **1989**, 54, 2045–2053.

9. Stoyanov, S.; Stoyanova, T.; Antonov, L.; Karagiannidis, P.; Akrivos, P. *Monatsh. Chem*. **1996**, 127, 495–504.

10. Muller, P. *Pure Appl. Chem*. **1994**, 66, 1077–1184.

11. Watson, J. D.; Crick, F. H. C. *Nature* **1953**, 171, 737–738.

12. Pray, L. *Nature Education* **2008**, 1, 214.

13. Kamounah, F. H.; Antonov, L.; Petrov, V.; van der Zwan, G. J. *J. Phys. Org. Chem*. **2007**, 20, 313–320.

14. Nedeltcheva, D. L.; Antonov, L. *J. Phys. Org. Chem*. **2009**, 22, 274–281.

15. Liudmil, A. *Tautomerism: Concepts and Applications in Science and Technology*, Wiley-VCH Verlag GmbH & Co. KGaA, Weinheim, Germany, **2016**.

16. Ortiz-Sánchez, J. M.; Gelabert, R.; Moreno, M.; Lluch, J. M. *J. Phys. Chem. A* **2006**, 110, 4649–4656.

17. Padalkar, V. S.; Seki, S. *Chem. Soc. Rev.* **2016**, 45, 169–202.

18. Pagacz-Kostrzewa, M.; Reva, I. D.; Bronisz, R.; Giuliano, B. M.; Fausto, R.; Wierzejewska, M. *J. Phys. Chem. A* **2011**, 115, 5693–5707.

19. Sobolewski, A. L; Domcke, W. *Chem. Phys*. **2000**, 259, 181–191.

20. Sobolewski, A. L; Domcke, W.; Dendonder-Lardeux, C.; Jouvet, C. *Phys. Chem. Chem. Phys.* **2002**, 4, 1093–1100.

21. Sobolewski, A. L; Domcke, W. *Science* **2003**, 302, 1693–1694.

22. Sobolewski, A. L. *Phys. Chem. Chem. Phys.* **2008**, 10, 1243–1247.

23. Nowak, M. J.; Fulara, J.; Łapiński, L. *J. Mol. Struct*. **1988**, 175, 91–96.

24. Łapiński, L.; Nowak, M. J.; Les, A.; Adamowicz, L. *J. Am. Chem. Soc.* **1994**, 116, 1461–1467.

25. Łapiński, L.; Nowak, M. J.; Rostkowska, H. *J. Chem. Phys*. **2017**, 146, 094306.

26. Nowak, M.J.; Łapiński, L.; Fulara, J.; Les, A; Adamowicz, l. *J. Phys. Chem*. **1992**, 96, 1562–1569.

27. Gerega, A.; Łapiński, L.; Nowak, M.J.; Furmanchuk, A.; Leszczynski, J. *J. Phys. Chem. A* **2007**, 111, 4934–4943.

28. Łapiński, L.; Fulara, J.; Czerminski, R.; Nowak, M. J. *Spectrochim. Acta Part A* **1990**, 46, 1087– 1096.

29. Nowak, M. J.; Łapiński, L.; Fulara, J.; Les, A.; Adamowicz, L. *J. Phys. Chem*. **1991**, 95, 2404-2411.

30. Reva, I.; Almeida, B. J. A. N.; Łapiński, L.; Fausto, R. *J. Mol. Struct.* **2012**, 1025, 74–83.

31. Nowak, M. J.; Łapiński, L.; Fulara, J. *Spectrochim. Acta Part A* **1989**, 45, 229–242.

32. Łapiński, L.; Reva, I.; Nowak, M. J.; Fausto, R. *Phys. Chem. Chem. Phys.* **2011**, 13, 9676–9684.

33. Reva, I.; Nowak, M. J.; Łapiński, L.; Fausto, R. *J. Phys. Chem. B* **2012**, 116, 5703–5710.

34. Vranken, H.; Smets, J.; Maes, G.; Łapiński, L.; Nowak, M. J.; Adamowicz, L. *Spectrochim. Acta Part A* **1994**, 50, 875–889.

35. Giuliano, B. M.; Reva, I.; Łapiński, L; Fausto, R. *J. Chem. Phys.* **2012**, 136, 024505.

36. Reva, I.; Nowak, M. J.; Łapiński, L.; Fausto, R. *Phys. Chem. Chem. Phys*. **2015**, 17, 4888–4898

37. Nowak, M. J.; Reva, I.; Rostkowska, H.; Łapiński, L. *Phys. Chem. Chem. Phys.* **2017**, 19, 11447–11454.

38. Bahou, M.; Das, P.; Lee, Y.-F.; Wu, Y.-J.; Lee, Y.-P. *Phys. Chem. Chem. Phys.* **2014**, 16, 2200–2210.

39. Ruzi, M.; Anderson, D. T. *J. Phys. Chem. A* **2013**, 117, 13832–13842.

40. Kranendonk, J. V. *Solid Hydrogen: Theory of the Properties of Solid H2, HD and D2*, Plenum Press, New York, USA, 1st ed., **1983**, pp. 132–172.

41. Silvera, I. F. *Rev. Mod. Phys.* **1980**, 52, 393–452.

42. McCrone, W.C. *Polymorphism in Physics and Chemistry of the Organic Solid State*, ed. by Fox, D.; Labes, M. M.; Weissenberg, A., Wiley Interscience, New York, USA, **1965**.

43. Bernstein, J. *Cryst. Growth Des.* **2011**, 11, 632–650.

44. Jacobson, P. *Ber. Dtsch. Chem. Ges.* **1888**, 21, 2624–2631.

45. Elguero, J. *Cryst. Growth Des.* **2011**, 11, 4731–4738.

46. Aronova, E.B.; Ginak, A. I. *Russ. J. Gen. Chem.* **2001**, 71, 1605–1607.

47. Aronova, E.B.; Ginak, A. I. *Russ. J. Appl. Chem.* **2002**, 75, 1885–1886.

48. Holzer, W.; Claramunt, R. M.; López, C.; Alkorta, I.; Elguero, J. *Solid. State Nucl. Magn. Reson.* **2008**, 34, 68–76.

49. Eichen, Y.; Botoshansky, M.; Peskin, U.; Scherl, M.; Haarer, D.; Khatib, S. *J. Am. Chem. Soc.* **1997**, 119, 7167–7168.

50. Khatib, S.; Tal, S.; Godsi, O.; Peskin, U.; Eichen, Y. *Tetrahedron* **2000**, 56, 6753–6762.

51. Schmidt, A.; Kababya, S.; Appel, M.; Khatib, S.; Botoshansky, M.; Eichen, Y. *J. Am. Chem. Soc.* **1999**, 121, 11291–11299.

52. Alkorta, I.; Rozas, I.; Elguero, J. *J. Chem. Soc., Perkin Trans.* **1998**, 2, 2671–2676.

53. Horta, P.; Henriques, M. S. C.; Brás, E. M.; Murtinheira, F.; Nogueira, F.; O'Neill, P.M.; Paixão, J. A.; Fausto, R.; Cristiano, M. L. S. *Pure Appl. Chem*. **2017**, 86, 765-780.

54. Halcrow, M. A.; Powell, H. R.; Duer, M. *J. Acta Crystallogr. Sect. B* **1996**, 52, 746–752.

55. Llamas-Saiz, A. L.; Foces-Foces, C.; Fontenas, C.; Jagerovic, N.; Elguero, J. *J. Mol. Struct.* **1999**, 484, 197–205.

56. Jimenez, J. A.; Claramunt, R. M.; Escolastico, C.; Elguero, *J. Struct. Chem.* **2000**, 11, 77–83.

57. Lewars, E. G. *Computational Chemistry*, Springer Netherlands: Dordrecht, Netherlands, **2011**.

58. Jensen, F. *Introduction to Computational Chemistry*, 2nd Ed. John Wiley & Sons, Chichester, UK, **2007**.

59. Parr, R. G.; Yang, W. *Density-functional theory of atoms and molecules*, Oxford University Press, **1989**.

60. Szabo, A.; Ostlund, N. S. *Modern quantum chemistry: introduction to advanced electronic structure theory*, Dover Publications, New York, USA, **1996**.

61. Hohenberg, P.; Kohn, W. *Phys. Rev. B* **1964**, 136, 864–871.

62. Kohn, W.; Sham, L. J. *Phys. Rev. A* **1965**, 140, 1133–1138.

63. Becke, A. D. *Phys. Rev. A* **1988**, 38, 3098–3100.

64. Lee, C.; Yang, W.; Parr, R. G. *Phys. Rev. B* **1988**, 37, 785–789.

65. Mehlich, B.; Savin, A.; Stoll, H.; Preuss, *H. Chem. Phys. Lett*. **1989**, 157, 200–207.

66. Vosko, S. H.; Wilk, L.; Nusair M. *Can. J. Phys*. **1980**, 58, 1200–1211.

67. Parr, R. G.; Yang, W. *Oxford Science Publications*, Oxford, UK, **1989**.

68. McLean, A. D.; Chandler, G. S. *J. Chem. Phys*. **1980**, 72, 5639–5648.

69. Frisch, M. J.; Pople, J. A.; Binkley, J. S. *J. Chem. Phys*. **1984**, 80, 3265–3269.

70. Clark, T.; Chandrasekhar, J.; Spitznagel, G. W.; Schleyer, P. V. R. *J. Comput. Chem*. **1983**, 4, 294–301.

71. Wilson, E. B.; Decius, J. C.; Cross, P. C. *Molecular Vibrations: The Theory of Infrared and Raman Vibrational Spectra*, Dover Publications, New York, USA, **1980.**

72. Fausto, R. *In Química Síntese e Estrutura.*; Burrows, H. D., Pereira, M. M., Escolar Editora: Lisboa, Portugal, **2006**.

73. Dunkin, I. R. *Matrix-Isolation Techniques: a practical approach*, Oxford University Press Inc., Oxford, UK, **1998**.

74. Whittle, E.; Dows, D. A.; Pimentel, G. C. *J. Chem*. *Phys*. **1954**, 22, 1943–1944.

75. Fausto, R. *Low Temperature Molecular Spectroscopy*, Springer Netherlands: Dordrecht, Netherlands, **1996**.

76. Dunkin, I. R. *Matrix Photochemistry. In CRC Handbook of Organic Photochemistry and Photobiology*, Horspool, W. M.; Song. P. S., 2nd Ed., CRC Press, USA, **2003**.

77. Fausto, R.; Khriachtchev, L.; Hamm, P. *Conformational Changes in Criogenics Matrices. In Physics and Chemistry at Low Temperature*; Khriachtchev, L., Pan Stanford Publishing: Singapore, **2011**, 51.

78. Fausto, R.; Gómez-Zavaglia *A. Light Induced Reactions in Cryogenics Matrices. In Photochemistry*; Albini. A, Ed., Royal Society of Chemistry Pubs, Cambridge, UK, **2011**.

79. Fausto, R.; Maçôas, E.M.S. *J. Mol. Struct*. **2001**, 563–564, 27–40.

80. Nunes, C. M.; Reva, I.; Rosado, M. T. S.; Fausto, R. *Eur. J. Org. Chem*. **2015**, 7484–7493.

81. Horta, P; Kuş, N.; Henriques, M. S. C.; Paixão, J. A.; Coelho, L.; Nogueira, F.; O'Neill, P.; Fausto, R.; Cristiano, M. L. S. *J. Org. Chem*. **2015**, 80, 12244–12257.

82. Schrader, B. *Infrared and Raman Spectroscopy - Methods and Applications*, Verlag GmbH & Co. KGaA, Weinheim, Germany, **1995**.

83. Atkins, P. W. *Physical Chemistry*, 4th Ed., Oxford University Press, Oxford, UK, **1992**.

84. Stuart, B. H. *Infrared Spectroscopy: Fundamentals and Applications*, John Wiley & Sons, Chichester, UK, **2004**.

85. Raman, C. V.; Krishnan, K. S. *Nature* **1928**, 121, 501–502.

86. Smith, E.; Dent, G. *Modern Raman spectroscopy: a practical approach*, John Wiley & Sons, Chichester, UK, **2005**.

87. Long, D. A. *The Raman Effect*, John Wiley & Sons, Chichester, UK, **2002**.

88. McCreery, R. L. *Raman Spectroscopy for Chemical Analysis*, John Wiley & Sons, Hoboken, USA, **2000**.

89. Pecharsky, P. *Fundamentals of Powder Diffraction and Structural Characterization of Materials*, 2nd Ed., Springer US, **2009**.

90. McCrone, W. C.; McCrone, L. B.; Delly, J. G. *Polarized light microscopy*, Ann Arbor Science Publishers, Chicago, USA, **1978**.

91. Kuhnert-Brandstätter, M. *Thermomicroscopy in the Analysis of Pharmaceuticals*, Pergamom Press, Oxford, UK, **1971**.

92. Charsley, E. L.; Stewart, C.; Barnes, P. A.; Parkes, G. M. B. J. *Therm. Anal. Calorim*. **2003**, 72, 1087–1090.

93. Mojumdar, S. C.; Sain, M.; Prasad, R. C.; Sun, L.; Venart, J. E. S. *J. Therm. Anal. Calorim*. **2007**, 90, 653–62.

94. Brown, M. E. *Introduction to Thermal Analysis*; 1st ed., Kluwer Academic Publishers: Dordrecht, Netherlands, **2004**.

95. Frisch, M. J.; Trucks, G. W.; Schlegel, H. B.; Scuseria, G. E.; Robb, M. A.; Cheeseman, J. R.; Scalmani, G.; Barone, V.; Mennucci, B.; Petersson, G. A.; Nakatsuji, H.; Caricato, M.; Li, X.; Hratchian, H. P.; Izmaylov, A. F.; Bloino, J.; Zheng, G.; Sonnenberg, J. L.; Hada, M.; Ehara, M.; Toyota, K.; Fukuda, R.; Hasegawa, J.; Ishida, M.; Nakajima, T.; Honda, Y.; Kitao, O.; Nakai, H.; Vreven, T.; Montgomery Jr., J. A.; Peralta, J. E.; Ogliaro, F.; Bearpark, M.; Heyd, J. J.; Brothers, E.; Kudin, K. N.; Staroverov, V. N.; Kobayashi, R.; Normand, J.; Raghavachari, K.; Rendell, A.; Burant, J. C.; Iyengar, S. S.; Tomasi, J.; Cossi, M.; Rega, N.; Millam, J. M.; Klene, M.; Knox, J. E.; Cross, J. B.; Bakken, V.; Adamo, C.; Jaramillo, J.; Gomperts, R.; Stratmann, R. E.; Yazyev, O.; Austin, A. J.; Cammi, R.; Pomelli, C.; Ochterski, J. W.; Martin, R. L.; Morokuma, K.; Zakrzewski, V. G.; Voth, G. A.; Salvador, P.; Dannenberg, J. J.; Dapprich, S.; Daniels, A. D.; Farkas, Ö.; Foresman, J. B.; Ortiz, J. V; Cioslowski, J.; Fox, D. J. Gaussian Inc Wallingford CT. **2009**.

96. Schachtschneider, J. H.; Mortimer, F. *Vibrational Analysis of Polyatomic Molecules*, VI: FORTRAN IV *Vibrational Analysis of Polyatomic Molecules*, VI, Shell Developmen, Emeryville, CA, USA, **1969**.

97. Pulay, P.; Fogarasi, G.; Pang, F.; Boggs, J. E. *J. Am. Chem. Soc.* **1979**, 101, 2550–2560.

98. Lu, T.; Chen, F. *J. Comp. Chem*. **2012**, 33, 580–592.

99. Bruker AXS Inc.: Madison, Wisconsin, USA, **2006**.

100. Sheldrick, G. M. *Acta Crystallogr. Sect. C Struct. Chem*. **2015**, C71, 3–8. Sabbah, R.; Xu-wu, A.; Chickos, J. S.; Leitão, M. L. P.; Roux, M. V.; Torres, L. A. *Thermochim. Acta* **1999**, 331, 93–204.

101. Sabbah, R.; Xu-wu, A.; Chickos, J. S.; Leitão, M. L. P.; Roux, M. V.; Torres, L. A. *Thermochim. Acta* **1999**, 331, 93–204.

102. Silva, A. L. R.; Morais, M. F. V.; Silva, M. D. M. C.; Simões, R. C.; Bernardes, C. E. S.; Piedade, M. F. M; Piedade, M. E. M. *J. Chem. Thermodynamics* **2016**, 95, 35–48.

103. Form, G. R.; Raper, E. S.; Downie, T. C. *Acta Cryst.* **1976**, B32, 345–348.

104. Lodochnikova, O. A.; Bodrov, A.V.; Saifina, A. F.; Nikitina, L. E.; Litvinov, I. A. *J. Struct. Chem.* **2013**, 54, 140–147.

105. Khan, H.; Badshah, A.; Shaheen, F.; Giek, C.; Qureshi, R. A. *Acta Crystallogr. Sect. E. Crystallogr. Commun.* **2008***,* 64, 2056–9890.

106. Arunan, E.; Desiraju, G. R.; Klein, R. A.; Sadlej, J.; Scheiner, S.; Alkorta, I.; Clary, D. C.; Crabtree, R. H.; Dannenberg, J. J.; Hobza, P.; Kjaergaard, H. G.; Legon, A. C.; Benedetta, M.; Nesbitt, D. J. P*ure Appl. Chem.* **2011**, 83, 1619–1636.

107. Bader, R. F. W. *Atoms in Molecules: A Quantum Theory*, Clarendon Press, Oxford, UK, **1994**.

108. Kruszewski*,* J.*;* Krygowski*,* T. M. *Tetrahedron Lett*. **1972**, 3839–3842.

109. Bird, C. W. *Tetrahedron* **1985**, 41, 1409-1414.

110. Khvorostov, A.; Łapiński, L.; Rostkowska, H.; Nowak, M. J. *Photochem. Photobiol.* **2005**, 81, 1205–1211.

111. Wei, J.; Kuczmann, A.; Riedel, J.; Renth, F.; Temps, F. *Phys. Chem. Chem. Phys.* **2003**, 5, 315–320.

112. Cronin, B.; Nix, M. G. D.; Qadiri, R. H.; Ashfold, M. N. R. *Phys. Chem. Chem. Phys.* **2004**, 6, 5031–5041.

113. Nix, M. G. D.; Devine, A. L.; Cronin, B.; Ashfold, M. N. R. *Phys. Chem. Chem. Phys.* **2006**, 8, 2610–2618.

114. Godfrey, T. J.; Yu, H.; Ullrich, S. Chem. Phys., 2014, 141, 044314.

115. Godfrey, T. J.; Yu, H.; Biddle, M. S.; Ullrich, S. *Phys. Chem. Chem. Phys.* **2015**, 17, 25197–25209.

116. Devine, A. L.; Cronin, B.; Nix, M. G. D.; Ashfold, M. N. R. *J. Chem. Phys.* **2006**, 125, 184302.

117. Nunes, C. M.; Reva, I.; Pinho e Melo, T. M. V. D.; Fausto, R.; Šolomek, T.; Bally, T. *J. Am. Chem. Soc*. **2011**, 133, 18911–18923.

118. Wierzejewska, M.; Mielke, Z. *Chem. Phys. Letters* **2001**, 349, 227–234.

119. Toumi, A.; Pietri, N.; Couturier-Tamburelli, I. *Phys. Chem. Chem. Phys.* **2015**, 17, 30352–30363.

120. Toumi, A.; Couturier-Tamburelli, I.; Chiavassa, T.; Pietri, N. *J. Phys. Chem. A* **2014**, 118, 2453−2462.

121. Hudson R. L.; Moore, M. H. *Icarus* **2004**, 172, 466−478.

122. Nagy, P. *Antioxid. Redox Signal.* **2013,** 18, 1623-1641.

123. Winterbourn, C. C.; Hampton, M. B. *Free Radic. Biol. Med*. **2008**, 45, 549-561.

124. Okuda, S.; Sherman, D. J.; Silhavy, T. J.; Ruiz, N.; Kahne, D. *Nat. Rev. Microbiol.* **2016**, 14, 337–345.

125. Carter, R.; Coulson, A.; Bhatti, S.; Taylor, B. J.; Elliott, J. F. *Mol*. *Biochem. Parasitol.* **1995**, 71, 203-210.

126. Bazargani, M. F.; Talavat, L.; Soheila, N.; Khavasi, H. R. *Acta Cryst. E* **2011**, E67, o2585.

127. Steed, K. M.; Steed, J. W. *Chem. Rev.* **2015**, 115, 2895-2933.

APPENDIX

Appendix

Table 25. Internal coordinates used in the 2-MI thione normal mode analysis.[a]

Coordinate	A. Description [b]	Definition [c]
S_1	$\nu(NH)_s$	$\nu_{8,4} + \nu_{9,5}$
S_2	$\nu(NH)_{as}$	$\nu_{8,4} - \nu_{9,5}$
S_3	$\nu(C=S)$	$\nu_{1,10}$
S_4	$\nu(CH)_s$	$\nu_{7,3} + \nu_{2,6}$
S_5	$\nu(CH)_{as}$	$\nu_{7,3} - \nu_{2,6}$
S_6	$\nu(C=C)$	$\nu_{7,2}$
S_7	$\nu(NC)_s$	$\nu_{8,1} + \nu_{9,1}$
S_8	$\nu(NC)_{as}$	$\nu_{8,1} - \nu_{9,1}$
S_9	$\nu(CN)_s$	$\nu_{8,7} + \nu_{9,2}$
S_{10}	$\nu(CN)_{as}$	$\nu_{8,7} - \nu_{9,2}$
S_{11}	$\delta(NH)_s$	$\delta_{5,1,9} - \delta_{5,2,9} + \delta_{4,1,8} - \delta_{4,7,8}$
S_{12}	$\delta(NH)_{as}$	$\delta_{5,1,9} - \delta_{2,5,9} - \delta_{4,1,8} + \delta_{4,7,8}$
S_{13}	$\delta(C=S)$	$\delta_{10,8,1} - \delta_{10,9,1}$
S_{14}	$\delta(CH)_s$	$\delta_{6,9,2} - \delta_{6,7,2} + \delta_{3,8,7} - \delta_{3,2,7}$
S_{15}	$\delta(CH)_{as}$	$\delta_{6,9,2} - \delta_{6,7,2} - \delta_{3,8,7} + \delta_{3,2,7}$
S_{16}	$\delta(ring)_1$	$\delta_{9,8,1} - 0.809\delta_{7,1,8} - 0.809\delta_{2,1,9} + 0.309\delta_{2,8,7} + 0.309\delta_{7,9,2}$
S_{17}	$\delta(ring)_2$	$-1.118\delta_{7,1,8} + 1.118\delta_{2,1,9} + 1.809\delta_{2,8,7} - 1.809\delta_{7,9,2}$
S_{18}	$\tau(ring)_1$	$\tau_{8,7,2,9} - 0.809\tau_{2,7,8,1} - 0.809\tau_{7,2,9,1} + 0.309\tau_{7,8,1,9} + 0.309\tau_{2,9,1,8}$
S_{19}	$\tau(ring)_2$	$1.118\tau_{2,7,8,1} - 1.118\tau_{7,2,9,1} - 1.809\tau_{7,8,1,9} + 1.809\tau_{2,9,1,8}$
S_{20}	$\gamma(NH)_s$	$\gamma_{5,9,2,1} + \gamma_{4,8,7,1}$
S_{21}	$\gamma(NH)_{as}$	$\gamma_{5,9,2,1} - \gamma_{4,8,7,1}$
S_{22}	$\gamma(C=S)$	$\gamma_{10,9,1,8}$
S_{23}	$\gamma(CH)_s$	$\gamma_{6,9,2,7} + \gamma_{3,8,7,2}$
S_{24}	$\gamma(CH)_{as}$	$\gamma_{6,9,2,7} - \gamma_{3,8,7,2}$

[a] The atom numbering is presented in figure 8. [b] Approximate description: ν - stretching; δ - in-plane-bending; γ - out-of-plane bending; τ - torsion. [c] ν_i is the distance between atoms A_j and A_j; $\delta_{i,k,j}$ and is the angle between vectors A_iA_j and A_jA_k; $\tau_{l,j,k,l}$ is the dihedral angle between the plane defined by A_i, A_j, A_k and the plane defined by A_j, A_k, A_l atoms; $\gamma_{i,j,k,l}$ the angle between the vector A_iA_k and the plane defined by atoms A_j,A_k,A_l . The normalizations constants are not showed.

Table 26. Internal coordinates used in the 2-MBI thione normal mode analysis.[a]

Coordinate	A. Description [b]	Definition [c]
S_1	$\nu(NH)_s$	$\nu_{11,16} + \nu_{12,14}$
S_2	$\nu(NH)_{as}$	$\nu_{11,16} - \nu_{12,14}$
S_3	$\nu(C=S)$	$\nu_{13,15}$
S_4	$\nu(NC)_s$	$\nu_{11,13} + \nu_{12,13}$
S_5	$\nu(NC)_{as}$	$\nu_{11,13} - \nu_{12,13}$
S_6	$\nu(CN)_s$	$\nu_{11,3} + \nu_{12,2}$
S_7	$\nu(CN)_{as}$	$\nu_{11,3} + \nu_{12,2}$
S_8	$\nu(CH)_1$	$\nu_{1,7} + \nu_{4,8} + \nu_{6,10} + \nu_{5,9}$
S_9	$\nu(CH)_2$	$\nu_{1,7} + \nu_{4,8} - \nu_{6,10} - \nu_{5,9}$
S_{10}	$\nu(CH)_3$	$\nu_{1,7} - \nu_{4,8} + \nu_{6,10} - \nu_{5,9}$
S_{11}	$\nu(CH)_4$	$\nu_{1,7} - \nu_{4,8} - \nu_{6,10} + \nu_{5,9}$
S_{12}	$\nu(CC)_1$	$\nu_{2,1} + \nu_{3,4} + \nu_{1,6} + \nu_{5,4}$
S_{13}	$\nu(CC)_2$	$\nu_{2,1} + \nu_{3,4} - \nu_{1,6} - \nu_{5,4}$
S_{14}	$\nu(CC)_3$	$\nu_{2,1} - \nu_{3,4} + \nu_{1,6} - \nu_{5,4}$
S_{15}	$\nu(CC)_4$	$\nu_{2,1} - \nu_{3,4} - \nu_{1,6} + \nu_{5,4}$
S_{16}	$\nu(CC)_5$	$\nu_{2,3}$
S_{17}	$\nu(CC)_6$	$\nu_{6,5}$
S_{18}	$\delta(NH)_s$	$\delta_{14,13,12} - \delta_{14,2,12} + \delta_{16,13,11} - \delta_{16,3,11}$
S_{19}	$\delta(NH)_{as}$	$\delta_{14,13,12} - \delta_{14,2,12} - \delta_{16,13,11} + \delta_{16,3,11}$
S_{20}	$\delta(C=S)$	$\delta_{15,11,13} - \delta_{15,12,13}$
S_{21}	$\delta(ring1)_1$	$\delta_{12,11,13} - 0.809\delta_{3,13,11} - 0.809\delta_{2,13,12} + 0.309\delta_{2,11,3} + 0.309\delta_{3,12,2}$
S_{22}	$\delta(ring1)_2$	$-1.118\delta_{3,13,11} + 1.118\delta_{2,13,12} + 1.809\delta_{2,11,3} - 1.809\delta_{3,12,2}$
S_{23}	$\delta(CH)_1$	$\delta_{9,4,5} + \delta_{10,1,6} + \delta_{8,3,4} + \delta_{7,2,1}$
S_{24}	$\delta(CH)_2$	$\delta_{9,4,5} - \delta_{10,1,6} + \delta_{8,3,4} - \delta_{7,2,1}$
S_{25}	$\delta(CH)_3$	$\delta_{9,4,5} - \delta_{10,1,6} - \delta_{8,3,4} + \delta_{7,2,1}$
S_{26}	$\delta(CH)_4$	$\delta_{9,4,5} + \delta_{10,1,6} - \delta_{8,3,4} - \delta_{7,2,1}$
S_{27}	$\delta(ring2)_1$	$\delta_{4,2,3} - \delta_{1,3,2} + \delta_{5,3,4} - \delta_{6,2,1} + \delta_{6,4,5} - \delta_{5,1,6}$
S_{28}	$\delta(ring2)_2$	$2\delta_{6,4,5} - \delta_{5,3,4} - \delta_{4,2,3} + 2\delta_{1,3,2} - \delta_{6,2,1} - \delta_{5,1,6}$
S_{29}	$\delta(ring2)_3$	$\delta_{5,3,4} + \delta_{4,2,3} - \delta_{6,2,1} - \delta_{5,1,6}$
S_{30}	$\tau(ring1)_1$	$\tau_{11,3,2,12} - 0.809\tau_{2,3,11,13} - 0.809\tau_{3,2,12,13} + 0.309\tau_{3,11,13,12} + 0.309\tau_{2,12,13,11}$
S_{31}	$\tau(ring1)_2$	$1.118\tau_{2,3,11,13} - 1.118\tau_{3,2,12,13} - 1.809\tau_{3,11,13,12} + 1.809\tau_{2,12,13,11}$
S_{32}	$\tau(ring2)_1$	$-\tau_{4,5,6,1} + \tau_{4,3,2,1} - \tau_{5,4,3,2} + \tau_{5,6,1,2} - \tau_{6,1,2,3} + \tau_{6,5,4,3}$
S_{33}	$\tau(ring2)_2$	$2\tau_{4,5,6,1} - \tau_{6,5,4,3} - \tau_{5,6,1,2} + 2\tau_{4,3,2,1} - \tau_{5,4,3,2} - \tau_{6,1,2,3}$
S_{34}	$\tau(ring2)_3$	$\tau_{6,5,4,3} - \tau_{5,6,1,2} + \tau_{6,1,2,3} - \tau_{6,5,4,3}$
S_{35}	τ Butterfly	$\tau_{11,3,2,1} - \tau_{12,2,3,4}$
S_{36}	$\gamma(NH)_s$	$\gamma_{14,2,12,13} + \gamma_{16,3,11,13}$
S_{37}	$\gamma(NH)_{as}$	$\gamma_{14,2,12,13} - \gamma_{16,3,11,13}$
S_{38}	$\gamma(C=S)$	$\gamma_{15,11,13,12}$
S_{39}	$\gamma(CH)_1$	$\gamma_{7,6,1,2} + \gamma_{8,5,4,3} + \gamma_{10,5,6,1} + \gamma_{9,6,5,4}$
S_{40}	$\gamma(CH)_2$	$\gamma_{7,6,1,2} - \gamma_{8,5,4,3} + \gamma_{10,5,6,1} - \gamma_{9,6,5,4}$
S_{41}	$\gamma(CH)_3$	$\gamma_{7,6,1,2} - \gamma_{8,5,4,3} - \gamma_{10,5,6,1} + \gamma_{9,6,5,4}$
S_{42}	$\gamma(CH)_4$	$\gamma_{7,6,1,2} + \gamma_{8,5,4,3} - \gamma_{10,5,6,1} - \gamma_{9,6,5,4}$

[a] The atom numbering is presented in figure 11. [b] Approximate description: ν - stretching; δ - in-plane-bending; γ - out-of-plane bending; τ - torsion. [c] ν_i is the distance between atoms A_j and A_j; $\delta_{i,k,j}$ and is the angle between vectors A_iA_j and A_jA_k; $\tau_{I,j,k,l}$ is the dihedral angle between the plane defined by A_i, A_j, A_k and the plane defined by A_j, A_k, A_l atoms; $\gamma_{i,j,k,l}$ the angle between the vector A_iA_k and the plane defined by atoms A_j,A_k,A_l . The normalizations constants are not showed.

Table 27. Internal coordinates used in the 1-M-2-MI thione normal mode analysis.[a]

Coordinate	A. Description [b]	Definition [c]
S_1	$\nu(NH)$	$\nu_{8,4}$
S_2	$\nu(NC)_1$	$\nu_{7,10}$
S_3	$\nu(CH_3)_s$	$\nu_{10,13} + \nu_{10,12} + \nu_{10,11}$
S_4	$\nu(CH_3)_{as'}$	$2\nu_{10,13} - \nu_{10,12} - \nu_{10,11}$
S_5	$\nu(CH_3)_{as''}$	$\nu_{10,12} - \nu_{10,11}$
S_6	$\nu(C=S)$	$\nu_{1,9}$
S_7	$\nu(CH)_1$	$\nu_{6,3}$
S_8	$\nu(CH)_2$	$\nu_{2,5}$
S_9	$\nu(C=C)$	$\nu_{2,6}$
S_{10}	$\nu(NC)_2$	$\nu_{8,1}$
S_{11}	$\nu(NC)_3$	$\nu_{7,1}$
S_{12}	$\nu(CN)_1$	$\nu_{7,6}$
S_{13}	$\nu(CN)_2$	$\nu_{8,2}$
S_{14}	$\delta(NH)$	$\delta_{4,1,8} - \delta_{4,2,8}$
S_{15}	$\delta(NC)$	$\delta_{10,1,7} - \delta_{10,6,7}$
S_{16}	$\delta(CH_3)_s$	$\delta_{13,12,10} + \delta_{13,11,10} + \delta_{12,11,10} - \delta_{7,13,10} - \delta_{7,11,10} - \delta_{7,12,10}$
S_{17}	$\gamma(CH_3)_{as'}$	$2\delta_{12,11,10} - \delta_{13,12,10} - \delta_{13,11,10}$
S_{18}	$\delta(CH_3)_{as'}$	$2\delta_{7,13,10} - \delta_{7,12,10} - \delta_{7,11,10}$
S_{19}	$\gamma(CH_3)_{as''}$	$\delta_{13,12,10} - \delta_{13,11,10}$
S_{20}	$\delta(CH_3)_{as''}$	$\delta_{7,12,10} - \delta_{7,11,10}$
S_{21}	$\delta(C=S)$	$\delta_{9,8,1} - \delta_{9,7,1}$
S_{22}	$\delta(CH)_1$	$\delta_{5,8,2} - \delta_{5,6,2}$
S_{23}	$\delta(CH)_2$	$\delta_{3,7,6} - \delta_{3,2,6}$
S_{24}	$\delta(ring)_1$	$\delta_{7,8,1} - 0.809\delta_{2,1,8} - 0.809\delta_{6,1,7} + 0.309\delta_{6,8,2} + 0.309\delta_{2,7,6}$
S_{25}	$\delta(ring)_2$	$-1.118\delta_{2,1,8} + 1.118\delta_{6,1,7} + 1.809\delta_{6,8,2} - 1.809\delta_{2,7,6}$
S_{26}	$\tau(CH_3)$	$\tau_{13,10,7,1} + \tau_{13,10,7,6} + \tau_{12,10,7,1} + \tau_{12,10,7,6} + \tau_{11,10,7,1} + \tau_{11,10,7,6}$
S_{27}	$\tau(ring)_1$	$\tau_{8,2,6,7} - 0.809\tau_{6,2,8,1} - 0.809\tau_{2,6,7,1} + 0.309\tau_{2,8,1,7} + 0.309\tau_{6,7,1,8}$
S_{28}	$\tau(ring)_2$	$1.118\tau_{6,2,8,1} - 1.118\tau_{2,6,7,1} - 1.809\tau_{2,8,1,7} + 1.809\tau_{6,7,1,8}$
S_{29}	$\gamma(NH)$	$\gamma_{4,2,8,1}$
S_{30}	$\gamma(NC)$	$\gamma_{10,6,1,7}$
S_{31}	$\gamma(C=S)$	$\gamma_{9,7,7,8}$
S_{32}	$\gamma(CH)_1$	$\gamma_{3,2,6,7}$
S_{33}	$\gamma(CH)_2$	$\gamma_{5,8,2,6}$

[a] The atom numbering is presented in figure 14. [b] Approximate description: ν - stretching; δ - in-plane-bending; γ - out-of-plane bending; τ - torsion. [c] ν_i is the distance between atoms A_j and A_j; $\delta_{i,k,j}$ and is the angle between vectors A_iA_j and A_jA_k; $\tau_{l,j,k,l}$ is the dihedral angle between the plane defined by A_i, A_j, A_k and the plane defined by A_j, A_k, A_l atoms; $\gamma_{i,j,k,l}$ the angle between the vector A_iA_k and the plane defined by atoms A_j,A_k,A_l . The normalizations constants are not showed.

Table 28. Internal coordinates used in the 1-M-2-MBI thione normal mode analysis.[a]

Coordinate	A. Description [b]	Definition [c]
S_1	ν(NH)	$\nu_{11,15}$
S_2	$\nu(NC)_1$	$\nu_{12,16}$
S_3	$\nu(CH_3)_s$	$\nu_{16,19} + \nu_{16,17} + \nu_{16\text{-},18}$
S_4	$\nu(CH_3)_{as'}$	$2\nu_{16,19} - \nu_{16,17} - \nu_{16,18}$
S_5	$\nu(CH_3)_{as''}$	$\nu_{16,17} - \nu_{16,18}$
S_6	ν(C=S)	$\nu_{13,14}$
S_7	$\nu(NC)_2$	$\nu_{12,13}$
S_8	$\nu(NC)_3$	$\nu_{11,13}$
S_9	$\nu(CN)_1$	$\nu_{12,2}$
S_{10}	$\nu(CN)_2$	$\nu_{11,3}$
S_{11}	$\nu(CH)_1$	$\nu_{1,7} + \nu_{4,8} + \nu_{6,10} + \nu_{5,9}$
S_{12}	$\nu(CH)_2$	$\nu_{1,7} + \nu_{4,8} - \nu_{6,10} - \nu_{5,9}$
S_{13}	$\nu(CH)_3$	$\nu_{1,7} - \nu_{4,8} + \nu_{6,10} - \nu_{5,9}$
S_{14}	$\nu(CH)_4$	$\nu_{1,7} - \nu_{4,8} - \nu_{6,10} + \nu_{5,9}$
S_{15}	$\nu(CC)_1$	$\nu_{2,1}$
S_{16}	$\nu(CC)_2$	$\nu_{3,4}$
S_{17}	$\nu(CC)_3$	$\nu_{1,6}$
S_{18}	$\nu(CC)_4$	$\nu_{5,4}$
S_{19}	$\nu(CC)_5$	$\nu_{2,3}$
S_{20}	$\nu(CC)_6$	$\nu_{6,5}$
S_{21}	δ(NH)	$\delta_{15,13,11} - \delta_{15,3,11}$
S_{22}	δ(NC)	$\delta_{16,13,12} - \delta_{16,2,12}$
S_{23}	$\delta(CH_3)_s$	$\delta_{19,17,16} + \delta_{19,18,16} + \delta_{17,18,16} - \delta_{12,19,16} - \delta_{12,18,16} - \delta_{12,17,16}$
S_{24}	$\gamma(CH_3)_{as'}$	$2\delta_{17,18,16} - \delta_{19,17,16} - \delta_{19,18,16}$
S_{25}	$\delta(CH_3)_{as'}$	$2\delta_{12,19,16} - \delta_{12,17,16} - \delta_{12,18,16}$
S_{26}	$\gamma(CH_3)_{as''}$	$\delta_{19,17,16} - \delta_{19,18,16}$
S_{27}	$\delta(CH_3)_{as''}$	$\delta_{12,17,16} - \delta_{12,18,16}$
S_{28}	δ(C=S)	$\delta_{14,12,13} - \delta_{14,11,13}$
S_{29}	$\delta(ring1)_1$	$\delta_{12,11,13} - 0.809\delta_{3,13,11} - 0.809\delta_{2,13,12} + 0.309\delta_{2,11,3} + 0.309\delta_{3,12,2}$
S_{30}	$\delta(ring1)_2$	$-1.118\delta_{3,13,11} + 1.118\delta_{2,13,12} + 1.809\delta_{2,11,3} - 1.809\delta_{3,12,2}$
S_{31}	$\delta(CH)_1$	$\delta_{9,4,5} - \delta_{9,6,5}$
S_{32}	$\delta(CH)_2$	$\delta_{10,1,6} - \delta_{10,5,6}$
S_{33}	$\delta(CH)_3$	$\delta_{8,3,4} - \delta_{8,5,4}$
S_{34}	$\delta(CH)_4$	$\delta_{7,2,1} - \delta_{7,6,1}$
S_{35}	$\delta(ring2)_1$	$\delta_{4,2,3} - \delta_{1,3,2} + \delta_{5,3,4} - \delta_{6,2,1} + \delta_{6,4,5} - \delta_{5,1,6}$
S_{36}	$\delta(ring2)_2$	$2\delta_{6,4,5} - \delta_{5,3,4} - \delta_{4,2,3} + 2\delta_{1,3,2} - \delta_{6,2,1} - \delta_{5,1,6}$
S_{37}	$\delta(ring2)_3$	$\delta_{5,3,4} - \delta_{4,2,3} + \delta_{6,2,1} - \delta_{5,1,6}$
S_{38}	$\tau(CH_3)$	$\tau_{19,16,12,2} + \tau_{19,16,12,13} + \tau_{17,16,12,2} + \tau_{17,16,12,13} + \tau_{18,16,12,2} + \tau_{18,16,12,13}$
S_{39}	$\tau(ring1)_1$	$\tau_{11,3,2,12} - 0.809\tau_{2,3,11,13} - 0.809\tau_{3,2,12,13} + 0.309\tau_{3,11,13,12} + 0.309\tau_{2,12,13,11}$
S_{40}	$\tau(ring1)_2$	$1.118\tau_{2,3,11,13} - 1.118\tau_{3,2,12,13} - 1.809\tau_{3,11,13,12} + 1.809\tau_{2,12,13,11}$
S_{41}	$\tau(ring2)_1$	$-\tau_{4,5,6,1} + \tau_{4,3,2,1} - \tau_{5,4,3,2} + \tau_{5,6,1,2} - \tau_{6,1,2,3} + \tau_{6,5,4,3}$
S_{42}	$\tau(ring2)_2$	$2\tau_{4,5,6,1} - \tau_{6,5,4,3} - \tau_{5,6,1,2} + 2\tau_{4,3,2,1} - \tau_{5,4,3,2} - \tau_{6,1,2,3}$
S_{43}	$\tau(ring2)_3$	$\tau_{6,5,4,3} - \tau_{5,6,1,2} + \tau_{6,1,2,3} - \tau_{6,5,4,3}$
S_{44}	τ Butterfly	$\tau_{11,3,2,1} - \tau_{12,2,3,4}$
S_{45}	γ(NH)	$\gamma_{15,3,11,13}$
S_{46}	γ(NC)	$\gamma_{16,2,12,13}$
S_{47}	γ(C=S)	$\gamma_{15,11,13,12}$
S_{48}	$\gamma(CH)_1$	$\gamma_{7,6,1,2} + \gamma_{8,5,4,3} + \gamma_{10,5,6,1} + \gamma_{9,6,5,4}$
S_{49}	$\gamma(CH)_2$	$\gamma_{7,6,1,2} - \gamma_{8,5,4,3} + \gamma_{10,5,6,1} - \gamma_{9,6,5,4}$
S_{50}	$\gamma(CH)_3$	$\gamma_{7,6,1,2} - \gamma_{8,5,4,3} - \gamma_{10,5,6,1} + \gamma_{9,6,5,4}$
S_{51}	$\gamma(CH)_4$	$\gamma_{7,6,1,2} + \gamma_{8,5,4,3} - \gamma_{10,5,6,1} - \gamma_{9,6,5,4}$

[a] The atom numbering is presented in figure 17. [b] Approximate description: ν - stretching; δ - in-plane-bending; γ - out-of-plane bending; τ - torsion. [c] ν_i is the distance between atoms A_j and A_j; $\delta_{i,k,j}$ and is the angle between vectors A_iA_j and A_jA_k; $\tau_{l,j,k,l}$ is the dihedral angle between the plane defined by A_i, A_j, A_k and the plane defined by A_j, A_k, A_l atoms; $\gamma_{i,j,k,l}$ the angle between the vector A_iA_k and the plane defined by atoms A_j,A_k,A_l . The normalizations constants are not showed.

Table 29. Internal coordinates used in the 2-MI thiol normal mode analysis. [a]

Coordinate	A. Description [b]	Definition [c]
S_1	ν(NH)	$\nu_{3,7}$
S_2	ν(CS)	$\nu_{2,1}$
S_3	ν(SH)	$\nu_{1,8}$
S_4	$\nu(CH)_1$	$\nu_{4,10}$
S_5	$\nu(CH)_2$	$\nu_{5,9}$
S_6	ν(C=C)	$\nu_{4,5}$
S_7	$\nu(CN)_1$	$\nu_{4,3}$
S_8	$\nu(CN)_2$	$\nu_{5,6}$
S_9	$\nu(NC)_1$	$\nu_{3,2}$
S_{10}	$\nu(NC)_2$	$\nu_{6,2}$
S_{11}	δ(NH)	$\delta_{7,2,3} - \delta_{7,4,3}$
S_{12}	δ(CS)	$\delta_{1,6,2} - \delta_{1,3,2}$
S_{13}	δ(SH)	$\delta_{8,2,1}$
S_{14}	$\delta(CH)_1$	$\delta_{10,3,4} - \delta_{10,5,4}$
S_{15}	$\delta(CH)_2$	$\delta_{9,6,5} - \delta_{9,4,5}$
S_{16}	$\delta(ring)_1$	$\delta_{3,6,2} - 0.809\delta_{5,2,6} - 0.809\delta_{4,2,3} + 0.309\delta_{4,6,5} + 0.309\delta_{5,3,4}$
S_{17}	$\delta(ring)_2$	$-1.118\delta_{5,2,6} + 1.118\delta_{4,2,3} + 1.809\delta_{4,6,5} - 1.809\delta_{5,3,4}$
S_{18}	$\tau(ring)_1$	$\tau_{6,5,4,3} - 0.809\tau_{4,5,6,2} - 0.809\tau_{5,4,3,2} + 0.309\tau_{5,6,2,3} + 0.309\tau_{4,3,2,6}$
S_{19}	$\tau(ring)_2$	$1.118\tau_{4,5,6,2} - 1.118\tau_{5,4,3,2} - 1.809\tau_{5,6,2,3} + 1.809\tau_{4,3,2,6}$
S_{20}	τ(SH)	$\tau_{8,1,2,6} + \tau_{8,1,2,3}$
S_{21}	γ(NH)	$\gamma_{7,4,3,2}$
S_{22}	γ(CS)	$\gamma_{1,3,2,6}$
S_{23}	$\gamma(CH)_1$	$\gamma_{10,3,4,5}$
S_{24}	$\gamma(CH)_2$	$\gamma_{9,4,5,6}$

[a] The atom numbering is presented in figure 8. [b] Approximate description: ν - stretching; δ - in-plane-bending; γ - out-of-plane bending; τ - torsion. [c] ν_i is the distance between atoms A_j and A_j; $\delta_{i,k,j}$ and is the angle between vectors A_iA_j and A_jA_k; $\tau_{l,j,k,l}$ is the dihedral angle between the plane defined by A_i, A_j, A_k and the plane defined by A_j, A_k, A_l atoms; $\gamma_{i,j,k,l}$ the angle between the vector A_iA_k and the plane defined by atoms A_j,A_k,A_l . The normalizations constants are not showed.

Table 30. Internal coordinates used in the 2-MBI thiol normal mode analysis.[a]

Coordinate	A. Description [b]	Definition [c]
S_1	ν(NH)	$\nu_{12,14}$
S_2	ν(CS)	$\nu_{13,15}$
S_3	ν(SH)	$\nu_{15,16}$
S_4	$\nu(NC)_1$	$\nu_{11,13}$
S_5	$\nu(NC)_2$	$\nu_{12,13}$
S_6	$\nu(CN)_3$	$\nu_{12,2}$
S_7	$\nu(CN)_4$	$\nu_{11,3}$
S_8	$\nu(CH)_1$	$\nu_{1,7} + \nu_{4,8} + \nu_{6,10} + \nu_{5,9}$
S_9	$\nu(CH)_2$	$\nu_{1,7} - \nu_{4,8} + \nu_{6,10} + \nu_{5,9}$
S_{10}	$\nu(CH)_3$	$\nu_{1,7} + \nu_{4,8} - \nu_{6,10} - \nu_{5,9}$
S_{11}	$\nu(CH)_4$	$-\nu_{1,7} + \nu_{4,8} - \nu_{6,10} + \nu_{5,9}$
S_{12}	$\nu(CC)_1$	$\nu_{2,1}$
S_{13}	$\nu(CC)_2$	$\nu_{3,4}$
S_{14}	$\nu(CC)_3$	$\nu_{1,6}$
S_{15}	$\nu(CC)_4$	$\nu_{5,4}$
S_{16}	$\nu(CC)_5$	$\nu_{2,3}$
S_{17}	$\nu(CC)_6$	$\nu_{6,5}$
S_{18}	δ(NH)	$\delta_{14,13,12} - \delta_{14,2,12}$
S_{19}	δ(CS)	$\delta_{15,11,13} - \delta_{15,12,13}$
S_{20}	δ(SH)	$\delta_{16,13,15}$
S_{21}	$\delta(ring1)_1$	$\delta_{12,11,13} - 0.809\delta_{3,13,11} - 0.809\delta_{2,13,12} + 0.309\delta_{2,11,3} + 0.309\delta_{3,12,2}$
S_{22}	$\delta(ring1)_2$	$-1.118\delta_{3,13,11} + 1.118\delta_{2,13,12} + 1.809\delta_{2,11,3} - 1.809\delta_{3,12,2}$
S_{23}	$\delta(CH)_1$	$\delta_{9,4,5} - \delta_{9,6,5}$
S_{24}	$\delta(CH)_2$	$\delta_{10,1,6} - \delta_{10,5,6}$
S_{25}	$\delta(CH)_3$	$\delta_{8,3,4} - \delta_{8,5,4}$
S_{26}	$\delta(CH)_4$	$\delta_{7,2,1} - \delta_{7,6,1}$
S_{27}	$\delta(ring2)_1$	$\delta_{4,2,3} - \delta_{1,3,2} + \delta_{5,3,4} - \delta_{6,2,1} + \delta_{6,4,5} - \delta_{5,1,6}$
S_{28}	$\delta(ring2)_2$	$2\delta_{6,4,5} - \delta_{5,3,4} - \delta_{4,2,3} + 2\delta_{1,3,2} - \delta_{6,2,1} - \delta_{5,1,6}$
S_{29}	$\delta(ring2)_3$	$\delta_{5,3,4} + \delta_{4,2,3} - \delta_{6,2,1} - \delta_{5,1,6}$
S_{30}	$\tau(ring1)_1$	$\tau_{11,3,2,12} - 0.809\tau_{2,3,11,13} - 0.809\tau_{3,2,12,13} + 0.309\tau_{3,11,13,12} + 0.309\tau_{2,12,13,11}$
S_{31}	$\tau(ring1)_2$	$1.118\tau_{2,3,11,13} - 1.118\tau_{3,2,12,13} - 1.809\tau_{3,11,13,12} + 1.809\tau_{2,12,13,11}$
S_{32}	$\tau(ring2)_1$	$-\tau_{4,5,6,1} + \tau_{4,3,2,1} - \tau_{5,4,3,2} + \tau_{5,6,1,2} - \tau_{6,1,2,3} + \tau_{6,5,4,3}$
S_{33}	$\tau(ring2)_2$	$2\tau_{4,5,6,1} - \tau_{6,5,4,3} - \tau_{5,6,1,2} + 2\tau_{4,3,2,1} - \tau_{5,4,3,2} - \tau_{6,1,2,3}$
S_{34}	$\tau(ring2)_3$	$\tau_{6,5,4,3} - \tau_{5,6,1,2} + \tau_{6,1,2,3} - \tau_{6,5,4,3}$
S_{35}	τ Butterfly	$\tau_{11,3,2,1} - \tau_{12,2,3,4}$
S_{36}	τ(SH)	$\tau_{16,15,13,11} + \tau_{16,15,13,12}$
S_{37}	γ(NH)	$\gamma_{14,2,12,13}$
S_{38}	γ(CS)	$\gamma_{15,11,13,12}$
S_{39}	$\gamma(CH)_1$	$\gamma_{7,6,1,2} + \gamma_{8,5,4,3} + \gamma_{10,5,6,1} + \gamma_{9,6,5,4}$
S_{40}	$\gamma(CH)_2$	$\gamma_{7,6,1,2} - \gamma_{8,5,4,3} + \gamma_{10,5,6,1} - \gamma_{9,6,5,4}$
S_{41}	$\gamma(CH)_3$	$\gamma_{7,6,1,2} - \gamma_{8,5,4,3} - \gamma_{10,5,6,1} + \gamma_{9,6,5,4}$
S_{42}	$\gamma(CH)_4$	$\gamma_{7,6,1,2} + \gamma_{8,5,4,3} - \gamma_{10,5,6,1} - \gamma_{9,6,5,4}$

[a] The atom numbering is presented in figure 11. [b] Approximate description: ν - stretching; δ - in-plane-bending; γ - out-of-plane bending; τ - torsion. [c] ν_i is the distance between atoms A_j and A_j; $\delta_{i,k,j}$ and is the angle between vectors A_iA_j and A_jA_k; $\tau_{i,j,k,l}$ is the dihedral angle between the plane defined by A_i, A_j, A_k and the plane defined by A_j, A_k, A_l atoms; $\gamma_{i,j,k,l}$ the angle between the vector A_iA_k and the plane defined by atoms A_j,A_k,A_l . The normalizations constants are not showed.

Table 31. Internal coordinates used in the 1-M-2-MI thiol normal mode analysis.[a]

Coordinate	A. Description [b]	Definition [c]
S_1	$\nu(NC)_1$	$\nu_{3,10}$
S_2	$\nu(CH_3)_s$	$\nu_{10,11} + \nu_{10,13} + \nu_{10,12}$
S_3	$\nu(CH_3)_{as'}$	$2\nu_{10,11} - \nu_{10,13} - \nu_{10,12}$
S_4	$\nu(CH_3)_{as''}$	$\nu_{10,11} - \nu_{10,12}$
S_5	$\nu(CS)$	$\nu_{2,1}$
S_6	$\nu(SH)$	$\nu_{1,7}$
S_7	$\nu(CH)_1$	$\nu_{4,9}$
S_8	$\nu(CH)_2$	$\nu_{5,8}$
S_9	$\nu(C=C)$	$\nu_{4,5}$
S_{10}	$\nu(NC)_2$	$\nu_{3,2}$
S_{11}	$\nu(NC)_3$	$\nu_{6,2}$
S_{12}	$\nu(CN)_1$	$\nu_{3,4}$
S_{13}	$\nu(CN)_2$	$\nu_{6,5}$
S_{14}	$\delta(NC)$	$\delta_{10,2,3} - \delta_{10,4,3}$
S_{15}	$\delta(CH_3)_s$	$\delta_{11,13,10} + \delta_{11,12,10} + \delta_{13,12,10} - \delta_{3,11,10} - \delta_{3,12,10} - \delta_{3,13,10}$
S_{16}	$\gamma(CH_3)_{as'}$	$2\delta_{13,12,10} - \delta_{11,13,10} - \delta_{11,12,10}$
S_{17}	$\delta(CH_3)_{as'}$	$2\delta_{3,11,10} - \delta_{3,13,10} - \delta_{3,12,10}$
S_{18}	$\gamma(CH_3)_{as''}$	$\delta_{11,13,10} - \delta_{11,12,10}$
S_{19}	$\delta(CH_3)_{as''}$	$\delta_{3,13,10} - \delta_{3,12,10}$
S_{20}	$\delta(CS)$	$\delta_{1,6,2} - \delta_{1,3,2}$
S_{21}	$\delta(SH)$	$\delta_{7,2,1}$
S_{22}	$\delta(CH)_1$	$\delta_{8,6,5} - \delta_{8,4,5}$
S_{23}	$\delta(CH)_2$	$\delta_{9,3,4} - \delta_{9,5,4}$
S_{24}	$\delta(ring)_1$	$\delta_{3,6,2} - 0.809\delta_{5,2,6} - 0.809\delta_{4,2,3} + 0.309\delta_{4,6,5} + 0.309\delta_{5,3,4}$
S_{25}	$\delta(ring)_2$	$-1.118\delta_{5,2,6} + 1.118\delta_{4,2,3} + 1.809\delta_{4,6,5} - 1.809\delta_{5,3,4}$
S_{26}	$\tau(CH_3)$	$\tau_{11,10,3,2} + \tau_{11,10,3,4} + \tau_{13,10,3,2} + \tau_{13,10,3,4} + \tau_{12,10,3,2} + \tau_{12,10,3,4}$
S_{27}	$\tau(ring)_1$	$\tau_{6,5,4,3} - 0.809\tau_{4,5,6,2} - 0.809\tau_{5,4,3,2} + 0.309\tau_{5,6,2,3} + 0.309\tau_{4,3,2,6}$
S_{28}	$\tau(ring)_2$	$1.118\tau_{4,5,6,2} - 1.118\tau_{5,4,3,2} - 1.809\tau_{5,6,2,3} + 1.809\tau_{4,3,2,6}$
S_{29}	$\tau(SH)$	$\tau_{7,1,2,3} + \tau_{7,1,2,6}$
S_{30}	$\gamma(NC)$	$\gamma_{10,4,3,2}$
S_{31}	$\gamma(CS)$	$\gamma_{1,3,2,6}$
S_{32}	$\gamma(CH)_1$	$\gamma_{9,5,4,3}$
S_{33}	$\gamma(CH)_2$	$\gamma_{8,4,5,6}$

[a] The atom numbering is presented in figure 14. [b] Approximate description: ν - stretching; δ - in-plane-bending; γ - out-of-plane bending; τ - torsion. [c] ν_i is the distance between atoms A_j and A_j; $\delta_{i,k,j}$ and is the angle between vectors A_iA_j and A_jA_k; $\tau_{l,j,k,l}$ is the dihedral angle between the plane defined by A_i, A_j, A_k and the plane defined by A_j, A_k, A_l atoms; $\gamma_{i,j,k,l}$ the angle between the vector A_iA_k and the plane defined by atoms A_j,A_k,A_l . The normalizations constants are not showed.

Table 32. Internal coordinates used in the 1-M-2-MBI thiol normal mode analysis.[a]

Coordinate	A. Description [b]	Definition [c]
S_1	$\nu(NC)_1$	$\nu_{12,16}$
S_2	$\nu(CH_3)_s$	$\nu_{16,18} + \nu_{16,19} + \nu_{16,17}$
S_3	$\nu(CH_3)_{as'}$	$2\nu_{16,18} - \nu_{16,19} - \nu_{16,17}$
S_4	$\nu(CH_3)_{as''}$	$\nu_{16,19} - \nu_{16,17}$
S_5	$\nu(CS)$	$\nu_{13,14}$
S_6	$\nu(SH)$	$\nu_{14,15}$
S_7	$\nu(NC)_2$	$\nu_{12,13}$
S_8	$\nu(NC)_3$	$\nu_{11,13}$
S_9	$\nu(CN)_1$	$\nu_{12,2}$
S_{10}	$\nu(CN)_2$	$\nu_{11,3}$
S_{11}	$\nu(CH)_1$	$\nu_{1,7} + \nu_{4,8} + \nu_{6,10} + \nu_{5,9}$
S_{12}	$\nu(CH)_2$	$\nu_{1,7} - \nu_{4,8} - \nu_{6,10} + \nu_{5,9}$
S_{13}	$\nu(CH)_3$	$\nu_{1,7} + \nu_{4,8} - \nu_{6,10} - \nu_{5,9}$
S_{14}	$\nu(CH)_4$	$-\nu_{1,7} + \nu_{4,8} - \nu_{6,10} + \nu_{5,9}$
S_{15}	$\nu(CC)_1$	$\nu_{2,1}$
S_{16}	$\nu(CC)_2$	$\nu_{3,4}$
S_{17}	$\nu(CC)_3$	$\nu_{1,6}$
S_{18}	$\nu(CC)_4$	$\nu_{5,4}$
S_{19}	$\nu(CC)_5$	$\nu_{2,3}$
S_{20}	$\nu(CC)_6$	$\nu_{6,5}$
S_{21}	$\delta(NC)$	$\delta_{16,13,12} - \delta_{16,2,12}$
S_{22}	$\delta(CH_3)_s$	$\delta_{18,19,16} + \delta_{18,17,16} + \delta_{19,17,16} - \delta_{12,18,16} - \delta_{12,17,16} - \delta_{12,19,16}$
S_{23}	$\gamma(CH_3)_{as'}$	$2\delta_{19,17,16} - \delta_{18,19,16} - \delta_{18,17,16}$
S_{24}	$\delta(CH_3)_{as'}$	$2\delta_{12,18,16} - \delta_{12,19,16} - \delta_{12,17,16}$
S_{25}	$\gamma(CH_3)_{as''}$	$\delta_{18,19,16} - \delta_{18,17,16}$
S_{26}	$\delta(CH_3)_{as''}$	$\delta_{12,19,16} - \delta_{12,17,16}$
S_{27}	$\delta(CS)$	$\delta_{14,12,13} - \delta_{14,11,13}$
S_{28}	$\delta(SH)$	$\delta_{15,13,14}$
S_{29}	$\delta(ring1)_1$	$\delta_{12,11,13} - 0.809\delta_{3,13,11} - 0.809\delta_{2,13,12} + 0.309\delta_{2,11,3} + 0.309\delta_{3,12,2}$
S_{30}	$\delta(ring1)_2$	$-1.118\delta_{3,13,11} + 1.118\delta_{2,13,12} + 1.809\delta_{2,11,3} - 1.809\delta_{3,12,2}$
S_{31}	$\delta(CH)_1$	$\delta_{9,4,5} - \delta_{9,6,5}$
S_{32}	$\delta(CH)_2$	$\delta_{10,1,6} - \delta_{10,5,6}$
S_{33}	$\delta(CH)_3$	$\delta_{8,3,4} - \delta_{8,5,4}$
S_{34}	$\delta(CH)_4$	$\delta_{7,2,1} - \delta_{7,6,1}$
S_{35}	$\delta(ring2)_1$	$\delta_{4,2,3} - \delta_{1,3,2} + \delta_{5,3,4} - \delta_{6,2,1} + \delta_{6,4,5} - \delta_{5,1,6}$
S_{36}	$\delta(ring2)_2$	$2\delta_{6,4,5} - \delta_{5,3,4} - \delta_{4,2,3} + 2\delta_{1,3,2} - \delta_{6,2,1} - \delta_{5,1,6}$
S_{37}	$\delta(ring2)_3$	$\delta_{5,3,4} - \delta_{4,2,3} + \delta_{6,2,1} - \delta_{5,1,6}$
S_{38}	$\tau(CH_3)$	$\tau_{18,16,12,2} + \tau_{18,16,12,13} + \tau_{19,16,12,2} + \tau_{19,16,12,13} + \tau_{17,16,12,2} + \tau_{17,16,12,13}$
S_{39}	$\tau(ring1)_1$	$\tau_{11,3,2,12} - 0.809\tau_{2,3,11,13} - 0.809\tau_{3,2,12,13} + 0.309\tau_{3,11,13,12} + 0.309\tau_{2,12,13,11}$
S_{40}	$\tau(ring1)_2$	$1.118\tau_{2,3,11,13} - 1.118\tau_{3,2,12,13} - 1.809\tau_{3,11,13,12} + 1.809\tau_{2,12,13,11}$
S_{41}	$\tau(ring2)_1$	$-\tau_{4,5,6,1} + \tau_{4,3,2,1} - \tau_{5,4,3,2} + \tau_{5,6,1,2} - \tau_{6,1,2,3} + \tau_{6,5,4,3}$
S_{42}	$\tau(ring2)_2$	$2\tau_{4,5,6,1} - \tau_{6,5,4,3} - \tau_{5,6,1,2} + 2\tau_{4,3,2,1} - \tau_{5,4,3,2} - \tau_{6,1,2,3}$
S_{43}	$\tau(ring2)_3$	$\tau_{6,5,4,3} - \tau_{5,6,1,2} + \tau_{6,1,2,3} - \tau_{6,5,4,3}$
S_{44}	τ Butterfly	$\tau_{11,3,2,1} - \tau_{12,2,3,4}$
S_{45}	$\tau(SH)$	$\tau_{15,14,13,12} + \tau_{15,14,13,11}$
S_{46}	$\gamma(NC)$	$\gamma_{16,2,12,13}$
S_{47}	$\gamma(CS)$	$\gamma_{14,11,13,12}$
S_{48}	$\gamma(CH)_1$	$\gamma_{7,6,1,2} + \gamma_{8,5,4,3} + \gamma_{10,5,6,1} + \gamma_{9,6,5,4}$
S_{49}	$\gamma(CH)_2$	$\gamma_{7,6,1,2} - \gamma_{8,5,4,3} + \gamma_{10,5,6,1} - \gamma_{9,6,5,4}$
S_{50}	$\gamma(CH)_3$	$\gamma_{7,6,1,2} - \gamma_{8,5,4,3} - \gamma_{10,5,6,1} + \gamma_{9,6,5,4}$
S_{51}	$\gamma(CH)_4$	$\gamma_{7,6,1,2} + \gamma_{8,5,4,3} - \gamma_{10,5,6,1} - \gamma_{9,6,5,4}$

[a] The atom numbering is presented in figure 17. [b] Approximate description: ν - stretching; δ - in-plane-bending; γ - out-of-plane bending; τ - torsion. [c] ν_i is the distance between atoms A_j and A_j; $\delta_{i,k,j}$ and is the angle between vectors A_iA_j and A_jA_k; $\tau_{l,j,k,l}$ is the dihedral angle between the plane defined by A_i, A_j, A_k and the plane defined by A_j, A_k, A_l atoms; $\gamma_{i,j,k,l}$ the angle between the vector A_iA_k and the plane defined by atoms A_j,A_k,A_l . The normalizations constants are not showed.